Linking micro-structure to macro-behavior of granular matter: from flowing heterogeneously to morphing adaptively

Thesis by

Liuchi Li

In Partial Fulfillment of the Requirements for the
Degree of
Doctor of Philosophy

Caltech

CALIFORNIA INSTITUTE OF TECHNOLOGY
Pasadena, California

2020
Defended December 10th, 2019

Liuchi Li
ORCID: 0000-0002-1360-4757

ACKNOWLEDGEMENTS

First, I would like to express my sincere gratitude to my advisor and mentor, Prof. José Andrade, for all the lifelong lessons I have learned from him about being a academic researcher: to envision broadly, to think strategically, and to communicate efficiently. These invaluable lessons are integral to my Ph.D. journey and will continue to be so in my future academic endeavors. In particular, I am very thankful for the freedom he provided so that I can work on the specific topics that interest me, and for the guidance and encouragement he gave accompanying my ups and downs along the way. This work would not have been possible without his insightful inputs and patient responses.

Second, I would also like to extend my deep appreciation to both my candidacy committee and thesis committee members: Prof. Michael Lamb, Prof. Guruswami Ravichandran, Prof. Kaushik Bhattacharya, Prof. Chiara Daraio, and Prof. Ares Rosakis for the invaluable conversations and feedbacks on my research. In particular, I am very fortunate to have had the opportunity to work with Prof. Chiara Daraio and Prof. Ares Rosakis. Collaborating with them allowed me the integration of my research expertise in granular mechanics and physics to studies on mechanical meta-materials and earthquake physics. This work has shown me the unique beauty of working at the interface between science and engineering, and have helped shape my vision on my future research for many years to come. I would also like to thank Prof. Dennis Kochmann (now at ETH Zurich), Prof. Melany Hunt, and Prof. Nadia Lapusta who - though not on my committee - have helped my a lot in my research through classes and discussions.

Next, I would like to acknowledge both past and current officemates in B103 at Gates-Thomas for all the joy and fun both inside and outside of research. In particular thanks to Dr. Reid Kawamoto, Dr. Utkarsh Mital, Dr. Raj Kumar Pal, Prof. Xilin Lu, Dr. Xiaowen Wang, Dr. Siavash Monfared, Dr. Keng-Wit Lim, Dr. Jason Marshall, Rob Macedo, and John Harmon for giving advice and for exchanging interesting ideas. Special thanks to my awesome collaborators: Dr. Eloise Marteau, without whose experimental inputs my first project would not have been successful; and Konstantinos Karapiperis, without whose effort our computational study on sheared granular fault would otherwise end nowhere. Lastly, I would like to thank Dr. Yifan Wang from Prof. Daraio's group, for sharing his concept on meta-materials and for inviting me to be part of a really awesome and fun project.

My friends and colleagues from Caltech have given my journey a lot of fun and have helped me keeping the right amount of work-life balance. Thanks to everyone in my first year for the fun times outside of school, and for the many many hours spent together doing homework sets from "certain" classes. Thanks to my advisor for organizing our annual group retreat at Mammoth - starting there I became an avid skier and have had a lot of fun shredding at various resorts with Kostas, Reid, John, Yang, Xiaomin, Siteng and many others from Caltech. I would like to thank my friends (Sheng, Jize, Yang, Xinying and many many others) for all the joy they brought over various events such as the routine Friday board/video game nights, regular badminton games and road trips. In particular, I would like to thank Jize for being a wonderful badminton partner and for finding the opportunity to get professional training on men's double from Tony Gunawan. I would also like to thank Jenni for her tireless help on my logistics and travel, to thank Laura and Daniel from ISP who have made my life at Caltech as an international student a lot easier, and to thank Erin and Emma from the writing center for their invaluable help on improving my writing skills.

Lastly, I would like to express my heartfelt gratitude to my parents for their unconditional love, and for their unweavering support to me on pursuing a career that I am truly passionate about. They have also taught me so many things and I am extremely fortunate to have them as my family.

ABSTRACT

From concrete gravels unloaded from trucks to wheat seeds discharged through funnels, from polymeric beads filled in shoe cushions to metallic pellets packed in robotic grippers, granular matter is becoming increasingly relevant in coping with our evolvingly sophisticated societal needs in many respects (e.g. expanding urbanization, growing population and advancing manufacturing). This increasing relevance urges developing micro-structural understandings of granular matter regarding its two basic macro-scale behaviors: flowing heterogeneously and morphing adaptively. However, findings in this regard so far suffered from a disconnection in length-scale - some adopting a top-down perspective lacking predictability due to few insights taken from underpinning micro-scale details (e.g. particle shape), while others adopting a bottom-up perspective lacking practicality due to few specificities incorporated from overlaying macro-scale conditions (e.g. heterogeneities).

In this dissertation, via Discrete Element Method (DEM) simulations, we bridge the divide between length-scales in this regard by revealing the fundamental role of microstructures. To begin with, we evaluate and verify the robustness of DEM in capturing granular microstructures, by systematically comparing simulation results with experimental measurements on quasi-statically sheared granular assemblies. Then, we first numerically study spatial phase transitions in heterogeneous granular flows from a top-down perspective. We start by calibrating and validating a DEM model using experiments we perform on fluidizing spherical particle pile formed in a rotating drum. We next take the validated model to produce flows with different microstructures by systematically varying boundary condition and loading rate, and lastly we study their correlations with phase transitions ranging from gas-like layers near the free surface, to underneath liquid-like layers, and to solid-like layers deep in the bulk. We propose a micro-scale parameter quantifying the level of structural anisotropy, that can for the first time elucidate the spatial phase transitions between these layers independent of imposed boundary conditions and loading rates. Further, we find that, in solid-like layers, this micro-structural quantity correlates to bulk effective friction, an integral macro-scale quantity in constitutive modeling. Next, we numerically study bending modulus adaptations in shape-morphing granular sheets from a bottom-up perspective. We start by calibrating and validating a DEM model using experiments we perform on bending 3D printed granular sheets enclosed in a flexible membrane. We next take the validated model to construct granular sheets with different microstructures by varying constituent particle shape, initial configuration and confining pressure. Lastly we study the correlation between microstructure variations and modulus adaptations. We discover a universal power-law correlation between bending modulus (a macro-scale quantity) and coordination number (a micro-scale quantity) in reminiscence of the canonical power-law scaling for packings of frictionless sphere near jamming. We also find larger coordination number favors interlocked particles over non-interlocked ones, leading to significantly better shape-morphing performance of chain-like sheets over discrete assemblies.

PUBLISHED CONTENT AND CONTRIBUTIONS

(* denotes equal contribution)

Liuchi Li, Eloïse Marteau, and José E. Andrade (2019). "Capturing the inter-particle force distribution in granular material using LS-DEM." In: *Granular Matter*. doi: 10.1007/s10035-019-0893-7, pp 21-43. ISSN: 1434-7636.
The author participated in the conception of the project, carried out numerical studies, processed and analyzed the data, co-wrote the manuscript, and participated in manuscript revision.

Liuchi Li and José E. Andrade (2020). "Identifying spatial transitions in heterogeneous granular flow." In: *Granular Matter*. In press. ISSN: 1434-7636.
The author proposed the concept of the project, carried out experimental and computational studies, processed and analyzed the data, co-wrote the manuscript, and participated in manuscript revision.

Yifan Wang*, Liuchi Li*, Douglas Hofmann, José E. Andrade, and Chiara Daraio (2020). "Architectured granular sheets with adaptive stiffness." In preparation.
The author participated in the conception of the project, carried out numerical studies, co-analyzed the data, and co-wrote the manuscript.

TABLE OF CONTENTS

LIST OF ILLUSTRATIONS

LIST OF TABLES

Chapter 1

INTRODUCTION

1.1 Objective and Scope

This dissertation focuses on the type of granular matter that is composed of cohesionless, rigid and weakly polydisperse particles. Within this scope, the objective is to bridge length-scale divide by linking macro-scale behaviors of granular matter to the underpinning micro-scale details. Specifically, employing advanced computational and experimental techniques, we study the fundamental role of granular microstructures in elucidating spatial phase transitions in heterogeneous flows from a top-down perspective, and in elucidating bending modulus adaptations in shape-morphing assemblies from a bottom-up perspective.

1.2 Background and motivation

Granular matter and the major challenges

Granular matter can be defined as aggregates of athermal and frictional solid particles with size greater than one micrometer. From gravels in landslides to polymer beads filled in shoe cushions, granular matter is becoming increasingly relevant in coping with our evolvingly sophisticated societal needs. For instance, the participation of granular matter is required for mitigating geophysical hazards (e.g. landslides), optimizing relevant industrial processes (hopper discharge of wheat seeds), and rationally designing adaptive mechanical systems (e.g. soft robotics). Major challenges thus face us in developing better understandings towards the behaviors of granular matter regarding their two basic macro-scale behaviors: flowing heterogeneously and morphing adaptively.

The first aspect, flowing heterogeneously, features spatial phase transitions which often require minimum confinement (e.g. an open-end channel), thereby allowing the constituent particles to move freely upon shear. Spatial phase transitions show up in virtually any granular flow encountered in both geophysical hazards (e.g. landslides and snow avalanches) and industrial processes (e.g. hopper discharges and tumbler mixings). Specifically, unlike in homogeneous flows, in heterogeneous flows the strain rate gradient and stress gradient are no longer zero and multiple phases (solid-like, liquid-like and gas-like) can coexist in space. In other words, the phases that particles collectively exhibit can transit spatially in certain directions. A classical example is shown in Fig.1.1(a), where glass beads are being poured over a pile. We can clearly observe, along the direction perpendicular to the slope, three different layers corresponding to three different phases: first a gas-like layer near the free surface where beads bounce around randomly in all directions creating a dilute chaotic media; then this gas-like layer transitions into a liquid-like layer lying underneath where beads move freely in a more coherent manner; finally this liquid-like layer transition into a solid-like layer lying deep in the bulk where beads creep slowly. The last solid-like layer can not be observed easily with our naked eyes, but becomes apparent under cameras whose shutter speeds are adjusted appropriately. As shown in Fig. 1.1(b), as the shutter speed is gradually increased, the apparent “frozen" layer lying deep in the bulk is seen to flow with growing thickness. In particular, the smooth transition into such solid-like layers with non-zero velocity challenges the classical $\mu(I)$ granular rheology model [34, 60, 78] established about 20 years ago. This model would otherwise predict a sharp transition into solid-like layers where particle velocities identically vanish. The apparent deviation of predictions from experiments is believed to be attributed to the intrinsic locality that this model (termed as local rheology herein) relies upon (see Fig.1.1(c)): (i) the effective bulk friction $\mu = \tau/P$ of a steadily flowing granular media at any given location, depends monotonously in an increasing manner on the inertia number $I = \dot{\gamma}\bar{d}\sqrt{\frac{\rho}{P}}$ *only* at the same location, and (ii) there exists a critical yield stress value μ_s that depends *only* on particle properties (e.g. surface friction and shape), below which flow is not possible (i.e. particle velocities are identically zero). The inertia number I can be viewed as a competition between two timescales $I = t_c/t_s$ with $t_s = 1/\dot{\gamma}$ and $t_c = \bar{d}\sqrt{\rho/P}$, where t_s is the macro-scale shear time and t_c is the micro-scale particle relaxation time (see Fig.1.1(d)). Thus, in short, this model describes granular materials as Bingham-like plastics that are shear-thinning when they flow. Here, τ, P, $\dot{\gamma}$, ρ and $\bar{d}$ are shear stress, pressure, shear rate, material density and mean particle size, respectively.

Holding the rheology’s local nature responsible, researchers began to assume that granular flows are non-local in the sense that particle motions at different locations within flowing granular media are strongly correlated. This non-locality narrative also seems to offer reasonable explanations for other phenomena that the local rheology also failed in capturing. For instance, a shallower granular layer deposited over an inclined plane requires large slope angle in order to flow [92, 93]; stirring beads only at the bottom of a box fluidizes the whole bead assembly [84, 99]. On the other hand, observations of particle “clusters” formations [17, 79] in simple systems

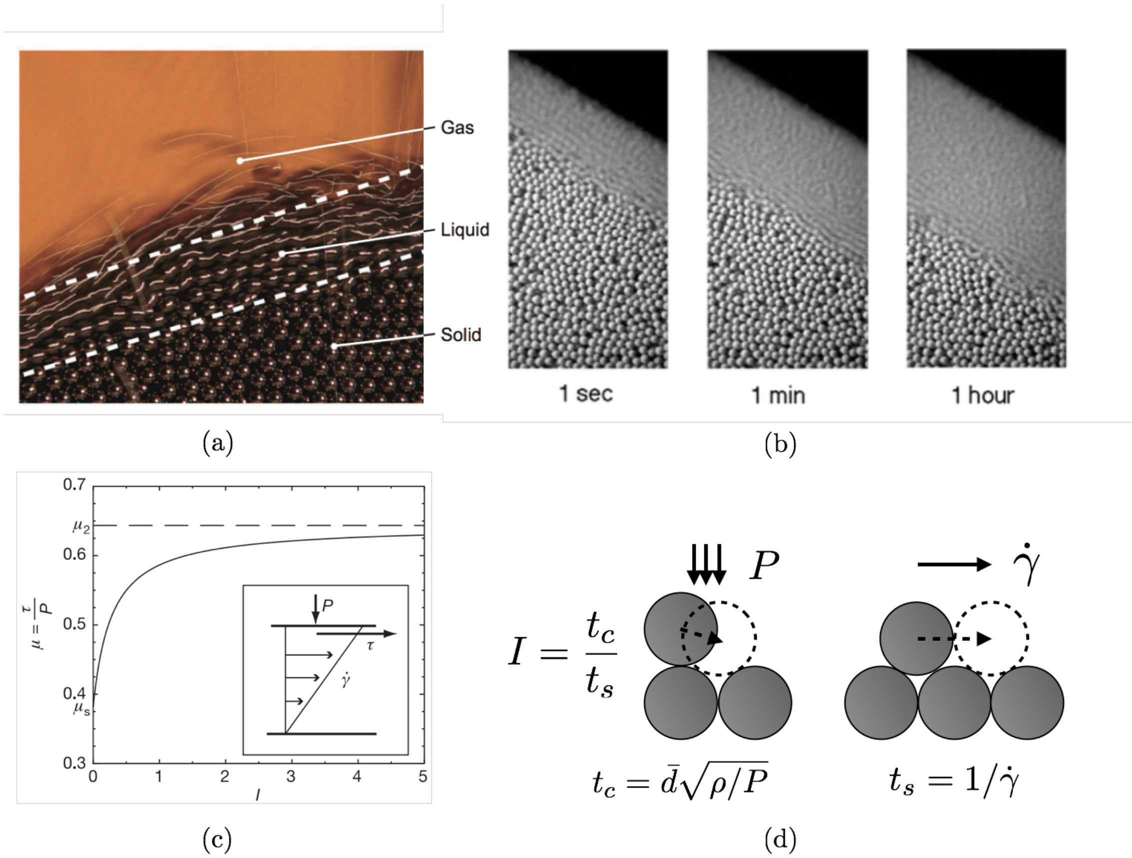

Figure 1.1: Heterogeneous flows with spatial phase transitions and the state-of-the-art rheological law. (a) An example of heterogeneous granular flow formed as steel beads being poured on a pile. Source: reprinted from [43]. (b) Creep motion in solid-like layers becoming obvious as camera shutter speed is increased from 1 sec to 1 min and to 1 hour. Source: reprinted from [66]. (c) One-to-one relationship between bulk effective friction μ and inertia number I with a yield stress ratio μ_s with parameters calibrated for glass beads. Source: reprinted from [60]. (d) Inertia number I as a competition between micro-scale particle relaxation time t_c and macro-scale shear time t_s.

additionally hint on the relevance of non-locality. Since around ten years ago, several non-local models based on the local rheology started to emerge. These models appear to be different on their respective mathematical formulations, but more fundamentally they are proposed with very different (and sometimes controversial) theoretical interpretations regarding "non-local" effect. Accordingly, there have been controversial opinions on the source of non-locality to consider (e.g. solely from particle interactions [35, 94] or further including boundary perturbations [4, 79]), on the choice of propagator to represent the source of non-locality [20, 61, 121], on the order of the chosen propagator's gradient to spread non-locality [20, 61, 106], and on the direction along which the non-local length-scale diverges as approaches jamming [20, 61, 106]. As a consequence, these models provide little insight regarding the condition under which non-locality manifests, they are often geometry-specific, and their performances depend sensitively on specific boundary conditions. These limitations highlight the essential but missing step to begin with, a top-down step that provides micro-structural understandings of spatial phase transitions in heterogeneous granular flows, and a step which will be integral to establishing a unified interpretation of "non-locality".

Unlike the first aspect, the second aspect, morphing adaptively featuring modulus adaptations often require certain level of confinement (e.g. a flexible membrane), thereby preventing the constituent particles from moving freely upon loading. Modulus adaptations are essential ingredients enabling the functionality of shape-morphing granular assemblies that may find many applications in the fields of medicine and manufacturing. In general, modulus adaptations emerge either from solely changing the external conditions (e.g. varying confining pressure), or further from additional variations of the internal conditions (e.g. varying constituent particle properties). For instance, for simple granular matter, an adaptive bulk modulus emerges from varying the vacuum level on flexibly confined granular assemblies, enabling the realization of universal robotic grippers (see Fig.1.2(a)), which excels at fast gripping of complex objects [24]. For more complex granular chains [123](see Fig.1.2(b)), an adaptive bulk modulus can also emerge from a combination of varying externally the indentation depth and varying internally the individual chain length [37], manifesting as strikingly tunable strain stiffening that has many practical implications in industry. Relevant work also reported on realizations of free-standing and even load-bearing granular structures by simply varying the shape of constituent particles (see Fig.1.2(c)). Examples are Z-shaped [82] and staple-shaped [48] particles.

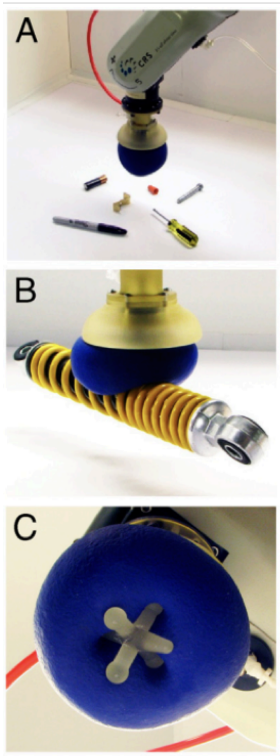

(a)

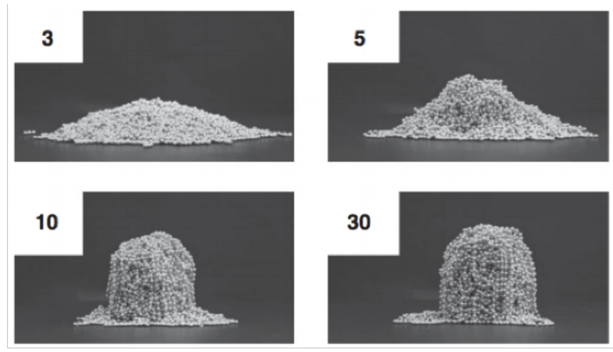

(b)

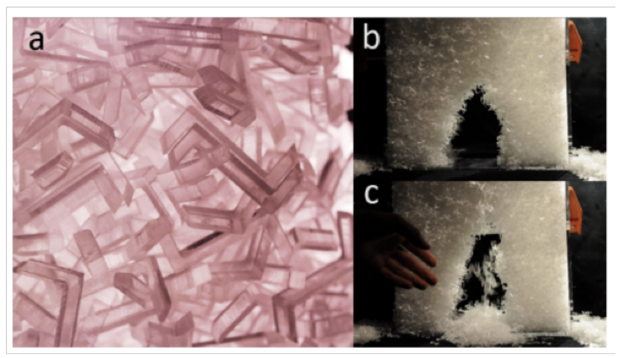

(c)

Figure 1.2: Examples of granular-based systems with adaptive mechanical modulus (a) Robotic gripper constructed by filling a blue flexible membrane with ground coffee; the three sub-images show its ability of grabbing objects with complex morphology. Source: reprinted from [24]. (b) Assemblies of granular chains evolve their morphology from pile-like to column-like with increasing bulk modulus; numbers shown at the upper-left corner of each sub-image indicate the number of beads connected per chain. Source: reprinted from [37]. (c) Free-standing granular structures shown as collections of inter-twined Z-shaped particles. Source: reprinted from [82].

On the realization side, self-evidently, similar or even more robust experimental realizations regarding shape-morphing granular assemblies will appear in the future. Such granular assemblies will most likely be designed in a bottom-up fashion by taking their internal conditions to more sophisticated levels, by means of rapidly advancing fabrication and testing techniques (e.g. additive manufacturing). For instance, particles with virtually any morphology, size-distribution and deformabilities can be fabricated via 3D printing. However, on the theoretical side, developments guiding efficient design seem to be focusing on highly idealized systems (e.g. frictionless spheres [85] or other simple shapes [75, 117] under negligible boundary effects such as periodic boundaries [30, 85, 120]). As such, their relevance remains questionable for strategically designing robust shape-morphing granular assemblies. In this regard, such theoretical limitations call for micro-structural understandings of modulus adaptations in shape-morphing granular assemblies that often involve complex boundary effects and internal conditions.

Understanding through granular microstructures

Again, as granular matter is intrinsically discrete, developing a better understanding of their macro-scale behaviors pivots on investigating the underpinning non-negligible microstructures formed collectively from frictional interactions between constituent athermal particles. In general, granular microstructures can be reflected by three kinds of micro-structural quantities that range from lower-order to higher order within each kind: geometrical-type ones containing information about particle arrangements, mechanical-type ones containing information about inter-particle forces, and kinematical-type ones containing information about particle motions.

- **Geometrical-type micro-structural quantities**. Examples include volume fraction (lower order) which is defined as the total volume of particles divided by the total volume they occupied; coordination number (lower order) which is defined as the average contact number per particle; probability distribution of "rigid clusters" [17, 80] in terms of their number and their geometrical properties such as radius of gyration, a rigid cluster is defined as a sub-collection of "caged" particles that are mutually in contact, and whose local packing fraction all exceed a certain threshold (e.g. 0.6 for disk [80]); Portion of particles with different number of contacts (higher order) [8], bond orientational order parameters (BOOP, higher order) [74] which quantify how close the local particle arrangement is compared to ordered patterns (e.g. hexagonal pattern); probability distribution of contact normals in polar coordinates (also known as the fabric, higher order) [13, 103] which can be represented by a second-order symmetric tensor $\langle n \otimes n \rangle$, here "$\langle \cdot \rangle$" denotes spatial average over all contacts and "n" is the contact normal (a unit vector) of a single contact. Additionally, the associated principal direction (the one corresponding to the largest eigenvalue) indicates the preferred contact direction (i.e. the direction along which major contacts appear, higher order).

- **Mechanical-type micro-structural quantities**. Examples include the probability density distribution (*p.d.f*) of both normal and tangential contact forces (lower order) [13, 103]; pair correlation functions of contact forces [73] which quantifies the directional and spatial correlation of contact forces; polar diagram of normal contact forces, tangential contact forces, and friction mobilizations (higher order) [13, 103, 111] which can be computed by evaluating in magnitude the average of normal contact forces, tangential contact forces and tangential contact forces divided by normal contact forces in every polar direction, respectively; the preferred direction of force transmissions (i.e. the direction along which dominant contact forces appear, higher order). In particular, in dense packing with enduring inter-particle contacts, the preferred direction of force transmissions essentially indicates the direction of *force chains* [8]. This direction can be computed as the dominant principle direction of a second-order symmetric tensor "$\langle |f| n \otimes n \rangle$" where "$|f| = \sqrt{|f_n|^2 + |f_t|^2}$" is the magnitude of total contact force at each contact with "$|f_n|$" the magnitude of normal contact force and "$|f_t|$" the magnitude of tangential contact force. Oftentimes the contribution from the tangential force is negligible, thus the preferred direction of force transmissions can also be computed from normal contact forces alone, i.e. can be defined as the dominant principle direction of "$\langle |f_n| n \otimes n \rangle$."

- **Kinematical-type micro-structural quantities.** Examples include velocity fluctuation magnitude (lower order) defined as the root of *granular temperature* [107] which is the mean square of velocity deviations (from mean particle velocity); pair correlation functions of velocity fluctuations [15, 93] which quantify the directional and spatial correlation of particle motions; and probability distribution of granular "clusters" (or granular eddies [17, 64, 79], higher order) in terms of their number and their geometrical properties such as radius of gyration, where a granular cluster is defined as a sub-collection of particles that are mutually in contact and whose motions are cooperative enough. Common practice in determining motion cooperativity is to look at the angle formed by the velocity fluctuation directions associated with two contacted particles. If the angle is less than a certain threshold (e.g. 30°), the two contacted particles then belong to the same granular "cluster."

Despite the seemingly abundant investigations on granular microstructure, most studies in this regard (both experimental and computational), as we have briefly mentioned in the previous subsection, have been focused on simple and homogeneous systems with no stress or strain (rate) gradient, and under either rigid or periodic boundaries. These studies indeed have identified many fundamental perspectives on granular materials, for instance, the bimodal character of force transmissions [97], the contact and force anisotropy induced by shear [73], and the divergence of rigid cluster size as approaching jamming [80]. However, their practical implications on heterogeneous systems (e.g. heterogenous flows) remain elusive. Further, it is unclear how relevant these conclusions are in helping understand systems with flexible boundaries (e.g. shape-morphing granular assemblies). Therefore, the major task of this dissertation is to bridge the divide in length-scale by elucidating the fundamental role of the underpinning microstructures in furnishing overlaying macro-behaviors of granular matter, specifically, in elucidating spatial phase transitions in heterogeneous granular flows and bending modulus adaptations of shape-morphing granular sheets.

Relevant experimental and computational techniques

Having presented the challenges that need to be addressed, it is now the time to identify the tools needed in order to perform analysis. As our focus is on granular microstructures, computational techniques can show great advantages over current experimental techniques, especially when analyzing three-dimensional systems. Although our work is mostly computational, we make sure first our computational results can faithfully reproduce experimental observations (mostly) at the macro-scale. In the following we briefly introduce the experimental and computational techniques involved in our work.

- **Discrete Element Method, DEM** [33]. Given a model for particle interaction, DEM resolves the dynamics of each simulated particle by numerically integrating Newton's law. Detailed particle-scale information can be easily obtained from DEM simulations (e.g. particle positions, velocities, rotations, and contact forces). In particular we will mainly use a DEM-variant method called LS-DEM [62, 63] that is able to simulate particles with arbitrary shape. DEM will be the major tool in our work to get access to micro-scale details (e.g. granular microstructures).

- **Granular Element Method, GEM** [54]. Combining experimental imaging techniques (e.g. Digital Image Correlation, DIC [47]) with equations governing particles' mechanical behaviors, GEM allows contact force inference in cohensionless granular materials with particles of arbitrary shape, texture and opacity. We use GEM in our work to experimentally get access to micro-scale details. These measurements are used to test and verify the robustness of

DEM in capturing microstructures (especially those related to contacts and contact forces) of granular assemblies upon loading.

- **Particle Image Velocimetry, PIV** [116]. PIV is an image analysis tool widely used in experimental fluid mechanics for measurements of kinematical fields of fluids. PIV has also gained applications in flows of granular matter. We use PIV in our work to measure the velocity field of heterogeneous flows of glass beads in a rotating drum. The measurements are used to calibrate and validate our DEM model.
- **3D printing**. 3D printing is useful in accurately fabricating particles with very complex morphology. In our work we use 3D printing to fabricate digitally designed granular sheets.

1.3 Thesis outline

The layout of this dissertation is as follows:

In Chapter 2, we evaluate and validate the robustness of DEM in capturing granular microstructures obtained from experiments. We utilize a DEM-variant technique, LS-DEM [62, 63] that is able to simulate the dynamics of arbitrarily-shaped particles by representing each particle as a level-set function. Using LS-DEM, we conduct one-to-one 2D simulations in comparison with experiments by exactly replicating the initial configurations and particle morphologies. We consider simple shear of collections of circular-shaped and arbitrarily-shaped columns, both of which are 3D printed to preserve the designed particle shape and size. We compare experiments and simulations at both the macro-scale and the micro-scale. At the macro-scale, we compare the evolution of the homogenized Cauchy stress tensor in its three components and the evolution of vertical dilation ratio; at the particle-scale, we compare the evolution of microstructures in terms of (i) the probability distribution of contact normals in polar coordinates, (ii) the polar diagram of contact forces, and (iii) the polar diagram of friction mobilizations. We show that, with minimum calibration efforts, DEM (LS-DEM) is able to capture both macro-scale and micro-scale responses measured from experiments.

In Chapter 3, with the confidence in DEM built in the work showed in Chapter 2, we take DEM to analyze phase transitions in heterogeneous flow developed at the center of rotating drums from a top-down perspective. We first perform experiments of glass beads flowing in a rotating drum, measuring at the drum center the dynamical angle of repose and down-stream velocity for three different drum rotation speeds.

We use these measurements to calibrate and validate a DEM model, which is later taken to produce various microstructures by systematically varying boundary conditions (drum width and side wall friction) and load rates (rotating speeds). We then study the correlations of these microstructures to the spatial phase transitions from gas-like layers near the free surface, to underneath liquid-like layers, and finally to solid-like layers deep in the bulk. We propose a micro-scale parameter quantifying the structural anisotropy by measuring the overall deviation of preferred direction of inter-particle contacts to preferred direction of inter-particle force transmissions. We show that this quantity elucidates the phase transitions between these layers independent of boundary condition and loading rate. Further, we show that, in solid-like layers, this micro-structural quantity correlates to bulk effective friction, which is an integral macro-scale quantity in constitutive modeling.

In Chapter 4, we take DEM to analyze modulus adaptations in shape-morphing granular sheets , from a bottom-up perspective.We first fabricate architected granular sheets by 3D printing interlocked solid particles following a certain interlocking pattern. Depending on the level of imposed isotropic pressure via vacuuming, we show by three-point bending tests the exceptionally tunable bending modulus of the jammed sheets. We next calibrate a DEM model based on our experimental measurements and take the validated model to construct granular sheets with different microstructures by varying constituent particle shape, initial configuration and imposed isotropic pressure. Lastly we study the correlations of microstructure variations with modulus adaptations. We discover a universal power-law correlation between bending modulus (a macro-scale quantity) and coordination number (a micro-scale quantity) with the scaling exponent being independent of investigated particle shapes and imposed isotropic pressures, in a way reminiscent of the canonical power-law scaling for frictionless sphere packing near jamming. We also find larger coordination number favors interlocked particles over non-interlocked ones, leading to significantly better shape-morphing performance of chain-like sheets over discrete assemblies.

In Chapter 5, we conclude by summarizing the major results of this work and presenting future outlook.

Chapter 2

CAPTURING THE INTER-PARTICLE FORCE DISTRIBUTION IN GRANULAR MATERIAL USING LS-DEM

Liuchi Li, Eloïse Marteau, and José E. Andrade (2019). "Capturing the inter-particle force distribution in granular material using LS-DEM." In: *Granular Matter*. doi: 10.1007/s10035-019-0893-7, pp 21-43. ISSN: 1434-7636.

Abstract

Particle shape, as one of the most important physical ingredients of granular materials, can greatly alter the characteristic of inter-particle force distribution which is of vital importance in understanding the mechanical behavior of granular materials. However, currently both experimental and numerical studies remain limited in this regard. In this paper, we for the first time validate the ability of the level set discrete element method (LS-DEM) of capturing the inter-particle force distribution among particles of arbitrary shape. We first present the technical details of LS-DEM; we then apply LS-DEM to simulate experiments of shearing granular materials composed of arbitrarily shaped particles. The proposed approach directly links experimentally measured material properties to model parameters such as contact stiffness without any calibration. Our results show that LS-DEM is able to not only capture the macro-scale response such as stress and deformation, but also to reproduce the particle scale contact information such as the distribution of contact force magnitude, contact orientation and contact friction mobilization. Our work demonstrates the promising potential of LS-DEM on studying the mechanics and physics of natural granular materials, and on aiding the rational design of granular particle shape for novel macro-scale mechanical property.

2.1 Introduction

Any collection of macroscopic solid frictional particles with a size greater than 1 μm belong to the family of granular materials. They are ubiquitous on earth and are the second most manipulated industrial material [101]. Despite such a unified and simple definition, at the macro-scale, different granular materials can exhibit drastically different mechanical properties and can behave like solids, liquids, gases, or even with the aforementioned phases coexisting [56, 57] under different external loading and boundary setting. Such complex macro-scale behavior is closely tied to the heterogeneously distributed force chains formed by inter-particle forces [55, 73], the characteristic of which is sensitive to particle shape effect [5, 27]. However, investigations on the force transmission among arbitrarily shaped particles are still lacking due to several technical limitations both experimentally and computationally.

On one hand, most experimental studies so far involving measuring inter-particle forces rely on advanced optical techniques (for example refractive index matching tomography [23] and 3D x-ray diffraction and x-ray tomography [52]) that are able to reasonably measure particle scale deformation. Because of this, these methods often require the test material to have specific properties such as being birefringent [73] for photo-elasticity measurement or exhibiting optically detectable particle deformation for GEM measurement [54]. As such, they can only handle a very limited number of particles (typically in the order of magnitude of 100 [23] or even less for complex particles such as sands [54]). As such, experimentally it still remains a challenge to incorporate particle shape effects into the study of inter-particle force distribution.

On the other hand, due to recent advances in numerical techniques, relevant investigations have also been carried out based on discrete methods. In general all discrete methods aim at simulating the kinematics of a system of particles but in two different ways: either explicitly by penalizing the inter-particle penetration based on a certain contact model, known as the (classical) discrete element method (DEM) [33], or implicitly by solving a linear complementarity problem (LCP) with non-equality constraint for all particle contacts under the limit of infinite particle rigidity, known as the non-smooth contact dynamics (NSCD) [58]. In the rigid grain limit (which is usually the case for most granular material application [34]), these two methods have been shown to give similar results and we refer to [88] for a detailed discussion and comparison between DEM and NSCD. Such numerical techniques have been employed to characterize the inter-particle force network of granular media ranging from disk assembly in the late 90's [96, 97] to assemblies of pentagonal particles [9], elongated particles [6, 7], polyhedras [10], to assemblies composed of poly-disperse particles [12, 119] dated ten to five years ago, and to investigate granular pile instability based on friction mobilization analysis of particle contacts [111, 112]. However, in all current NSCD based numerical methods, usually all contact type between a certain shaped particle must be identified and be pre-built into the algorithm for contact detection and computation. As such it can only handle a system of particles with either identical and simple shape such as isotropically shaped polygons [9] or the so-called RCR particles [7], or with a very limited number of elementary particle shape type (mixture of sphere and RCR particles in [14] and mixture of cube, sphere, ellipsoid and cylinder in [88]). Another general class of DEM variant method utilizes sphere (disk) clumps [41] that can handle systems of particles with different shapes, however since the number of spheres (disks) needed to approximate one particle scales up dramatically fast with the change of particle shape, this method can be computationally intractable in simulating systems of complex-shaped particles. Therefore, while many granular materials commonly seen in nature such as sand are composed of particles with different and complex shapes, numerically our understanding is mostly limited to particles with simple shapes besides sphere (disk). More importantly, although many qualitative agreements can be found with experimental studies such as the appearance of strong and weak force network [73] and the shear-induced alignment effect on inter-particle force distribution [40], there has been no direct validation of the inter-particle force distribution computed from classical DEM or NSCD.

In summary, experimental investigations are limited by particle property, shape, and system size; while numerically these limitations become much less of an issue, the corresponding conclusions have never been directly validated. An important question to ask is: is there a numerical technique, with computationally tractable expense, that is able to capture the inter-particle force distribution among particles with different arbitrary shapes?

In this paper, we attempt to answer this question − we for the first time validate the ability of a newly developed DEM variant method called LS-DEM [62] on capturing the inter-particle force distribution among particles with arbitrary shape by using a recently developed experiment technique that is able to quantitatively measure inter-particle forces [77]. The paper is structured as follows: in section two, we present the technical details of LS-DEM; in section three, we first discuss a set of experiments that allow us to measure inter-particle forces in granular materials, then introduce the corresponding numerical simulations and lastly validate LS-DEM by comparing simulation results with experiment measurements; in section four, we outline the conclusions of this study and implications for future work.

2.2 Comparison between LS-DEM and DEM

LS-DEM [62] works in principle just like DEM: for each particle in a system, denoted as particle i here, once knowing all forces $\boldsymbol{f}_i$ acting on it, DEM (and LS-

DEM) simulates its dynamics by numerically integrating Newton's equations of motion for the translational and rotational degrees of freedom:

$$m_i \frac{\mathrm{d}^2 \boldsymbol{r}_i}{\mathrm{d}t^2} = \boldsymbol{f_i}, \quad \text{and} \quad \frac{\mathrm{d}}{\mathrm{d}t}(\boldsymbol{I}_i \cdot \boldsymbol{\omega}_i) = \boldsymbol{T}_i \tag{2.1}$$

with the mass m_i of particle i, its position $\boldsymbol{r}_i$, the total force $\boldsymbol{f}_i$ acting on it due to contacts with other particles, with boundaries or due to external body force field, the 3×3 inertia matrix $\boldsymbol{I}_i$ (in 3D), its angular velocity $\boldsymbol{\omega}_i$ and the total torque $\boldsymbol{T}_i$ acting on it. DEM treats each simulated particle as rigid but allows a small interpenetration d to compute the contact force $\boldsymbol{f_i}$ and moment $\boldsymbol{T}_i$ based on a chosen contact model. There are many contact models developed with different level of sophistications: Herztian or Hookean contact with particle scale damping[34, 108], incorporation of rolling resistance [2, 38], consideration of hysteresis [72] etc. A detailed introduction to various contact models can be found in [68]. In our study, the total force $\boldsymbol{f}^{j,i}$ (for simplicity we hereafter omit the superscript and call it $\boldsymbol{f}$) exerted by particle j to i is computed based on the following formula:

$$\boldsymbol{f} = \boldsymbol{f}_n + \boldsymbol{f}_t \tag{2.2}$$

$$\boldsymbol{f}_n = k_n d \hat{\boldsymbol{n}} \tag{2.3}$$

$$\boldsymbol{f}_t = -\frac{\boldsymbol{\Delta s}}{|\boldsymbol{\Delta s}|} \min\left(k_t |\boldsymbol{\Delta s}|,\ \mu_s |\boldsymbol{f}_n|\right) \tag{2.4}$$

where $\boldsymbol{f}_n$ and $\boldsymbol{f}_t$ are respectively the normal and tangential component of $\boldsymbol{f}$; $\hat{\boldsymbol{n}}$ and $\boldsymbol{\Delta s}$ are respectively the contact normal and the accumulated tangential displacement; μ_s is the inter-particle friction coefficient; and $k_n(k_t)$ is the normal (tangential) contact stiffness with unit of force per area.

However, unlike DEM, LS-DEM is able to compute d and the corresponding contact force and moment among particles with various shape. In LS-DEM each individual particle is represented by two quantities: a set of spatially distributed points $\{\boldsymbol{x}_1, \boldsymbol{x}_2, ..., \boldsymbol{x}_n\}$ (nodes) discretizing the particle surface (called the mesh) and a discretized level set function $\phi(\boldsymbol{p})$ where $\boldsymbol{p}$ are the grid points with color indicating the signed distance to the grain surface (negative for inside and positive for outside), as shown in Figure 2.1(a). Accordingly the discretized level set function $\phi(\boldsymbol{p})$ is scalar-valued and implicit. While $\{\boldsymbol{x}_1, \boldsymbol{x}_2, ..., \boldsymbol{x}_n\}$ provides the information of particle geometry, $\phi(\boldsymbol{p})$ gives the signed distance of a certain point $\boldsymbol{p}$ to the surface of the particle which is formed by connecting $\{\boldsymbol{x}_1, \boldsymbol{x}_2, ..., \boldsymbol{x}_n\}$: $\phi(\boldsymbol{p}) > 0$ when $\boldsymbol{p}$ is outside the surface, $\phi(\boldsymbol{p}) = 0$ when on the surface and $\phi(\boldsymbol{p}) < 0$ when $\boldsymbol{p}$ is inside the surface. To detect contact between two particles, a master-slave approach is used, where we evaluate the value of all nodes of the master using the level-set function of the slave. If the value of the level set function is negative for any node, contact exists and force and moment are computed for each penetrating node, which are then summed to give the total contact force and moment between the two particles, as shown in Figure 2.1(b). In current LS-DEM implementation the contact model becomes:

$$\boldsymbol{f}_n = \sum_{z=1}^{P} \boldsymbol{f}_{n,z} = \sum_{z=1}^{P} k_n d_z \hat{\boldsymbol{n}}_z \tag{2.5}$$

$$\boldsymbol{f}_t = \sum_{z=1}^{P} \boldsymbol{f}_{t,z} = -\sum_{z=1}^{P} \frac{\boldsymbol{\Delta s}_z}{|\boldsymbol{\Delta s}_z|} \min\left(k_t|\boldsymbol{\Delta s}_z|,\ \mu_s|\boldsymbol{f}_{n,z}|\right) \tag{2.6}$$

where P is the total number of penetrating nodes of particle i into particle j; $\boldsymbol{f}_{n,z}$ and $\boldsymbol{f}_{t,z}$ are the normal and tangential forces computed at node z; d_z, $\hat{\boldsymbol{n}}_z$ and $\boldsymbol{\Delta s}_z$ follow the same definition, but are now computed at each node z. In this paper, however, we modify the contact model implementation to instead only consider the node with maximum penetration. By doing so, LS-DEM becomes mesh-independent in displacement controlled loading condition and converges to DEM in simulating circular particles (see Appendix A). Taking advantage of the level set function formulation, contact detection between two arbitrarily shaped particles become very trivial and require very little computational expense. For more technical details of LS-DEM, we refer to [62, 63].

2.3 Beyond DEM: capturing the mechanical response of granular material with arbitrarily shaped particles

In the previous section, we introduced the technical details of LS-DEM. In this section, we will show the ability of LS-DEM of capturing the macro-scale response and further capturing particle scale information of a system of particles with different arbitrary shapes. In order to do this, we first detail the experiments that allow us to measure both the macro-scale response and the particle scale information in particular the inter-particle forces, then explain our simulation setup, and lastly compare LS-DEM simulation results to experimental measurements.

Experiments: extract inter-particle forces in granular materials

Laboratory tests are carried out using a custom-built shear apparatus designed to subject a two-dimensional analogue granular assembly to (quasi-static) shear conditions [76, 77]. The shear mechanism is generated by a displacement-controlled linear actuator connected to the shear cell. Simultaneously, a vertical load σ_N is

(a)

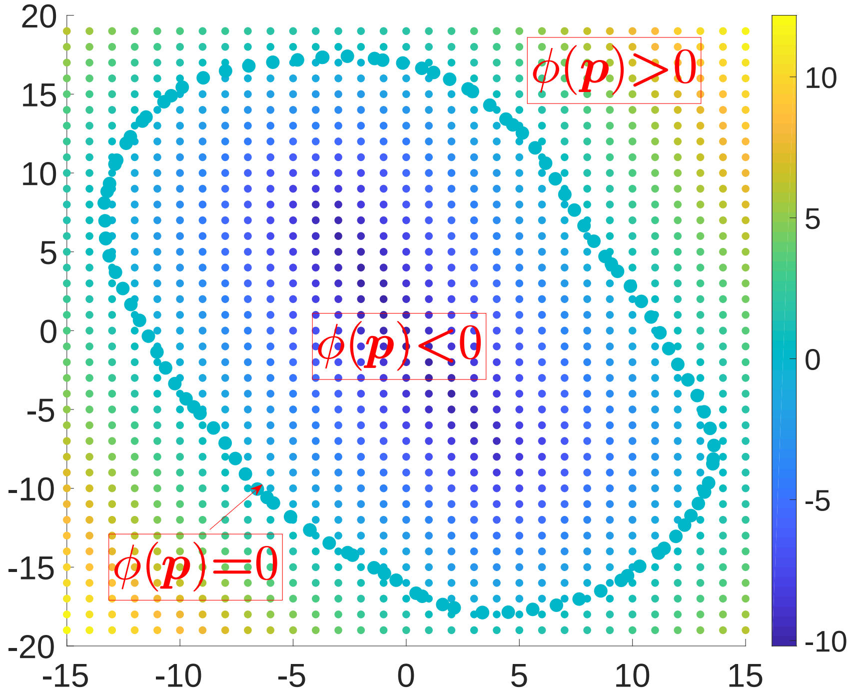

(b)

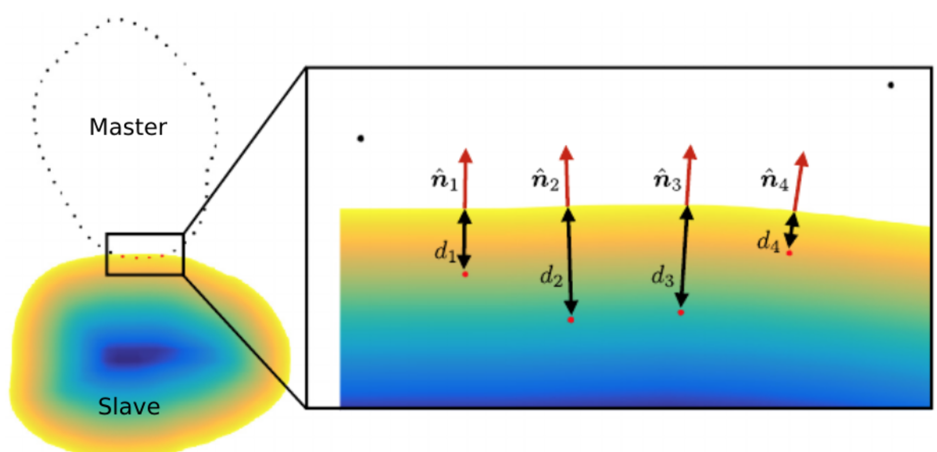

Figure 2.1: Examples of level-set construction and contact detection between grains. (a) An example of constructing one particle with arbitrary shape using level set function; surface points (nodes) are shown as the dots in cyan, overlaid grid points $\boldsymbol{p}$ represent the associated discretized level set function ϕ with color showing the signed distance to the surface: outside the surface $\phi(\boldsymbol{p}) > 0$, on the surface $\phi(\boldsymbol{p}) = 0$, and inside the surface $\phi(\boldsymbol{p}) < 0$. (b) Figure adapted from [63]: an example of contact detection between two particles: evaluate $\phi_s(\boldsymbol{x}_i^m)$ for every node $\boldsymbol{x}_i^m$ of the master particle against the level set function ϕ_s of the slave particle.

applied to the granular assembly confined in the shear cell through a dead weight loading system. The shear cell is a horizontal deformable parallelogram with one arm fixed to a support structure and is subjected to shear strain and normal strain in the y-direction while maintaining zero normal strain in the x-direction. At each load step, image processing techniques are employed to measure the length in the y-direction L_y and shear angle θ defined as the angle between the y-axis and the tilted side of the shear cell. Given these measurements, the components of the macroscopic strain tensor $\boldsymbol{\epsilon}$ are obtained as follows: $\epsilon_{xx} = 0$, $\epsilon_{yy} = \Delta L_y/L_y$, and $\epsilon_{xy} = 1/2 \tan\theta$, where ΔL_y is the change in length in the y-direction between the initial and deformed configurations. Images are acquired with an optical imaging system (Allied Vision Prosilica GT4907 15.7 Megapixel CCD camera attached to a Nikkor AF 105mm f/2.8 lens) that is installed above the apparatus.

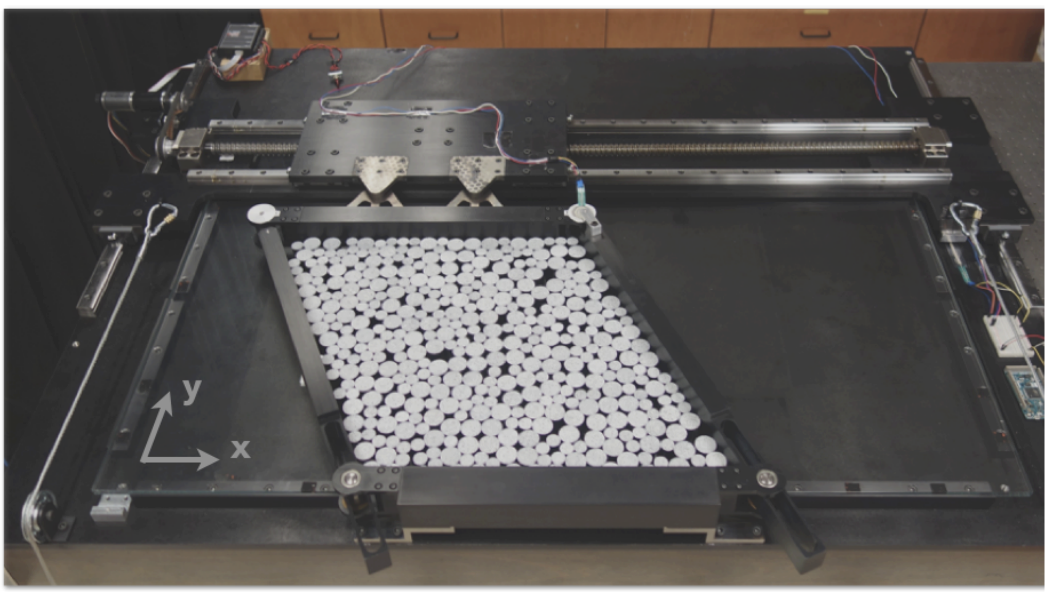

Figure 2.2: Picture of the experimental setup.

Experimental tests are performed on granular samples composed of either circular or arbitrarily-shaped grains. Both 2D analogue samples follow a log-normal distribution of grain diameter and are fabricated using the same rubber-like material (Stratasys FLX9895DM) and the same additive manufacturing technology (Stratasys Object500 Connex3 printer). All specimens were fabricated using the same additive manufacturing process. Factors such as the orientation of the print, support material composition and removal, and environmental conditions of storage of the raw materials were kept constant for all 3D-printing jobs. Such precautions were taken to ensure consistency in the effect of potential inhomogeneities and anisotropies.

While the particles in the experiments have been assumed to be elastic, isotropic and homogeneous, it is clear that this is not necessarily true, and the experiments rely on averaging the two independent bulk elastic constants over several measurements and macroscopic estimates of linear elastic behavior. Quantifying the degree of inhomogeneity and anisotropy in 3D printed materials is an open question in mechanics and lies outside the scope of our paper. Accordingly, the printed grains constituting the circular- and arbitrarily-shaped assemblies have the same mechanical properties, i.e. a Young's modulus E = 63 MPa and a Poisson's ratio ν of approximately 0.5. The height of the grains was set to 20 mm. The circular-shaped assembly has a total of N_p = 313 grains while the arbitrarily-shaped assembly is comprised of N_p = 398 grains. The arbitrarily-shaped assembly is engineered based on X-Ray Computed Tomography images of a sand sample (Caicos ooids) [71, 77]. 11 grain shapes are extracted for their different morphological properties (i.e. sphericity and roundness). The selected grain shapes are then copied and scaled to follow a log-normal distribution. Finally, a row of circular Teflon cylinders is added between the shear cell boundaries and the granular sample to ensure that the cell is sufficiently filled.

As the sample is sheared, we perform simultaneous measurements of particle- and continuum-scale quantities that govern the mechanical behavior of granular materials. At the particle-scale, the geometrical arrangement of the granular assembly, including the position of contact points and centroids, is characterized by means of image processing (i.e. the watershed segmentation algorithm [47, 104, 109] from Matlab Image Processing Toolbox). The 2D Digital Image Correlation (2D-DIC) software VIC-2D (Correlated Solutions, Inc., Columbia, SC, USA) [1] is used to measure the intra-particle full-field displacements and strains by comparing digital images in the undeformed and deformed configurations [87, 113]. The intra-particle full-field stresses are extracted from the strains assuming Hooke's law applies. Figure 2.3 shows an example of the measured strain field and computed stress field for the arbitrarily shaped particle assembly at shear angle θ = 13.9°. The normal and tangential inter-particle forces are inferred using the Granular Element Method (GEM) [3, 54, 76], provided that average particle stresses and contact point locations are known. Figure 2.4 presents experimental results of the intra-particle stresses and force networks obtained using the aforementioned measurement techniques at different shear angle θ in the circular- and arbitrarily-shaped assemblies.

At the macroscopic scale, the Cauchy stress tensor $\bar{\boldsymbol{\sigma}}$ is expressed as a function of the inter-particle forces and fabric [29] as follows:

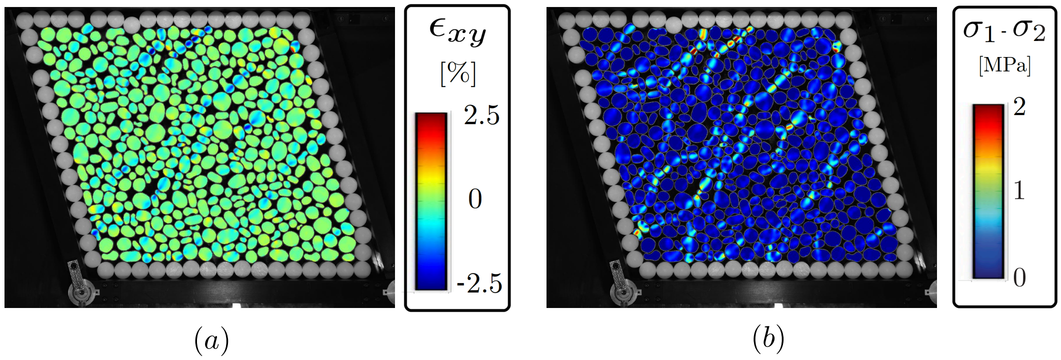

Figure 2.3: Measured strain field and computed stress field. (a): Measured shear strain field using DIC and (b): accordingly computed principle stress difference using the measured strain via Hooke's law.

$$\bar{\boldsymbol{\sigma}} = \frac{1}{V}\sum_{c=1}^{N_c} \mathrm{sym}(\boldsymbol{f}^c \otimes \boldsymbol{b}^c) \tag{2.7}$$

where N_c is the total number of contact points, V is the total volume of the granular assembly, $\boldsymbol{f}^c$ is the inter-particle force, and $\boldsymbol{b}^c$ is the branch vector at the contact c.

More details on the experimental setup, granular assemblies, and measurement techniques can be found in [76, 77].

LS-DEM simulations

Since the experiments are quasi-2D, we carry out 2D LS-DEM simulations − every simulated particle has a one-to-one correspondence to the one used in the experiment, as shown in Figure 2.5. In the following, based on the experimental setup, we discuss how we implement the boundary condition, choose the contact model and determine all parameters used in our simulations.

Boundary condition implementation

In order to properly implement the boundary boundary conditions, we start by drawing a free body diagram (Figure 2.6), in which we consider the boundary frame "AD-DC-CB" without the arm "AB" which is mounted to the table and fixed. In this way, under quasi-static loading condition, "AD-DC-CB" must always be in equilibrium by balancing all external forces: forces exerted by the particles (F_{kl}), forces imposed by the weight and shear-driving motor (F_N and F_h respectively) and reaction forces at the two slider (F_A and F_B). Taking the granular assembly as a whole with one stress state, firstly we can estimate the forces exerted by the particles

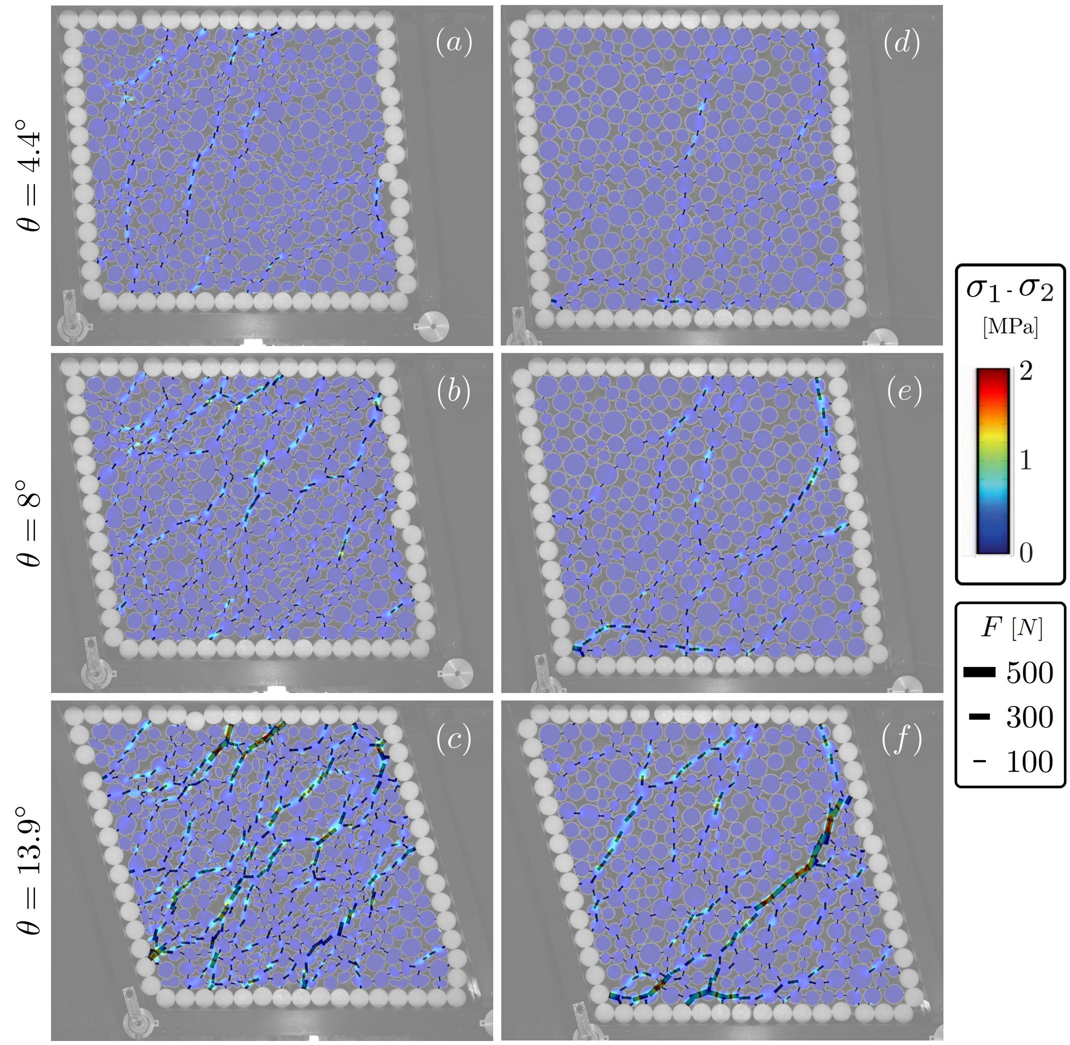

Figure 2.4: Inter-particle forces inferred with GEM superimposed on difference of principal stresses $\sigma_1 - \sigma_2$ at different values of shear angle θ for (a)-(c) the arbitrarily-shaped and (d)-(f) circular-shaped assemblies.

to the boundary as the following:

$$\boldsymbol{F}_{kl} = -\boldsymbol{\sigma}_\theta \cdot \boldsymbol{n}_{kl} S_{kl} \tag{2.8}$$

Where $\boldsymbol{\sigma}_\theta$ is the 2×2 stress tensor for the granular assembly at a shear angle θ, n_{kl} and S_{kl} are respectively the normal and cross-section area of each confining bar with kl = AD,DC or BC. By force equilibrium we can solve for F_A, F_B and F_h, all of which cannot be measured in our experiments (see Appendix B). In our implementation, we choose to take $(|\boldsymbol{F}_A| - |\boldsymbol{F}_B|)\sin\theta$ as an input in addition to F_N and θ, and compute the vertical dilation ratio $\epsilon_\theta = (h_\theta - h_0)/h_0 \times 100\%$ by moving DC vertically based on the force equilibrium in the y direction, where h_θ and h_0 are

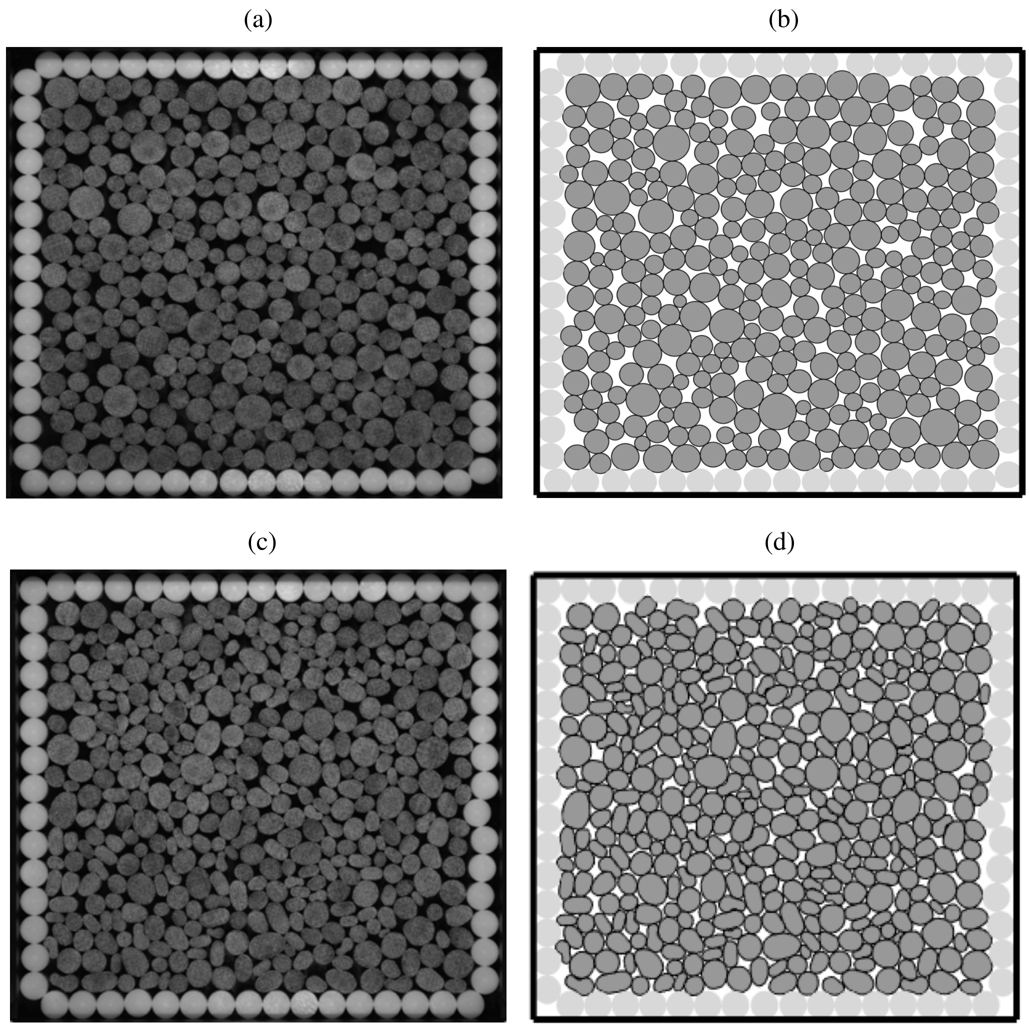

Figure 2.5: Experimental configuration and the one-to-one computational configuration. (a)(c): Initial configuration of the setup, (b)(d): corresponding 2D simulation setup for cylindrical particle case and arbitrarily shaped particle case; every simulated particle has a one-to-one correspondence to the one used in the experiment - same initial configuration, size, shape and density.

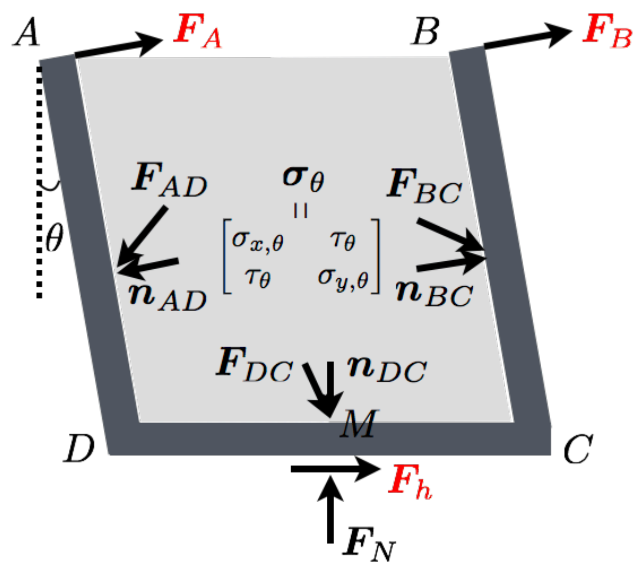

Figure 2.6: Free body force diagram of the boundary frame “AD-DC-CB". $\boldsymbol{F}_A$, $\boldsymbol{F}_B$ and $\boldsymbol{F}_h$ are not directly measured from experiment.

Input	F_N θ $(\lvert\boldsymbol{F}_A\rvert - \lvert\boldsymbol{F}_B\rvert)\sin\theta$
Output	$\epsilon_\theta = \frac{(h_\theta - h_0)}{h_0} \times 100\%$

Table 2.1: Simulation input and output of interest.

respectively the heights of the arm DC at a given shear angle θ and at $\theta = 0$. Table 2.1 shows the input quantities and also the output quantities of interest.

Contact between cylinders with parallel axes

In section two we presented the general contact model for our LS-DEM implementation. In this section we discuss the specific expression for each parameter such as k_n. In our experimental setup, for case one each contact takes place between two cylinders with parallel axes, we use the following applicable Hertzian contact theory that allows us to express the contact force F^c in the following way [91]:

$$F^c = \frac{\pi}{4} E^* L \delta \tag{2.9}$$

where E^* is the effective modulus and can be determined via $1/E^* = (1-\nu_1^2)/E_1 + (1-\nu_2^2)/E_2$ with ν_1, ν_2, E_1, E_2 being the Poisson's ratio and elastic modulus of the two contact cylinder respectively, L is the cylinder length, and δ is the indentation depth. Approximating δ by d, we accordingly determine the normal contact stiffness by:

$$k_n = \frac{\pi}{4} E^* L, \tag{2.10}$$

This model holds for contact between a cylinder and a flat surface by treating the flat surface as a cylinder with infinite radius. We assume that such model also holds for contact between two arbitrarily shaped particles with parallel axes. In DEM, common practice is to take $k_t = \beta k_n$ with $0.5 \leq \beta \leq 1$ [34, 62, 63, 108]. However, it is found that simulation results are not sensitive to the particular value of β [108], we therefore keep the same ratio as in [63] by taking $\beta = 0.9$. In this way, all parameters of the contact model can be physically defined and directly determined from experimental measurements.

Parameter determination

To this point, all other parameters (k_n, β, μ_s) are introduced except two: global damping ξ and time step Δt, both of which are closely tied to the implemented time integration scheme in LS-DEM. In our study, for 2D we rewrite the equations of motion considering damping and use the centered finite difference integration scheme proposed in [70] for numerical integration:

$$m_i \ddot{\boldsymbol{r}}_i + \xi m_i \boldsymbol{v}_i = \boldsymbol{f}_i, \tag{2.11}$$

$$I_i \ddot{\boldsymbol{\alpha}}_i + \xi I_i \boldsymbol{\omega}_i = T_i, \tag{2.12}$$

$$\boldsymbol{v}_i^{n+1/2} = \frac{1}{1+\xi\Delta t/2}\left[(1-\xi\Delta t/2)\boldsymbol{v}_i^{n-1/2} + \frac{\Delta t}{m_i}\boldsymbol{f}_i\right], \tag{2.13}$$

$$\omega_i^{n+1/2} = \frac{1}{1+\xi\Delta t/2}\left[(1-\xi\Delta t/2)\omega_i^{n-1/2} + \frac{\Delta t}{I_i}T_i\right], \tag{2.14}$$

$$\boldsymbol{r}_i^{n+1} = \boldsymbol{r}_i^n + \Delta t \boldsymbol{v}_i^{n+1/2}, \tag{2.15}$$

$$\alpha_i^{n+1} = \alpha_i^n + \Delta t \omega_i^{n+1/2}, \tag{2.16}$$

where $\boldsymbol{v}_i^{n+1/2}$, $\boldsymbol{v}_i^{n-1/2}$, α_i^{n+1} and α_i^n are, respectively, the velocities and rotational positions of particle i at different discretized time step. The global damping ξ has a unit of inverse of time and dissipates the kinetic energy of each particle as if it is immersed in viscous fluid. We note that simulations are carried out in a loading rate faster than that imposed in experiment since it is computationally very expensive to use the real quasi-static loading rate. Accordingly, the introduction of ξ allows us to maintain quasi-static numerically by quickly dissipating kinetic energy, and helps with accounting for the dissipative frictional force between particles and the underlying glass plate that is not directly modeled in our simulation. We set Δt to be a small fraction of t_{tol} to maintain numerical stability, where t_{tol} is the characteristic binary collision time between two particles [72]. Now the complete parameter space of our LS-DEM model is

$$\wp = \begin{bmatrix} k_n, & \beta, & \mu_s, & \Delta t, & \xi \end{bmatrix} \tag{2.17}$$

In this parameter space, Δt and β are determined based on common DEM computation practice. We also know the contact stiffness between the 3D-printed particles from the measured Young's modulus and Poisson's ratio (see the experiment section). For the associated friction coefficient, we consult [53] where a similar rubber-like material is used for particle fabrication, and a value of 0.6 is used. We adjust 0.6 to 0.5 such that the stress component $\sigma_{y,\theta}$ under uniaxial compression before shear is applied ($\theta = 0$), matches the applied compression force F_N on the confining bar (properly scaled by the cross section of the confining bar). Here $\sigma_{y,\theta}$ is computed from the Christofferson equation using the inter-particle forces inferred by GEM. With these four parameters being constrained, the actual parameter space reduce to just ξ.

We note here that, since the PTFE particles are not considered for forces computation in the experiments, the associated friction coefficient and elastic properties are not measured. We set the friction coefficient between PTFE cylinders and that between PTFE cylinder and aluminum boundary bar both to be 0.1, elastic modulus to be 0.5 GPa and Poisson's ratio to be 0.46 based on [42]. As the 3D-printed particles has much rougher surface than those of the PTFE particles, we set the associated friction coefficient between them to be 0.5 as well. Table 2.2 and 2.3 show values of relevant parameters used in our simulation, where ξ_1 and ξ_2 are the damping parameters determined for cylindrical particle case and arbitrarily shaped particle case respectively. Again, we note that all modeling parameters except ξ are kept as the same for both cases and are consistent with our experimental measurements. While the damping parameter ξ can not be measured experimentally, the determined ξ_1 and ξ_2 are consistent with those estimated from a structural dynamics perspective [31]: for each particle in the system, we may simplify its interaction with all

Material properties	Boundary(Aluminum)	PTFE cylinders	3D-printed particles
Young's modulus E (GPa)	72	0.5	0.0635
Poisson's ratio ν	0.33	0.46	0.5
Density ρ (kg/m^3)	2700	1471	961

Table 2.2: Experimentally measured material properties.

Parameters	Value
L (m)	0.02
μ_s (between boundary and PTFE cylinder)	0.1
μ_s (between PTFE cylinders)	0.1
μ_s (between PTFE cylinder and 3D-printed particle)	0.5
μ_s (between 3D-printed particles)	0.5
Δt (s)	10^{-5}
β	0.9
ξ_1 (s^{-1}) [calibrated]	1.7×10^4
ξ_2 (s^{-1}) [calibrated]	1.1×10^4

Table 2.3: Other model input parameters.

other surrounding particles effectively as a linear spring-dashpot system (LSD) with corresponding stiffness $k_{eff} \sim k_n$ and damping $\xi_{eff} \sim \sqrt{k_{eff}/m}$, where k_n and m are the contact stiffness and mass of the considered particle. Since most particles in experiments are 3D printed, we estimate k_{eff} by considering the elastic property (shown in Table 2.2) of such materials, and compute the average mass of all 3D-printed particles, which together for both cases gives $\xi \sim 10^4$ − in close proximity to the determined ξ_1 and ξ_2. We further note that due to the fact that the particle mass distribution of each experiment case is different, we expect slight discrepancies between ξ_1 and ξ_2.

Comparison between LS-DEM simulation and experimental results

In this section we show the comparison between the LS-DEM simulation and experiment results on both the macro-scale and the inter-particle force level scale.

Macro-scale mechanical response

LS-DEM has already been shown to be able to capture the macro-scale deformation and shear-banding of real sand subjected to triaxial loading [63]. Therefore, our study serves as another evaluation of the ability of LS-DEM of capturing the macro-scale response with additional results on the grain scale. As mentioned before, on the macro-scale we compare two quantities: the vertical dilation ratio $\epsilon_\theta = \frac{h_\theta - h_0}{h_0} \times 100\%$

and the average stress $\boldsymbol{\sigma}_\theta$ at a given shear angle θ computed according to Eqn. 2.7. Figures 2.7 and 2.8 show the comparisons for ϵ_θ and the three stress components of $\boldsymbol{\sigma}_\theta$: $\sigma_{x,\theta}, \sigma_{y,\theta}$ and τ_θ for both experimental cases. Our model correctly captures not only the evolution of all three stress components with increasing θ but also the vertical dilation ratio evolution, see Figures 2.7 and 2.8. For the arbitrarily shaped particle experiment, for ϵ_θ we notice that although our model shows an earlier dilation than that from experiment, it is able to capture the overall trend and both the maximum compaction and the maximum dilation ratio at the right amount and under the right shear angle θ (Figure 2.8). Our results demonstrate that by using a suitable contact model, LS-DEM is able to quantitatively capture the macro-scale response of granular material with all model parameters (except the global damping ξ) being directly determined experimentally without any calibration.

Particle-scale force response

In this section, we go one scale downward and for the first time make comparison between experiment and simulation at the inter-particle force level. We note that, the simulations use the same physical parameters (μ_s, ν, E and ρ, see Table. 2 and 3) as in the experiments. In our particular cases, we are unable to make one-to-one comparisons of kinematics and even worse kinetics at the particle level, as the particle systems are chaotic – small perturbations can create large differences. Additionally, a given contact point is sporadic and cannot be traced in time. As such, in terms of the inter-particle forces, we present qualitative and statistical comparisons. First, in terms of qualitative comparisons, Fig.2.9 show the spatial distribution of inter-particle forces for both cases in experiments and simulations at four different shear angles $\theta = 0.2°, 4.4°, 8.0°$and $13.9°$. It can be observed that even though the exact spatial locations of large force chains are not the same between experiments and simulations, our simulations can capture the overall evolution of force network qualitatively. One step further, in terms of statistical comparisons, we compare inter-particle forces in terms of their distribution; specifically, the polar diagram of contact force magnitude $|\boldsymbol{f}^c|$, the polar diagram of friction mobilization $\eta = \frac{|\boldsymbol{f}_t^c|}{|\boldsymbol{f}_n^c|}$, and the polar histogram of contact orientation defined as the direction of $\boldsymbol{f}_n^c$ ($\boldsymbol{f}_n^c$ is defined as the normal component of $\boldsymbol{f}^c$). Figures 2.10 (for cylindrical particle case) and 2.11 (for arbitrarily shaped particle case) show the results of $|\boldsymbol{f}^c|$, η and contact orientation from simulation and experiment at the same four shear angles. For all three quantities, simulations show both qualitative and quantitative agreement with experiments. In particular, in terms of the polar diagram of contact

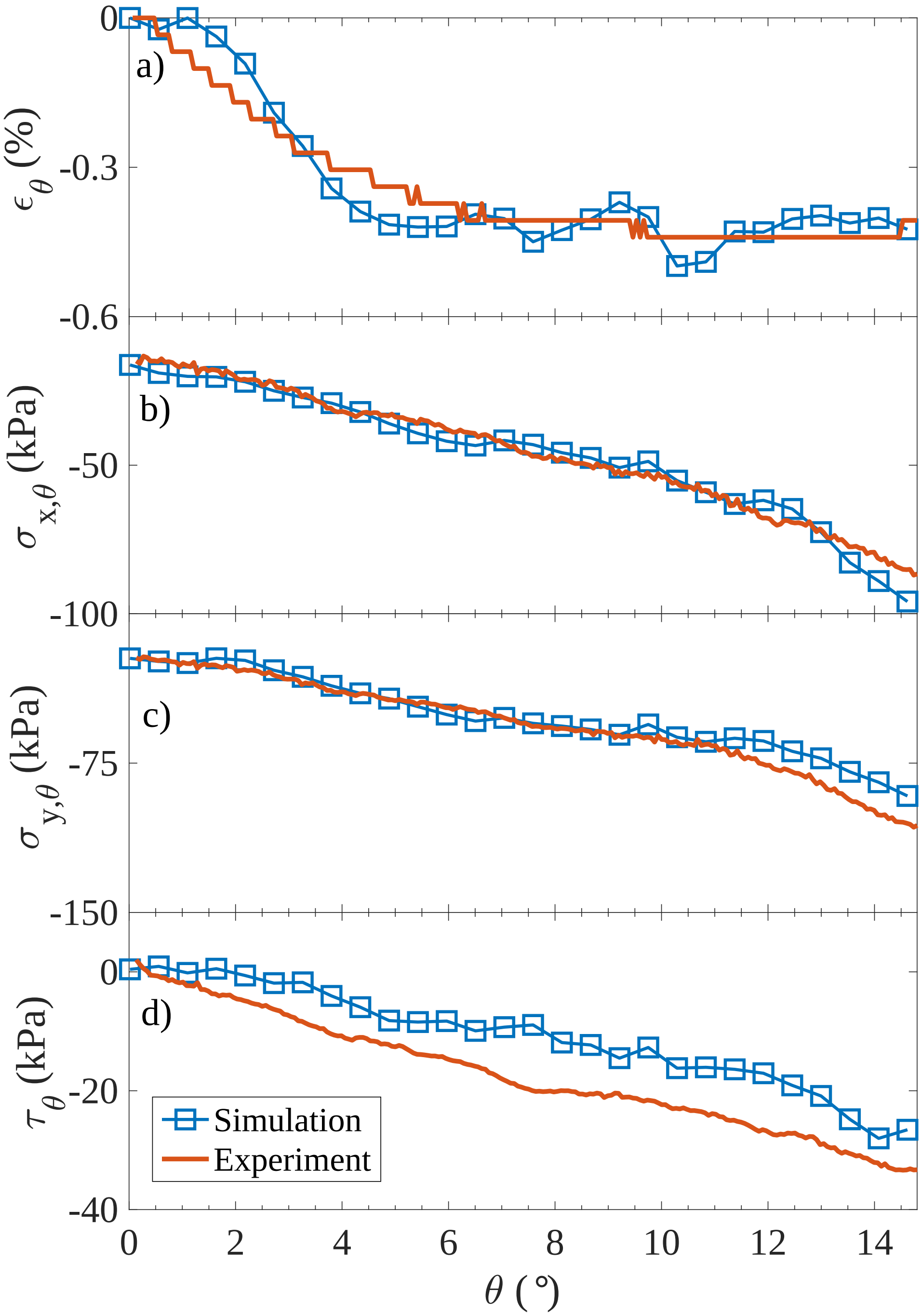

Figure 2.7: Vertical dilation ϵ_θ and stress $\boldsymbol{\sigma}_\theta$ response as the shear angle θ increases computed from experiment and simulation for the cylindrical particle case.

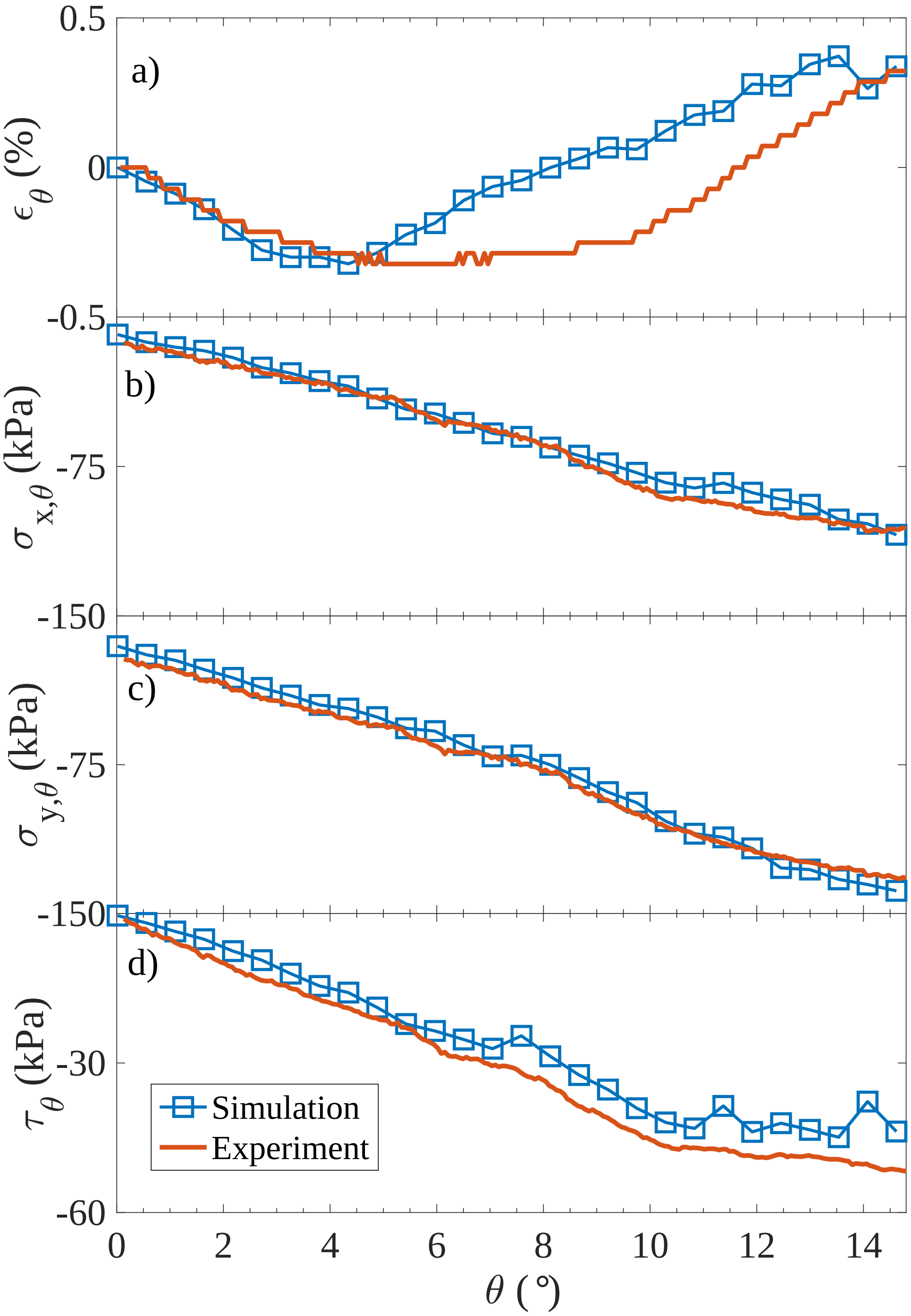

Figure 2.8: Vertical dilation ϵ_θ and stress $\boldsymbol{\sigma}_\theta$ response as the shear angle θ increases computed from experiment and simulation for the arbitrarily shaped particle case.

force and polar histogram of contact normal, our model successfully captures: (i) their rotation as the shear angle θ increases, and (ii) larger contact forces are less mobilized than smaller ones (Figure 2.10(e)(h)(k), Figure 2.11(e)(h)(k)). We observe that, especially for the case of cylindrical particles, however, simulations slightly underestimate the magnitude of friction mobilization η. A possible reason could be that due to manufacturing errors, the 3D printed spherical particles may show slight deviation from perfect disks which are however implemented in our simulation. This explanation is consistent with the result that the arbitrarily shaped particle case shows higher friction mobilization than the spherical shaped particle case.

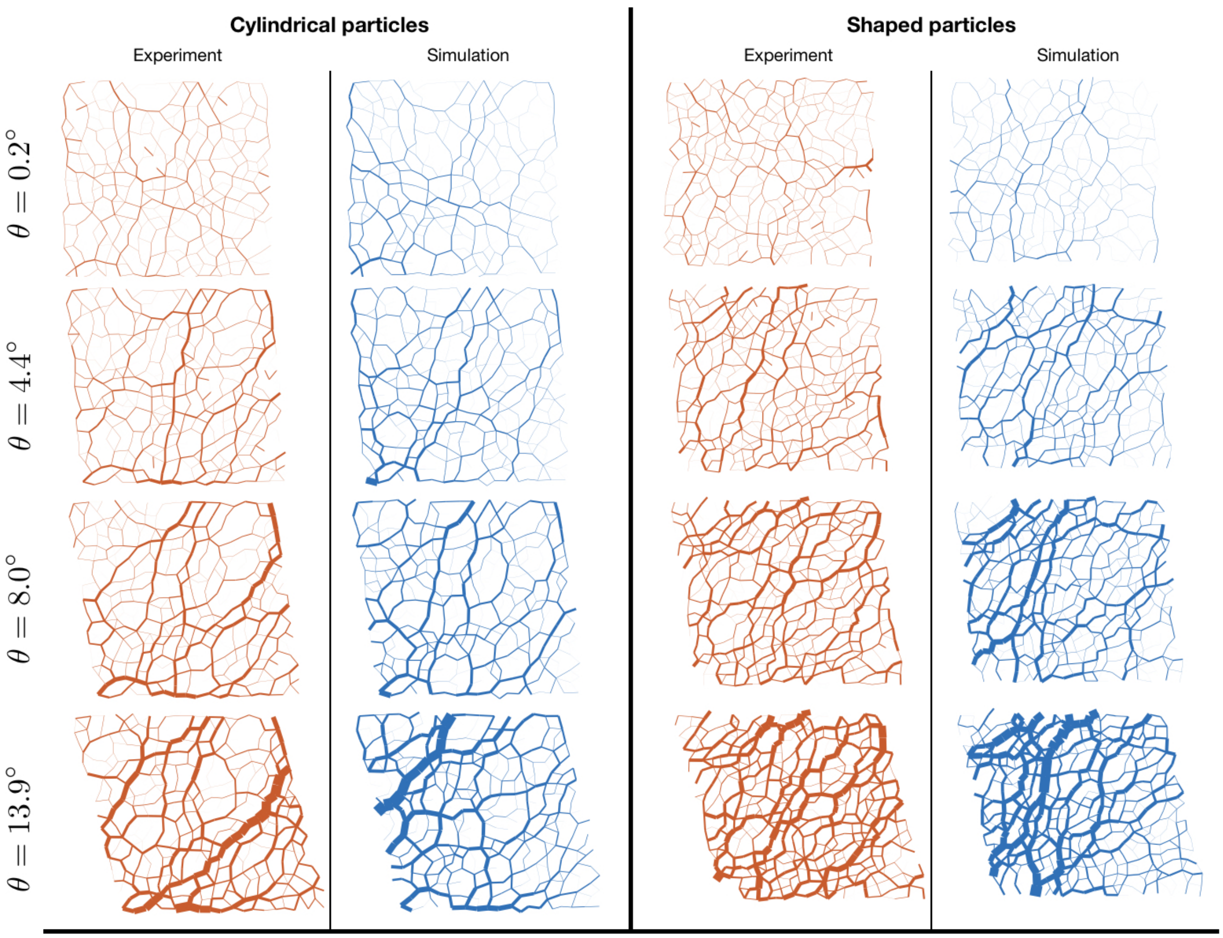

Figure 2.9: The spatial distribution of inter-particle forces measured from experiments (red) and computed from simulations (blue) for both cases. All forces are shown under then same scale for a clear comparison.

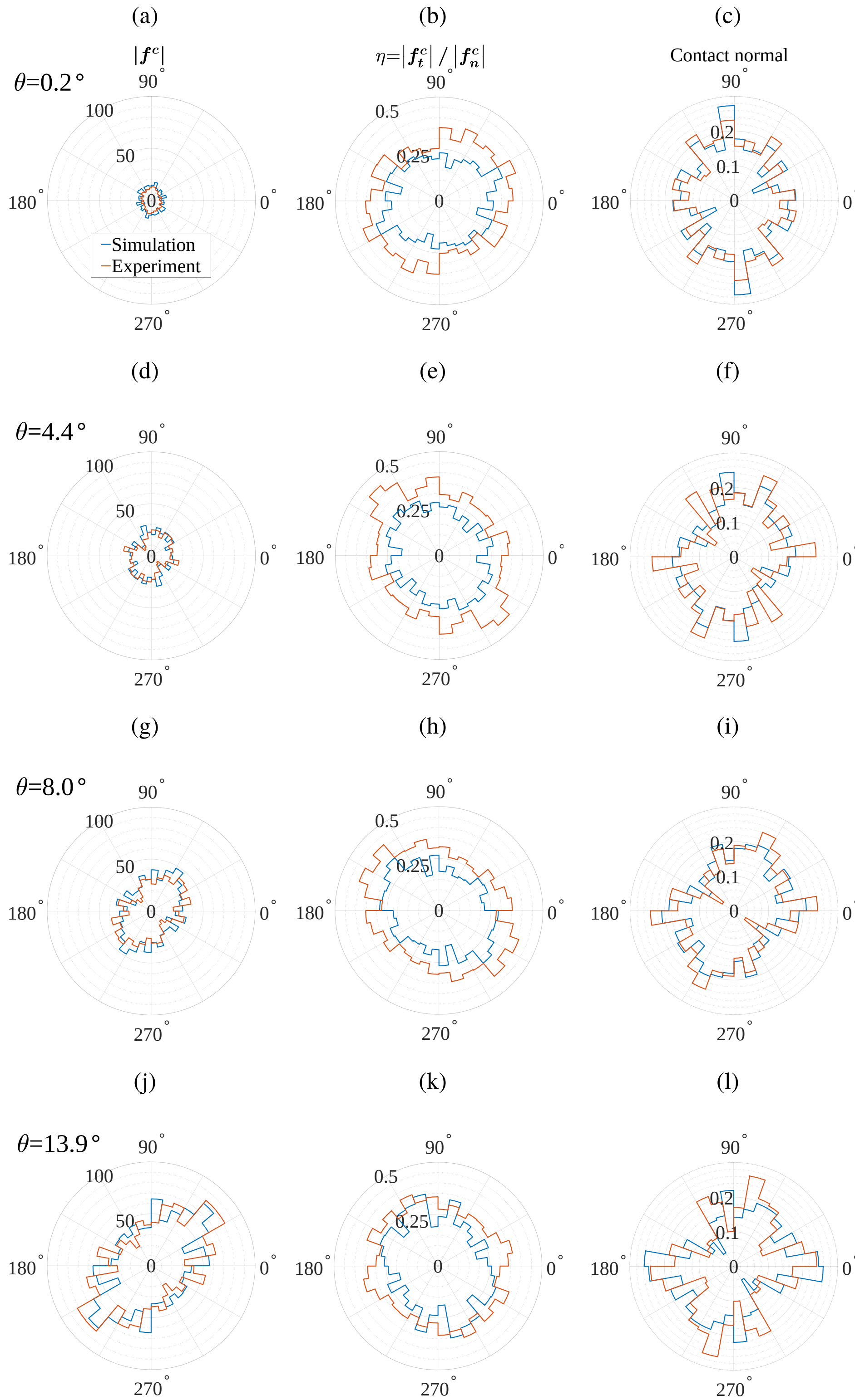

Figure 2.10: Particle scale response represented by the polar diagram of contact force magnitude $\boldsymbol{f}^c$, the polar diagram of friction mobilization $\eta = \left|\frac{\boldsymbol{f}_t^c}{\boldsymbol{f}_n^c}\right|$, and the polar histogram of contact normal at four different shear angle: $\theta = 0.2°$ (a)-(c), $\theta = 4.4°$ (d)-(f), $\theta = 8.0°$ (g)-(i), and $\theta = 13.9°$ (j)-(l) from experiment and simulation for cylindrical particle case.

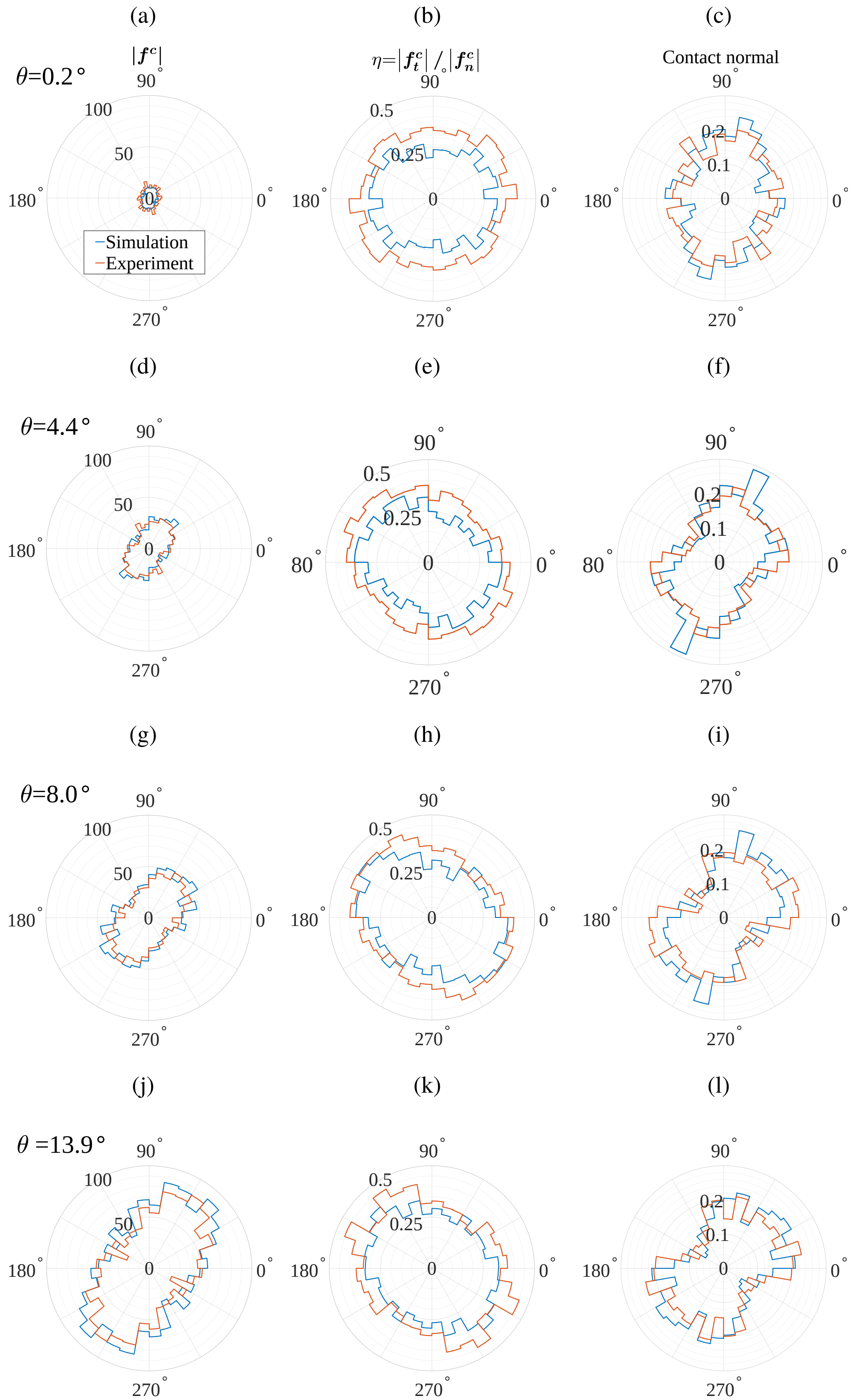

Figure 2.11: Particle scale response represented by the polar diagram of contact force magnitude f^c, the polar diagram of friction mobilization $\eta = \left|\frac{f_t^c}{f_n^c}\right|$, and the polar histogram of contact normal at four different shear angle: $\theta = 0.2°$ (a)-(c), $\theta = 4.4°$ (d)-(f),$\theta = 8.0°$ (g)-(i), and $\theta = 13.9°$ (j)-(l) from experiment and simulation for arbitrarily-shaped particle case.

2.4 Conclusions and future outlook

This study for the first time presents systematic analysis that evaluates the ability of LS-DEM on predicting particle scale response of granular material beyond the macro-scale, and beyond simple particle shape. Our contribution can be summarized as follows:

- We show that by using the suitable contact model, LS-DEM is able to capture quantitatively the macro-scale mechanical response of granular material measured from experiments, with all model parameters being physically well-defined and directly measured from experiments (except damping).
- We for the first time perform systematic comparison between simulation and experiment results at the particle scale. We show that LS-DEM simulations, with all model parameters being consistent with experimental measurements, can quantitatively predict the inter-particle force distribution among particles with various shape.

Our study also opens the door for several valuable future investigations. For instance, is it possible to directly determine the global damping ξ from experimental measurements? In our current implementation ξ is computed based on the average mass of the system and is held constant for each particle – this turns out to be a rather good approximation for our case since all particles have similar mass; however, this may be problematic for system with high poly-dispersity. It may be beneficial to consider particle scale damping that is commonly used for highly dynamical situations such as granular flow [34, 108], where the particle scale damping between two particles in contact is determined by the mass of the two particles, the coefficient of restitution e and the contact stiffness k_n. Investigations along this direction remains a topic for the future.

To conclude, by systematically comparing experiment and numerical simulation results at both macro and particle scales, we show the versatility and potential of LS-DEM in studying the physics and mechanics of granular materials. We also present several valuable future investigations on LS-DEM with the goal of multi-scale predictability. Along this direction, LS-DEM opens an avenue to efficiently study the inter-play between particle shape and inter-particle force distribution which remains vital in understanding not only many natural phenomena such as booming sand dunes [51], but also engineering granular particles for novel properties [82].

Chapter 3

IDENTIFYING SPATIAL TRANSITIONS IN HETEROGENEOUS GRANULAR FLOW

Liuchi Li and José E. Andrade (2020). "Identifying spatial transitions in heterogeneous granular flow." In: *Granular Matter*. In press. ISSN: 1434-7636.

Abstract

It is well known that heterogeneous granular flows exhibit collisional, dense, and creep regimes that can coexist in space. How to correctly predict and control such complex phenomena has many implications in both mitigation of natural hazards and optimization of industrial processes. However, it still remains a challenge to establish a predictive granular rheology model due to the lack of understanding of the internal structure variation across different regimes and its interaction with the boundary. In this work, we use DEM simulations to investigate the internal structure of heterogeneous granular flow developed at the center of rotating drum systems. By systematically varying the side wall conditions, we are able to generate various heterogeneous flow fields under different levels of boundary effects. Our extensive simulation results reveal a highly relevant micro-structural quantity $\delta\theta = |\theta_c - \theta_f|$, where θ_c and θ_f are the preferred direction of inter-particle contacts and the preferred direction of inter-particle force transmissions, respectively. We show that $\delta\theta$ can characterize the internal structure of granular flow in collisional, dense, and creep regimes, and its variation can identify the transition between them. In particular, in dense and collisional regimes, the classical rheological relation between bulk friction μ and inertia number I holds, while in the creep regime, such relation breaks down and μ instead depends on $\delta\theta$. Our findings hold for all investigated flow fields regardless of the level of boundary effect imposed, and regardless of the amount of shear experienced. $\delta\theta$ thus provides a unified micro-structural characterization for heterogeneous granular flow in different regimes, and lays the foundation of establishing microstructure-informed granular rheology models.

3.1 Introduction

Granular materials, collections of solid frictional grains with size greater than one micrometer, are ubiquitous on earth. The existence of static friction, negligible thermal effect and inelastic particle collision lead to their distinct ability of behaving like solids, liquids or gases [56]. In particular, when behaving like liquids, it has been observed that, both experimentally and numerically in various geometries [16, 17, 28, 66, 81], they often depart from homogeneous flow and exhibit co-existing regimes [43] that range from collisional to dense to creep flow. How to model and further control such feature of co-existing regimes has been of major research interest over the past decades because it would benefit not only the mitigation of natural hazards such as snow avalanches, but the optimization of industrial processes such as silo discharge.

Based on the seminal $\mu(I)$ constitutive relation [34, 60, 78], and the observations of granular cluster formation [15, 17, 80, 86, 110], several models have been proposed that could capture experimental observations by incorporating the concept of spatial correlation (giving rise to the so-called "non-local" rheology models) [20, 61, 94]. Here $\mu = \tau/P$ is the bulk friction with τ the shear stress and P the pressure; $I = \dot{\gamma}\bar{d}\sqrt{\rho_s/P}$ is called the inertial number with $\dot{\gamma}$ the shear rate, $\bar{d}$ the (mean) particle diameter and ρ_s the material density (see [34, 60] for details). Despite these theoretical advances, however, non-local effects are furnished into the $\mu(I)$ rheology by invoking phenomenological arguments that are still under debate [21, 35, 106]. The challenge lies in resolving the following three issues. First, in order to be valid, these models require stationary flow to further become steady (large amount of shear deformation), excluding their applicability to geometries containing flowing layers that are only stationary [32], such as creep flow in a rotation drum [100], in a silo [28] or over a heap [39, 66]. Second, the effects of boundary conditions on non-local phenomena are poorly understood - non-local phenomena can happen either with or without the presence of boundaries. For example, in "Kolmogorov flow" non-local phenomena manifest with periodic boundary conditions [106], while in planar shear flow [79] without stress gradient, non-local phenomena [8] can be triggered by the presence of rigid side walls. Lastly, it still remains unclear when and where non-local phenomena become significant. Resolving these three issues requires a fundamental understanding of (1) the internal structure variation of granular flow in collisional, dense and creep regimes, and (2) the dependence of internal structure variation on the amount of shear experienced and on boundary conditions. Only with such an understanding can we move forward to investigate the physical mechanism of non-locality, and eventually establish granular rheology models with a unified underlying mechanism.

To achieve such an understanding on the internal structure variation and its dependence on the amount of shear experienced and on boundary conditions, one will need to carefully choose a geometry that satisfies the following three requirements: (1) it should develop flow residing in all three regimes allowing non-local phenomena to arise at certain locations, (2) in the creep regime, it should produce flow to be either just stationary or further steady, and (3) it should allow flexible control over boundary effects [59, 90]. In light of this, we choose to investigate 3D flow developed at the center of rotating drums with a large enough radius ($D/\bar{d} > 100$ [36]): we can produce spatially heterogeneous flow with stationary and steady creep flow layers coexisting in space, and further, we can adjust the levels of imposed boundary effects by systematically varying the drum configurations (drum width and side wall friction). In particular, heterogeneous flow free of boundary effect is achievable numerically by using periodic side walls. In this work, we for now focus our attention on nearly mono-disperse, (quasi)spherical and rigid particles. We first perform experimental measurements on the dynamics of glass beads flowing in a rotating drum, we then use these measurements to calibrate and validate our DEM model, and we lastly use this DEM model to probe various flow fields, by both changing the rotating speeds and the drum configurations. Despite having only studied one geometry, the obtained flow fields are general enough to be comparable to those produced under other geometries.

We propose a micro-structural quantity called $\delta\theta = |\theta_c - \theta_f|$, which we can define as the overall misalignment between the preferred direction of contacts (θ_c) and the main direction of inter-particle force transmissions (θ_f). We show that (1) $\delta\theta$ naturally identifies the spatial transition between collisional, dense, and creep regimes, and (2) μ depends on $\delta\theta$ instead of I in the creep regime where the one-to-one $\mu(I)$ relation breaks down. These findings hold regardless of the studied rotating speeds and drum configurations (with or without boundary effects), and hold in the creep regime regardless of the amount of shear experienced. Accordingly, our findings are not only applicable to similar geometries (such as heap flows [39, 66]) where shear deformation can be largely absent, but relevant to other geometries (such as planar flows with gravity [121]) where steady creep flow occurs and is believed to be triggered by steady state non-local effects. Our results suggest that the misalignment between θ_c and θ_f in the creep regime can be caused by either (1) steady-state non-local effects or (2) lack of shear deformation. Further investigations to distinguish or to find connections between the two will be helpful in establishing microstructure-informed granular rheology models.

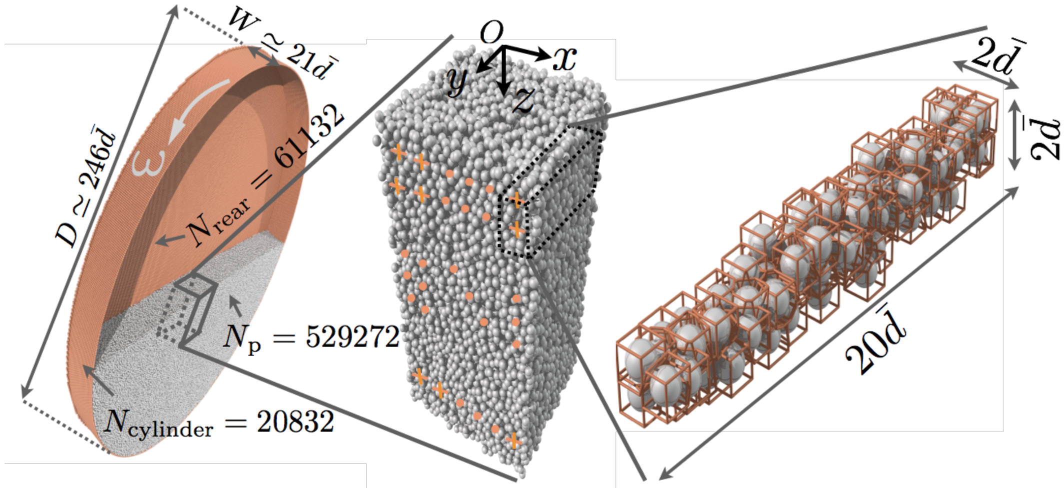

Figure 3.1: Simulation setup with the region of interest. From left to right: simulation setup in accordance with the drum used in the experiments (front plane not shown); region at the drum center for data extraction; (weakly) poly-disperse spheres with their computed radical Voronoi diagram that is used to compute the volume fraction ϕ.

3.2 Experiments

We half-fill a drum with quasi-spherical soda lime glass beads with density ρ_s = 2450 kg/m^3, roundness ≥ 95%, and particle diameter $d = 1 \sim 1.25$ mm. The drum has inner diameter $D = 277\,\mathrm{mm} \simeq 246\bar{d}$ and inner width $W_0 = 25\,\mathrm{mm} \simeq 22\bar{d}$, where $\bar{d} = 1.125$ mm. The front-side of the drum is bounded by a transparent circular glass plate allowing for optical measurement, while the rear-side and inner-cylinder walls have glass beads glued to them (accordingly the effective drum width is $W \simeq 21\bar{d}$). Different rotation speeds ω can be imposed in the experiments, ranging from 0.21°/s to 11.23°/s. In this work we consider three different rotation speeds: ω = 2.59°/s, 5.73°/s and 11.23°/s. For each considered rotation speed, after 20 rotations, we take images via a high-speed camera (Phantom V310, fps = 1000 with image size 288 px × 288 px) throughout a time window of 10 s, and measure the dynamical angle of repose and down-stream velocity near the glass plate at the center of the drum. For information on how these measurements are performed, see Appendix C. The measured dynamical angle of repose and down-stream velocity are used to calibrate and validate our numerical model.

3.3 Discrete-element-method (DEM) simulations

We use DEM [33] implemented in the open-source code LIGGGHTS [65] to perform simulations, approximating glass beads by spheres that interact through Hookean contact law with Coulomb friction. Initially we consider a drum to share the same dimensions as the one used in the experiments – the cylindrical wall and rear-side wall are made of spheres, and the front-side wall is treated as a flat plane, see Fig.3.1. Assuming the diameter following a Gaussian distribution $d \sim \mathcal{N}(1.125, 0.04^2)$, we sample spheres used as walls ($N_{\mathrm{rear}} = 61132, N_{\mathrm{cylinder}} = 20832$), and as granular medium ($N_{\mathrm{p}} = 529272$). We have also tried a uniform distribution from 1 mm to 1.25 mm, and we found that the results are insensitive to the chosen distribution regarding the particle diameter range considered in our study. The diameter range $d = 1 \sim 1.25$ mm is ensured by rejecting over and under-sized spheres. We calibrate and validate our model for flows developed at the drum center based on the aforementioned drum experiments (see Appendix A for details). The determined value for each model parameter is: the normal stiffness $k_{\mathrm{n}} = 2 \times 10^5 \bar{m}g/\bar{d}$ with $\bar{m}$ the mean particle mass and g the gravitational constant, the tangential stiffness $k_{\mathrm{t}} = 2/7k_{\mathrm{n}}$, the coefficient of restitution $e = 0.82$ [accordingly the normal damping $\gamma_{\mathrm{n}} = -2\ln e\sqrt{\bar{m}k_{\mathrm{n}}/(\pi^2 + \ln^2 e)}$], the tangential damping $\gamma_{\mathrm{t}} = 0$, and the surface friction coefficient $\mu_{\mathrm{p}} = 0.4$ with a rolling friction $\mu_{\mathrm{r}} = 0.03$. The friction coefficient between spheres and the front-side wall is also 0.4 with no rolling friction. The integration time step $\Delta t = t_c/10$ [18], where t_c is the binary collision time. Since the determined combination of values for these model parameters may not be unique depending on the specific calibration-validation procedure, we do not rule out the possible existence of other combinations.

Based on the validated model, we perform two additional simulations with $\omega = 33.69°/\mathrm{s}$ and $67.38°/\mathrm{s}$. Taking advantage of this novel asymmetrical side wall setup (one bumpy one flat) [4, 22, 60, 102], in order to include more flow conditions, we further consider different drum configurations by either varying its width or varying simultaneously the surface friction coefficient associated with the wall spheres and the front plane (hereafter we term both as the wall friction), with no change to the rolling friction. Specifically, we consider six different types of drum configurations: in four of them the wall friction is varied (first row in Table 3.1), while in the remaining two, the effective drum width is varied (second and third row in Table 3.1). For each drum configuration, we consider five different rotation speeds: $\omega = 2.59°/\mathrm{s}, 5.73°/\mathrm{s}, 11.23°/\mathrm{s}, 33.69°/\mathrm{s}$, and $67.38°/\mathrm{s}$. Accordingly, we consider in total 30 different flow fields which have Froude number on the order of $10^{-5} \sim 10^{-2}$. For these additionally performed simulations, even though we have not directly validated them against experiments, the simulated macro-scale flow responses are consistent with relevant studies. For instance, stronger side wall effect can lead to higher dynamical angle of repose [114, 115]. We use these simulation results to investigate both the macro-scale rheological responses and the micro-scale internal structure variations under different flow conditions.

W_0 (mm)	$W/\bar{d}$	Wall friction
25	21	0.2, 0.4, 0.6, 0.8
24	∞	— (periodic)
12	10	0.4

Table 3.1: Considered drum configurations in our simulations. For the periodic case, the cylindrical wall friction remains 0.4. Every configuration operates under five different rotation speeds $\omega = 2.59°/\mathrm{s}, 5.73°/\mathrm{s}, 11.23°/\mathrm{s}, 33.69°/\mathrm{s}$ and $67.38°/\mathrm{s}$.

For each simulation, after the flow becomes stationary, we output data for analysis. We choose the reference frame to be located at the drum center and to rotate with the drum, with the y (z) axis being parallel (perpendicular) to the local free surface (Fig.3.1). Note that while the local free surface remains flat, the whole surface profile can show an “S-shape" [115], see Appendix C. We consider flow at the drum center where the local surface remains flat for easy data extraction, and where the cylindrical wall effect is negligible [36] (we have $D/\bar{d} > 100$). In particular, as briefly mentioned in the introduction section, flow produced at the drum center can be essentially free of boundary effects once we set the side walls to be periodic. We first create a set of grid points (red crosses in Fig.3.1) at the drum center ($y = 0$) that are equally-spaced by $\bar{d}$ in both the x and z directions: along the x direction, they span from $x = -8\bar{d}$ to $x = 9\bar{d}$ ($W/\bar{d} \simeq 21$) and from $x = -3\bar{d}$ to $x = 4\bar{d}$ ($W/\bar{d} \simeq 10$); along the z direction they cover a depth down to $100\bar{d}$. We then consider a box ($L_y = 20\bar{d}, L_x = L_z = 2\bar{d}$) centered at $y = 0$, aligned with the y direction, surrounding each grid point to extract data. Some relevant fields are (i) the velocity v_i, (ii) the shear rate $\dot{\gamma}_{ij} = (v_{i,j} + v_{j,i})/2$ (neglecting $\partial_y v_i$), together with the deviatoric part $\dot{\gamma}^d_{ij} = \dot{\gamma}_{ij} - \dot{\gamma}_{kk}\delta_{ij}/3$ and $|\dot{\gamma}^d| = \sqrt{2\dot{\gamma}^d_{ij}\dot{\gamma}^d_{ij}}$, (iii) the Cauchy stress $\sigma_{ij} = \sum_c f^c_i \ell^c_j/V$ [29] together with $P = -\sigma_{kk}/3, s_{ij} = \sigma_{ij} + P\delta_{ij}$ and $\tau = \sqrt{s_{ij}s_{ij}/2}$, where V is the volume of every box and the summation is taken over all the contacts c with contact force f^c and branch vector ℓ^c connecting the centroids of contacting particles, and (iv) the volume fraction ϕ by computing the radical Voronoi diagram using the open-source code Voro++[105]. We confirm that (1) these quantities are insensitive to grid translation (either $y = -5d$ or $y = 5d$), box size ($L_x = L_z = \bar{d}$ or $3\bar{d}$) and grid spacing (50% or no overlap between boxes),

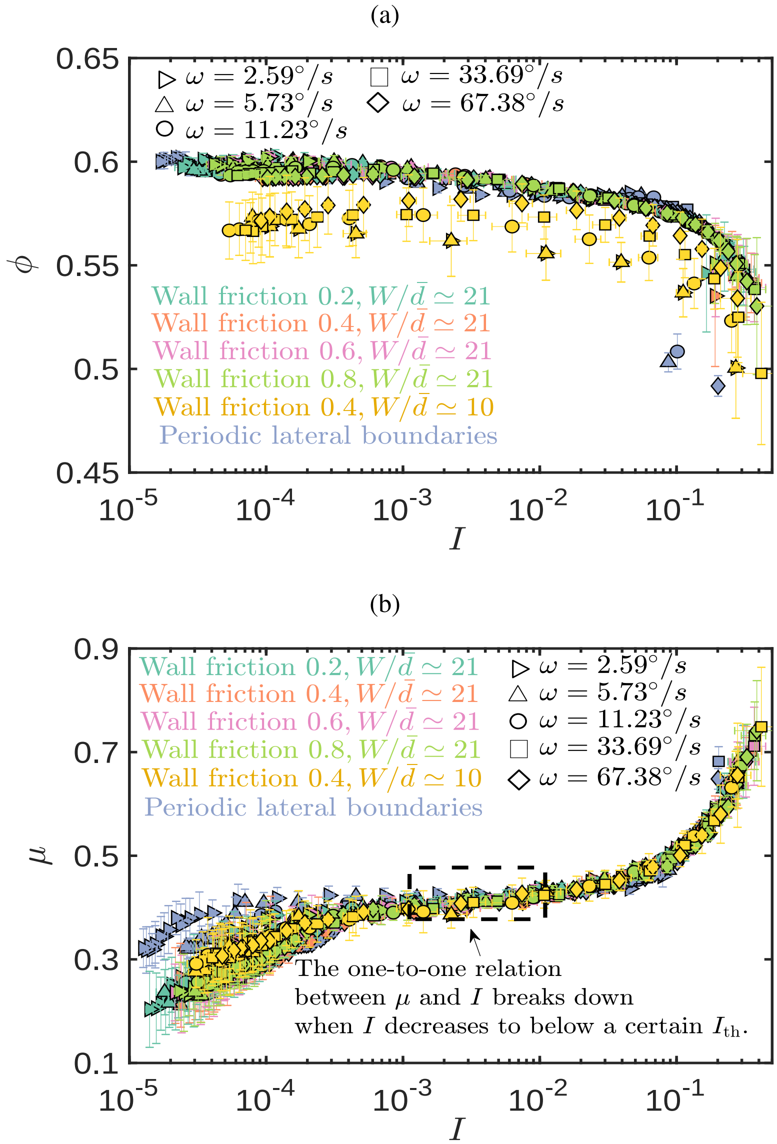

Figure 3.2: Macro-scale rheological responses. (a) Effective friction μ and (b) volume fraction ϕ as a function of I.

(2) kinematical contribution to the stress tensor is negligible [8, 34, 100, 121] and (3) results computed using either $\dot{\gamma}$ or $\dot{\gamma}^d$ are essentially identical and we use $\dot{\gamma}^d$ throughout. Note that the values of all fields mentioned hereafter are the temporal average of instantaneous ones computed via spatial coarse-graining within each box. Lastly, hereafter in all figures, quantities are shown as drum-width-averaged values, with error bars representing the variation across drum width.

3.4 Simulation results and discussions

Rheological response

We first perform macroscopic observations following the $\mu(I)$ rheology [34, 60]: Figs.3.2(a) and 3.2(b) show, respectively, the $\phi - I$ and $\mu - I$ relationships. The one-to-one relation between ϕ and I holds reasonably well, except for cases with $W/\bar{d} \simeq 10$, which can be attributed to stronger wall friction effects [25]. For all cases considered, the slow decrease of ϕ as I increases suggests the weak compressibility of steady dense granular flows [60, 67]. In contrast, a one-to-one relation between μ and I holds globally, until I decreases to a certain I_{th} threshold. For locations with $I \leq I_{\mathrm{th}}$, this one-to-one relation no longer holds globally but rather depends on both drum configuration and rotation speed. The threshold value of I_{th} varies on a case by case basis, but roughly resides in the range of $10^{-3} \sim 10^{-2}$, as shown in Fig.3.2(b). As we shall see later, as long as $I > I_{\mathrm{th}}$, all $\mu - I$ data can actually be described by the $\mu - I$ frictional law [34, 60]. Additionally, we find that more frictional walls and narrower drums, tend to break the typically-observed co-directionality between s and $\dot{\gamma}^d$ (see Appendix C). Hence, the rheological effect of side wall friction can be summarized as (1) when $I > I_{\mathrm{th}}$, it leads to the break down of the co-directionality between s and $\dot{\gamma}^d$ (this could explain the deviation of predicted velocity from experimental measurements reported in [60]), and (2) when $I \leq I_{\mathrm{th}}$, it not only intensifies the lack of co-directionality effect, but also signifies the departure from the one-to-one $\mu - I$ relationship. We have tried to explain the aforementioned observations using several existing non-local models [20, 45, 121], but unfortunately have not had much success (see Appendix C). Clearly, these observations necessitate a deeper fundamental understanding of the spatial transition marked by I_{th}.

Microstructures and spatial transitions

Based on our observations of the rheological response, we perform particle-scale investigations to characterize the micro-structure of the flow. In principle, we are trying to find certain micro-structural quantities whose variations against I (1) exhibit a clear transition as crossing I_{th} and identify the location z_{th} corresponding to I_{th}, and (2) correlate with the macro-scale rheological response: when $I > I_{\mathrm{th}}$ the spatial variations are free of drum configuration effects and rotation speed effects, while as soon as $I \leq I_{\mathrm{th}}$ they become both drum-configuration-dependent and rotation-speed-dependent.

We propose a micro-structural quantity $\delta\theta = |\theta_c - \theta_f|$ (see Appendix C.4 for additional results), where θ_c and θ_f are, respectively, the major principle direction of the “fabric" tensor (χ^c) and that of the “force-transmission" tensor (χ^f):

$$\chi^c_{ij} = \langle n^c_i n^c_j \rangle, \quad \chi^f_{ij} = \frac{1}{\langle |f| \rangle} \langle |f| n^c_i n^c_j \rangle, \tag{3.1}$$

where “$\langle \cdot \rangle$" denotes the average over all contacts, n^c is the contact normal which coincides with the branch vector direction for contact between spheres, $|f| = \sqrt{f_n^2 + f_t^2}$ is the associated contact force magnitude with f_n the normal component and f_t the tangential (frictional) component. Compared to χ^c, χ^f is a biased average in the sense that each contact is weighted by the magnitude of the force it carries. Mathematically, $\delta\theta$ has range $[0, 90°]$. Physically, for dense particle packings, θ_c and θ_f reflect, respectively, the geometrical configuration of the packing and the direction of force chains. For every simulation, we find that the variation of $\delta\theta$ as a function of depth follows the same trend that can be described with four different layers - Fig.3.3 showcases the variation of $\delta\theta$ against normalized depth with $\omega = 33.69°/\mathrm{s}$ under respectively, $W/\bar{d} = \infty$ with periodic side wall condition (lower panel of Fig.3.3(a)), and $W/\bar{d} \simeq 21$ with wall friction 0.4 (lower panel of Fig.3.3(b)): the first layer, from near the free surface until a critical depth z_1, shows a decrease in $\delta\theta$. Next, a second layer that goes until a critical depth z_2 and where $\delta\theta$ remains *constant*. This is followed by a third layer extending to a critical depth z_3 where $\delta\theta$ increases, and finally a fourth layer where $\delta\theta$ slowly relaxes. As we shall show later, this spatial variation of $\delta\theta$ can be used to identify different flow regimes. For depths $z > z_3$, where $\delta\theta$ ceases to increase but instead slowly relaxes along depth, we find that the particle motions are highly intermittent and therefore can not be considered as stationary. We regard these regions as “static” and do not attempt to model them, considering particle motions on the basis of the random void creation process [66].

Although the values of z_1 and z_2 differ from case to case, we find that z_1 corresponds to the universal $I \simeq 0.1$ (Fig.3.4(a)); z_2 coincides with z_{th} (Fig.3.4(b)), and $\delta\theta \simeq 10°$ for $z_1 \le z \le z_2$ (Figs.3.4(a) and 3.4(b)), where z_{th} is defined as the end point of the widely-observed exponential velocity profile [16, 100]. (See the upper panel of both Figs.3.3(a) and (b) where the black solid lines indicate exponential fit; also see Appendix B.5 for why drum-width-averaged profiles suffice to determine z_{th}.)

We first consider the regime where $z \le z_2$. The identified universal value $I \simeq 0.1$ [8] at $z = z_1$ is critical since it signifies the transition from collisional flow ($z \le z_1$), where particles interact majorly through short-lived binary collisions, to dense flow ($z_1 < z \le z_2$), where particles interact mostly through percolating contact network. Specifically, we observe that in the dense flow region, $\delta\theta$ remains constant and

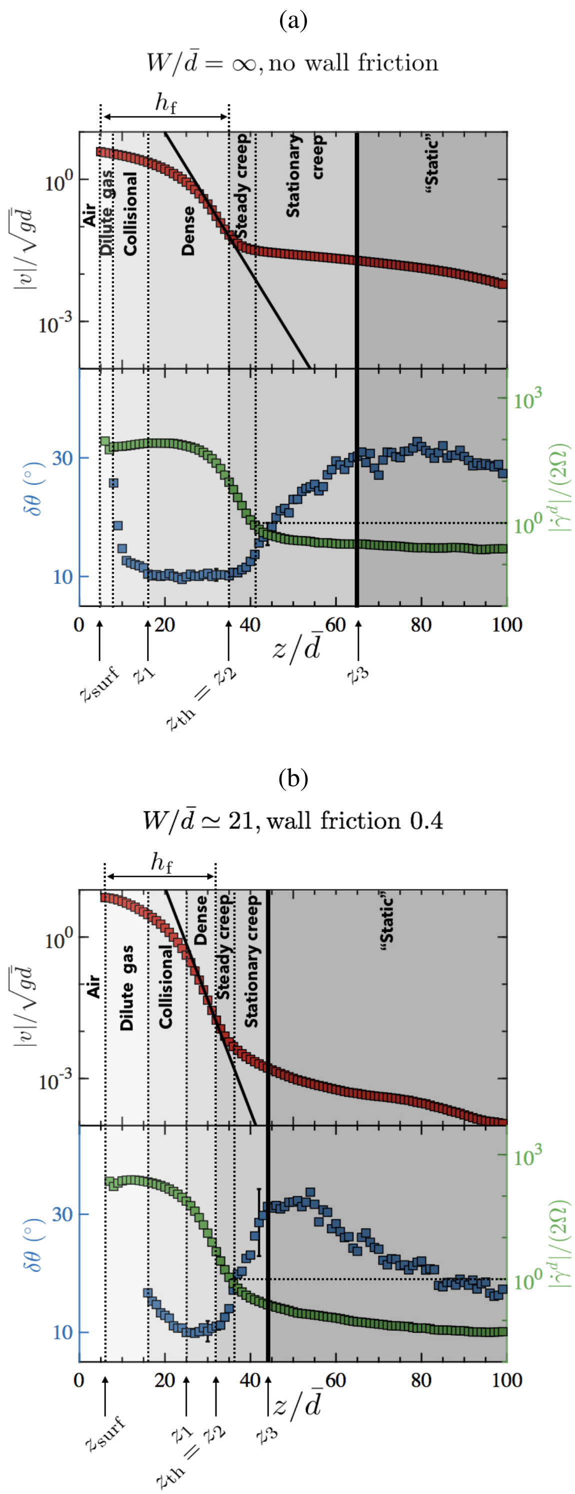

Figure 3.3: The spatial variation of velocity, $\delta\theta$ and $|\dot{\gamma}^d|/2\Omega$. (a) Under $W/\bar{d} = \infty$ with periodic side wall condition, the spatial variation of $|v|/\sqrt{g\bar{d}}$ (data in red at upper panel, with black solid lines indicating the exponential fit), of $\delta\theta$ (data in blue at lower panel, with error bars indicating its typical variation across drum width in both dense and creep regime), and of $|\dot{\gamma}^d|/2\Omega$ (data in green at lower panel) against normalized depth $z/\bar{d}$. (b) Same plots but under $W/\bar{d} \simeq 21$ with wall friction 0.4. We define a flow thickness (h_f) starting from the free surface (z_{surf}) to the end point of dense regime (z_2).

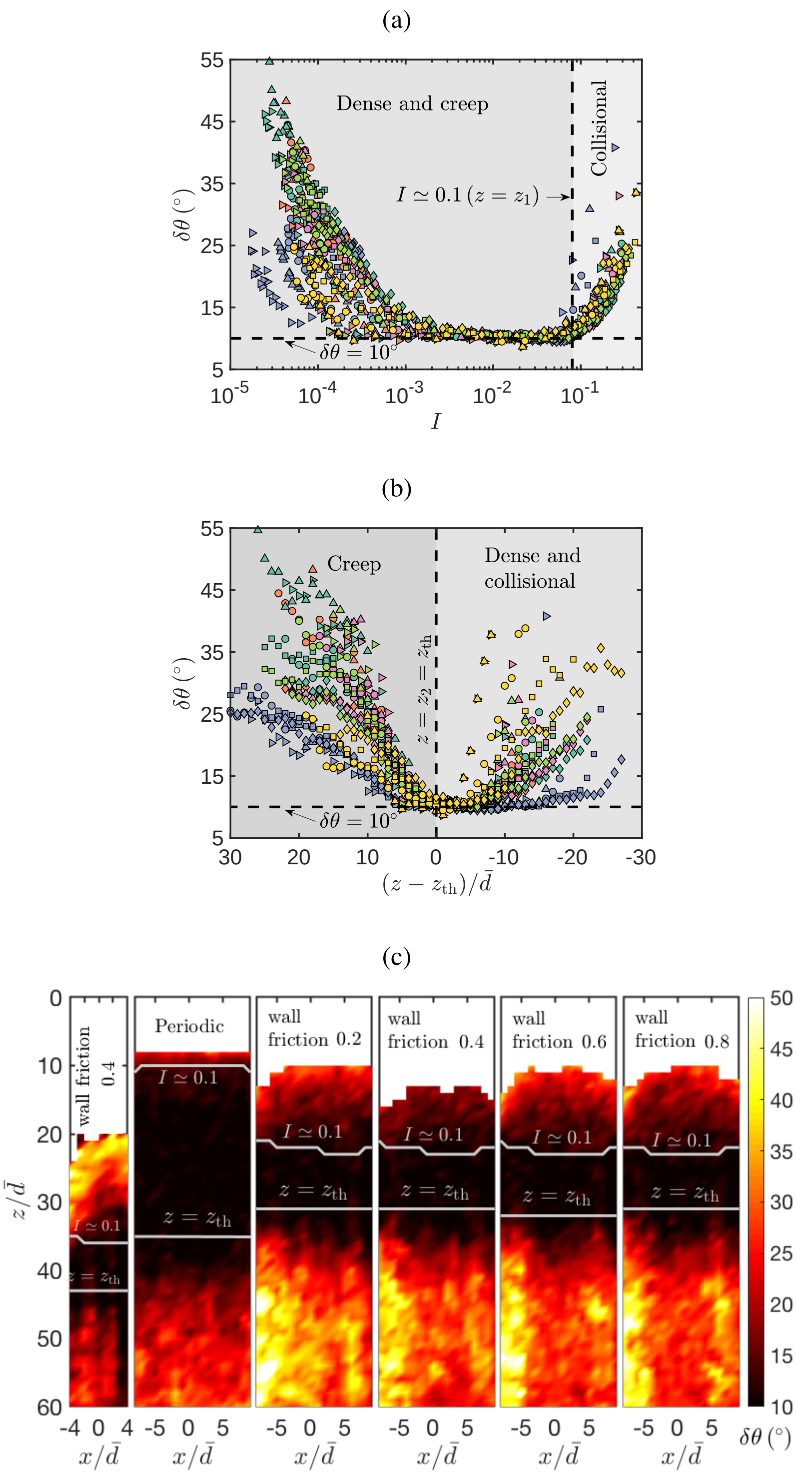

Figure 3.4: The variations of $\delta\theta$ for all cases considered. (a) Variation of $\delta\theta$ against inertia number I for all cases from $z \leq z_3$. (b) Variation of $\delta\theta$ against depth z (normalized by z_{th} and $\bar{d}$) from $z \leq z_3$. (c) Spatial variation (along both x and z) of $\delta\theta$ for all cases under $\omega = 33.69°/\mathrm{s}$; from left to right: frictional side walls ($W/\bar{d} \simeq 10$) with wall friction of 0.4, periodic side walls, and frictional side walls ($W/\bar{d} \simeq 21$) with wall friction of respectively 0.2, 0.4, 0.6, and 0.8.

small everywhere (Fig.3.4(c)), even near the side walls regardless of how frictional they are, or whether they are bumpy or flat and how wide the drum is. In fact, the observed θ_c and θ_f being nearly co-directional has also previously been reported in numerical studies of dense homogeneous planar flows [8]. Lastly, in this regime the $\mu(I)$ rheology in its invariant form holds (Fig.3.5(a)): we can fit the $\mu - I$ relation by both the linear [11, 34] and the non-linear formulation [60], although some deviation is observed for the latter for $I > 0.1$. On a side note, in all our simulations, within the collisional layer the highest inertia number value we are able to compute is around 0.3, beyond which, given the size of our homogenization box and our sampling frequency, the temporal average can not be properly defined since particle interactions are largely absent in multiple snapshots. We thus define the additional layer on top of the collisional layer as belonging to the dilute gas regime (upper panel of Figs.3.3(a) and (b)). We note that this value 0.3 has previously been identified as the point to transit into “fully collisional regime", where it has been shown that, the portion of floating particle (particle with no contact) in the system, goes beyond 0.6 [8]. In our study, we have consistent observation - looking at Fig. A6(a), the mean coordination number drops to nearly zero as approaching the dilute gas regime. Thus in the dilute gas regime (“fully collisional regime"), the $\mu(I)$ rheological law no longer holds, and kinetic theory [46] becomes applicable.

We then consider the regime where $z_2 < z \leq z_3$. As soon as z goes beyond z_2, $\delta\theta$ starts increasing and the $\mu - I$ relationship breaks down – it turns out that I_{th} corresponds to the location $z = z_2 = z_{\text{th}}$, where the misalignment between χ^c and χ^f begins, right at the end point of the exponential velocity profile. Thus, we identify this as the creep flow regime where μ has a one-to-one relation with $\delta\theta$ instead of I (Fig.3.5(a)): μ is inversely proportional to $\delta\theta$. From a micro-structural perspective, and for weakly poly-disperse sphere packings, μ can be well-approximated by adding together the contact anisotropy (determined from the eigenvalues of χ^c) and the force anisotropy (determined from the eigenvalues of χ^f) [8, 13]. Meanwhile, for a given packing configuration, with known contact anisotropy of direction θ_c, the force anisotropy is maximized if θ_f equals θ_c [103]: the larger the deviation of θ_f from θ_c, the smaller the force anisotropy and accordingly the smaller the μ.

More importantly, we emphasize here that the dependence of μ on $\delta\theta$, and the increase of $\delta\theta$ in the creep regime hold regardless of the amount of shear experienced. In order to see this, we use the local deformation $|\dot{\gamma}^d|/2\Omega$ to determine whether the initial memory is gone (shear deformation is large enough). Similar to [32], as the

(a)

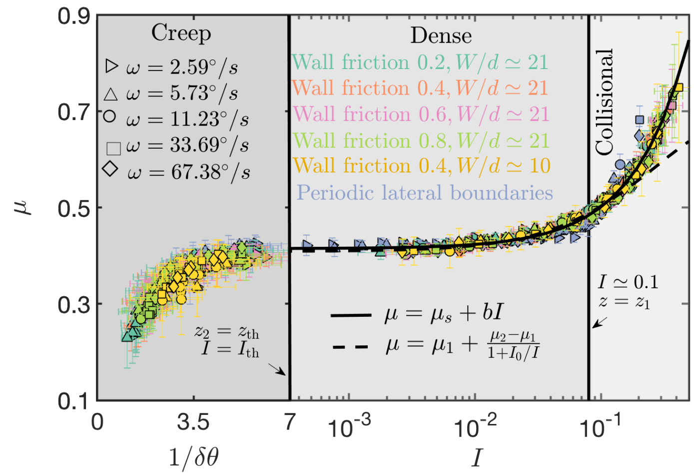

(b)

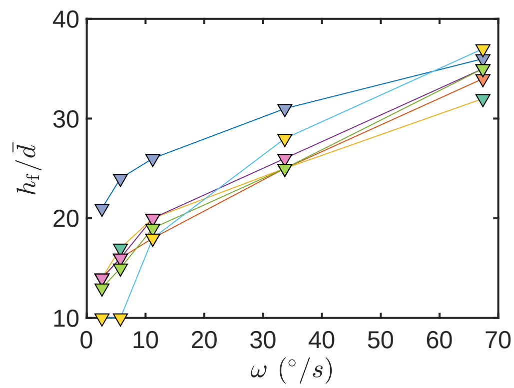

(c)

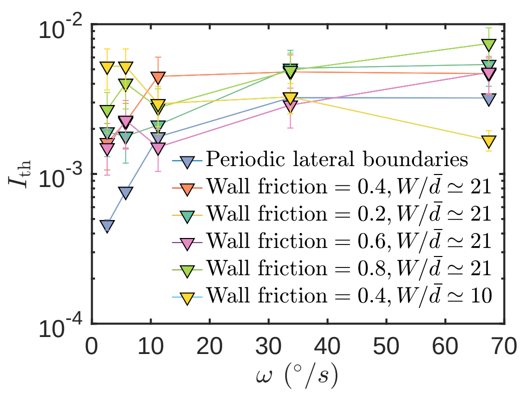

Figure 3.5: The relation between μ, I and $\delta\theta$ and the variation of h_f and $I_{\rm th}$ against rotation speed. (a) One-to-one relation between μ and I in collisional and dense regime, and that between μ and $\delta\theta$ in the creep regime. The $\mu - I$ data can be fit by both the linear law (black solid line) $\mu = \mu_s + bI$ with $\mu_s = 0.4148 \pm 0.0017$ and $b = 0.8628 \pm 0.0216$, and the non-linear law (black dashed line) $\mu = \mu_1 + (\mu_2 - \mu_1)/(1 + I_0/I)$ with $I_0 = 0.279$ (adapted from [60]), where $\mu_1 = 0.4089 \pm 0.0023$ and $\mu_2 = 0.7643 \pm 0.0107$. Variation against rotation speed of (b) flow thickness $h_{\rm f}$ and (c) $I_{\rm th}$ at $z = z_{\rm th}$.

drum is half filled and the flow is stationary, we consider the shear deformation to be sufficient if $|\dot{\gamma}^d|/2\Omega > 1$, in other words, particles have entered the surface avalanche after half a drum rotation period and the initial packing memory is erased by the fast surface flow. We have observed that for all rotation speeds considered, in the creep regime, the presence of layers with local deformation being both greater than one (termed as steady creep flow layer) and less than one (termed as stationary creep flow layer). As an example, as showcased in Figs.3.3(a)(b), under $\omega = 33.69°/\mathrm{s}$ for two different drum configurations ($W/\bar{d} \simeq 21$ with wall friction 0.4 and $W/\bar{d} = \infty$ with periodic side walls), there is a layer (with thickness $3\bar{d} \sim 5\bar{d}$) right after entering the creep regime where the local deformation is larger than one. In these layers, $\delta\theta$ is no longer constant, but rather increases with depth, and the one-to-one $\mu(I)$ relation breaks down. Similar steady creep flow layers with large shear deformation have also been observed in other geometries such as annular shear flow [67] and planar shear flow with gravity [121], in which the break-down of the one-to-one $\mu(I)$ relation is explained by steady-state non-local models. Following these steady creep flow layers deeper into the bulk are the stationary creep flow layers where the local deformation $|\dot{\gamma}^d|/2\Omega$ decreases to less than one. In these stationary creep flow layers the values of $\delta\theta$ continue to increase with depth, and the values of μ keep depending on the values of $\delta\theta$. This result suggests that, the misalignment of force chain direction and preferred contact direction can be caused by either (i) steady-state non-local effect for steady creep flow or (ii) lack of shear deformation for stationary creep flow. Further investigations need to be carried out to distinguish or find connections between the two. For example, it will be helpful to adopt a Lagrangian perspective, where we perform investigations by tracking the trajectory of each particle and examining its correlation with the inter-particle force network.

Figs.3.5(b) and 3.5(c) show the variation of flow thickness $h_{\mathrm{f}} = z_2 - z_{\mathrm{surface}}$ and I_{th} against ω. We observe that the effective drum width W has a stronger effect than side wall friction in changing h_{f}. However its influence seems to decrease as ω increases. The value of I_{th} can not be determined by a single constant as in [45], but depends on the specific drum configuration and rotation speed. In general, weaker boundary effect (larger effective drum width or smaller wall friction) and smaller rotating speed lead to smaller values of I_{th}, in other words, weaker boundary effect and smaller rotation speed can extend the applicability of the classical $\mu(I)$ rheological relation to flows with smaller values of I. This observation is supported by our results from cases with the effective drum width W being around $21\bar{d}$ under different wall friction, and being infinite under periodic side walls. One way to rationalize this is to consider steady state non-local effect, where particles in the creep flow layers may be “agitated" by particles in the fast flowing layers near the free surface. The faster the particles flow in dense and collisional regime, the larger the force fluctuations can they generate to “agitate" particles, presumably via force chains, in the underlying creep regime. As the presence of side wall friction and larger rotation speed can generate faster surface flow, the transition into creep regime (where the $\mu(I)$ relation breaks down) can happen with a larger value of I_{th}. However, for cases with $W/\bar{d} \simeq 10$ the dependence of I_{th} on drum configuration and rotation speed becomes a bit more complicated. At smaller rotation speeds ($\omega \leq 5.73°/\text{s}$), we have consistent observations: the values of I_{th} are at least non-decreasing with increasing rotation speeds, and are larger than those computed from wider drums due to stronger boundary effects, whereas for larger rotation speeds ($\omega \geq 11.23°/\text{s}$), values of I_{th} start to decrease with increasing rotation speeds. Further, at the highest rotation speed ($\omega = 67.38°/\text{s}$) the value of I_{th} decreases to be even smaller than that computed from periodic side wall conditions. We attribute this observation to the influence of effective wall friction [4] which becomes more pronounced under larger rotation speeds, subsequently leading to a faster decay of I along depth than those computed from wider drums. As a consequence, values of I can decrease for an order of magnitude when crossing I_{th}, giving values of I_{th} that decrease with increasing rotation speeds, and giving values of I_{th} that can become smaller than those computed from wider drums.

3.5 Concluding remarks

We propose a micro-structural quantity called $\delta\theta$ whose spatial variation characterizes the internal structure of granular flow in different regimes: (i) it recovers the universal value $I \simeq 0.1$ that corresponds to the transition ($z = z_1$) from collisional regime to dense regime [8] and, more importantly, (ii) it identifies the boundary ($z = z_2 = z_{\text{th}}$) between dense regime and creep regime with the value of $\delta\theta$ governing the variation of μ in the creep regime. The universal value $I \simeq 0.1$ and the both drum-configuration-dependent and rotation-speed-dependent I_{th} are closely related to the respective underlying particle interaction mechanisms: spatially uncorrelated and short-lived binary collisions for I above 0.1 and spatially correlated and enduring contact networks for I below I_{th}.

These findings hold regardless of studied rotating speeds and drum configurations (with or without boundary effects), and hold in the creep regime regardless of the amount of experienced shear deformation. Our findings are thus not only applicable to similar geometries (such as heap flows [66] and silo flows [28]) where shear deformation can also be largely absent in the creep regime, but relevant to other geometries (such as planar flows with gravity [121]) where steady creep flow with large enough shear occurs and is believed to be triggered by steady-state non-local effects. $\delta\theta$ thus provides a unified interpretation of the internal structure of granular flow in all three regimes. In particular, in the creep regime, it suggests that the misalignment between force chain direction and preferred contact direction can be caused by either (i) steady-state non-local effect, or (ii) lack of shear deformation. Further investigations to distinguish or to find connections between them, will be helpful in establishing microstructure-informed granular rheology models with a unified underlying mechanism.

In the future, we plan to extend our work to more realistic (and more complicated) granular materials by gradually adding ingredients like shape [19, 50, 83], deformability [35, 39], and polydispersity [26, 49] - these new ingredients may lead to different interaction mechanism not only between particles, but also between particles and boundaries [74].

Chapter 4

ARCHITECTURED GRANULAR SHEETS WITH ADAPTIVE STIFFNESS

Yifan Wang*, Liuchi Li*, Douglas Hofmann, José E. Andrade, and Chiara Daraio (2020). "Architectured granular sheets with adaptive stiffness." In preparation.

Abstract

In most practical scenarios, the tunable mechanical properties (e.g. stiffness) of granular systems are relatively easily accessible, making them ideal candidates over many architected materials in applications such as soft robotics. However, conventional granular-integrated mechanical systems are heavy and bulky, due to large numbers of particles needed in order to provide desirable range of stiffness tunability. The limitations are majorly due to particles being solid and interacting via non-cohesive forces. Here, we present (together with a prototype) a novel architected textile material with interlocking granular particles. The mechanical properties of the textile can be controlled through granular jamming transition, which makes it a promising candidate for smart wearable materials. We further explore the mechanics of jamming in these interlocked particles and obtain a power-law scaling relationship between the mechanical moduli and average contact number per particle. This scaling is valid for particles with different geometries, which provides guidelines for designing particle geometry for improved textile stiffness at the jammed state. We show that the textiles can also be formed into complex shapes to conform to human bodies and prevent threats from impacting objects. The concept of granular jamming explored in architected textiles is a scale-invariant physical phenomena, therefore recent advances in additive manufacturing make it possible to scaling down the textile thickness making it comparable to other wearable materials.

Architected materials, also referred to as mechanical metamaterials, are materials that derive their mechanical properties from both the selection of their constitutive materials and their arrangement in geometrical structures. After fabrication, the properties of most architected materials are fixed and cannot be tuned over time. This limits their applications in areas where material adaptivity and tunability are required, such as robotic applications. Solutions to tune the mechanical properties of materials and structures include the use of hydrogels that respond to temperature, pH, light and water content; shape memory alloys and polymers; liquid crystal elastomers (LCEs) that respond to temperature and light; and magnetorheological (MR) and electroactive polymers (EAPs). However, these materials are either mechanically too soft for engineering applications (hydrogels), require large temperature changes (LCEs), need re-programming at high temperatures (SMAs and SMPs), or require strong electromagnetic fields (MR materials, EAPs), which are not easily accessible in most practical scenarios.

Granular systems are known to exhibit tunable mechanical properties during jamming, when the packing fraction of the particles is increased. Jamming is a phase transition that does not rely on temperature changes, like in ordinary materials, but it is instead controlled by local geometric constraints. When a granular system jams, it undergoes a sharp transition from a soft to a rigid state, with large increases in stiffness and yield stress. The jamming transition in granular materials has been employed in engineering applications such as soft robotics and granular architectures. However, there are limitations when applying these traditional granular materials in areas such as wearable materials with tunable stiffness. First of all, the density of these granular materials is usually high and their volume needed to provide enough mechanical stiffness is to large for wearable applications. Secondly, no cohesive interactions exist in these non-convex granular particles, which means not enough tensile and bending stiffness is provided by the particle interactions.

To demonstrate the proposed architected textile, we fabricated a sample consisting topologically interlocked octahedra frame particles (Figure 4.1). The octahedra geometry is chosen as an example with a 90 degree rotational symmetry, which forms a square lattice in the textile. The resulting textile exhibits interesting mechanical behaviors: Firstly, the fabricated textile has little bending stiffness since no solid connection exists between neighboring particles. This feature makes it suitable for wearable materials, where frequent bending deformations are expected at the body joints. In addition, the textile exhibits strong resistance to tensile deformation, which contrasts it from non-cohesive granular aggregates and helps it to maintain structural integrity.

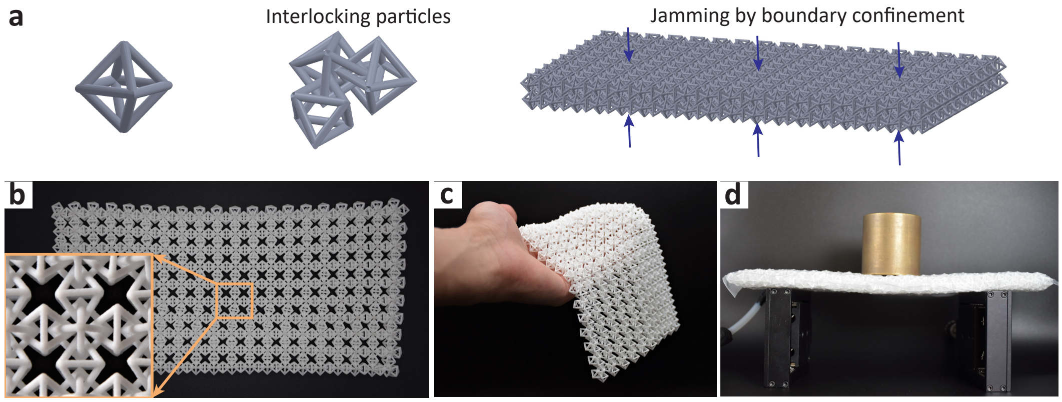

Figure 4.1: The designed textile prototype with bending stiffness adaptivity. (a) The designed octahedral particle (left), a demonstration of three octahedral particles interlocked together (middle) and two granular sheets stacked on top of each other and driven to jammed state by boundary confinement. (b) A top-down view of a single layer of granular sheet composed of interlocked octahedral particles (shown in the inset). (c) A single layer sheet is soft in the unjammed state in the absence of boundary confinement. (d) Two vertically stacked sheets become rigid (and load-bearing) in the jammed state driven by boundary confinement.

More interesting behaviors are observed when two layers of these textiles are stacked together and confined in an air-tight flexible envelope. When no pressure difference exists between the inside and outside of the envelope, the textiles can bend easily as very little coupling exists between the two layers (the remaining coupling comes from the gravity of the top layer). However, when confinement stress is applied to the textiles' boundaries with negative pressure inside the envelope, jamming transition of these interlocked particles takes place as their packing fraction increases. The jamming transition significantly increases the bending stiffness of the textiles and converts them to a load-bearing structure (Figure 4.1d).

To obtain quantitative information on the evolution of the textiles' mechanical properties between the unjammed and jammed states, we performed 3-point bending measurements on the enveloped textiles under increasing negative pressure confinements (Figure 4.2). The force-displacement curves demonstrate an initial linear elastic regime governed by the elasticity of the jammed structure, followed by a yielding regime caused by frictional deformation between the particles. The stiffness of the initial elastic regime increases monotonically when the internal negative gauge pressure is raised. As the internal gauge pressure increases from 0 to 93.3 kPa, the bending stiffness increases from 0.24 N/mm to 6.3 N/mm. The large changes in bending stiffness, by over an order of magnitude, surpass most other variable stiffness materials.

In order to understand the experimentally observed stiffness adaptations, we perform numerical simulations using LS-DEM (Level Set-Discrete Element Method [62, 63, 69]). LS-DEM goes beyond conventional Discrete Element Method (DEM [33]) in the sense that it accounts for arbitrary particle shape via level set representation [118] and particle surface triangulation. In our simulations, we construct the same octahedral particle designed for experiments, and we replicate the 3D printed granular sheet. We stack two layers of such granular sheets on top of each other and encompass them with a rectangular-shaped membrane modeled by spheres connected through normal and shear springs. We first impose isotropic pressure to the membrane which in response compresses the sheets, after relaxation is done (Figure 4.2a) we next additionally impose loads following the three-point bending protocol, and finally we compute the stiffness in the small strain limit. We use the experimental results measured under the highest confining pressure to calibrate our numerical model, and we use the remaining experimental results as validations.

Our simulations can quantitatively capture the bending stiffness variation against confining pressure (Figure 4.2c) – the dashed line and the shaded area indicates the mean stiffness and the variations from four different initial configurations, respectively. Further, to estimate the significance of having particle interlocked, we perform numerical three-point bending tests on jammed discrete assemblies of the same octahedral without interlocking. We make sure the dimension of the jammed assemblies (length, width and height) stays as close to that of the jammed interlocking sheets, such that the computed stiffness from discrete assemblies and interlocking sheets can be directly compared with each other. It can be observed that interlocked sheets outperform discrete assemblies - the former has around 26 times of increase as the confining pressure is increased from 0 kPa to 93.3 kPa, while correspondingly the later only has around 8 times of increase (Figure 4.2c).

To further explore the effect of particle shape, we utilize this validated DEM model to study the mechanical response of interlocking sheets composed of particles other than octahedral. In this work we consider only identical particle replication, i.e. no spatial shape variation within any designed sheets. Considering the interlocking pattern, we design five additional particle shapes that lead to six different types of sheets (Figure 4.3).

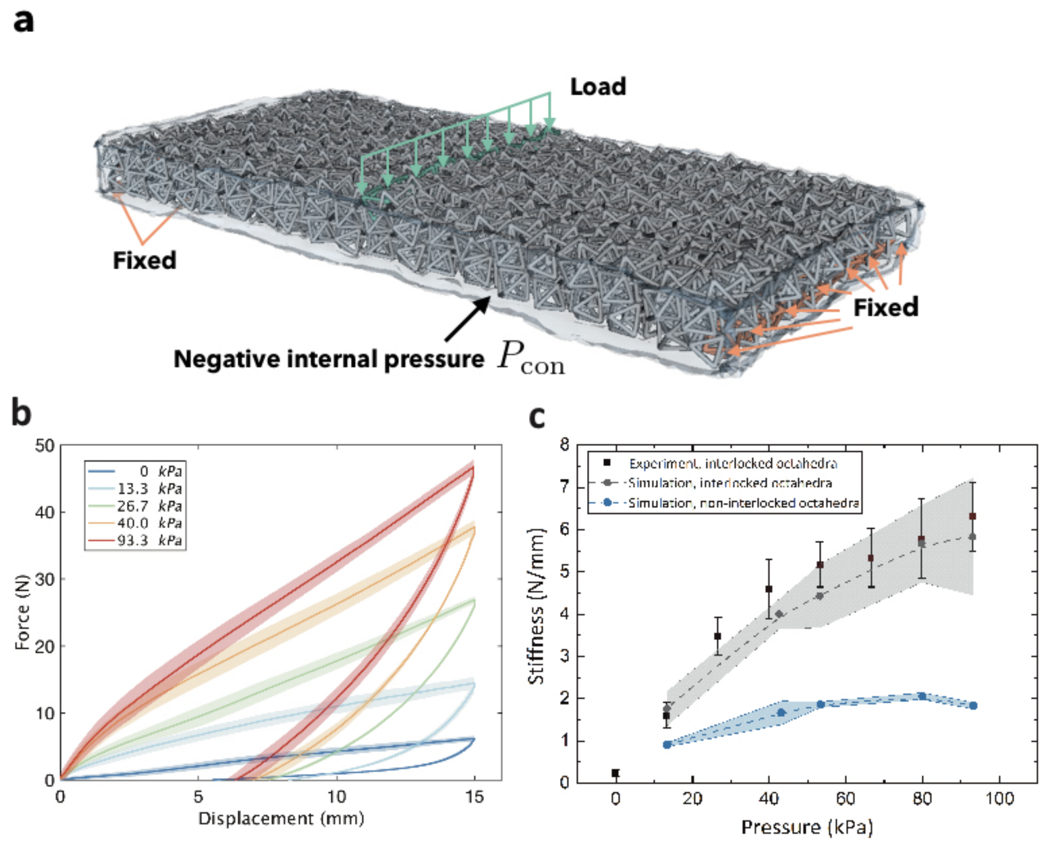

Figure 4.2: Simulation setup with simulation results. (a). In LS-DEM simulation, a 3D view of the granular sheets composed of octahedral particles together with the deformed membrane, right after compression relaxation but right before three-point bending; particles colored in green are those will be loaded during the following three-point bending test while particles colored in red at the two ends will be fixed during the following three-point bending test. (b) Loading-displacement curves obtained from experiments of three-point bending and unbending of octahedral sheets under five different confining pressures: 0 kPa (deep blue), 13.3 kPa (light blue), 26.7 kPa (light green), 40 kPa (light orange) and 93.3 (red); the solid lines and the corresponding shaded areas show the averaged results and the corresponding variation from four independent experiments. (c) At the small-strain limit, the elastic bending stiffness variation of interlocking octahedral sheets against confining pressure measured from experiments (black) and LS-DEM simulations (grey), and similarly the bending stiffness variation of octahedral assemblies without interlocking (light blue); for experiment results, the error bars indicate the variation measured from four repeated independent experiments, while for simulation results, the corresponding shaded area indicates the variation computed from four simulations, each of which has a different initial configuration regarding the octahedral particles' initial positions.

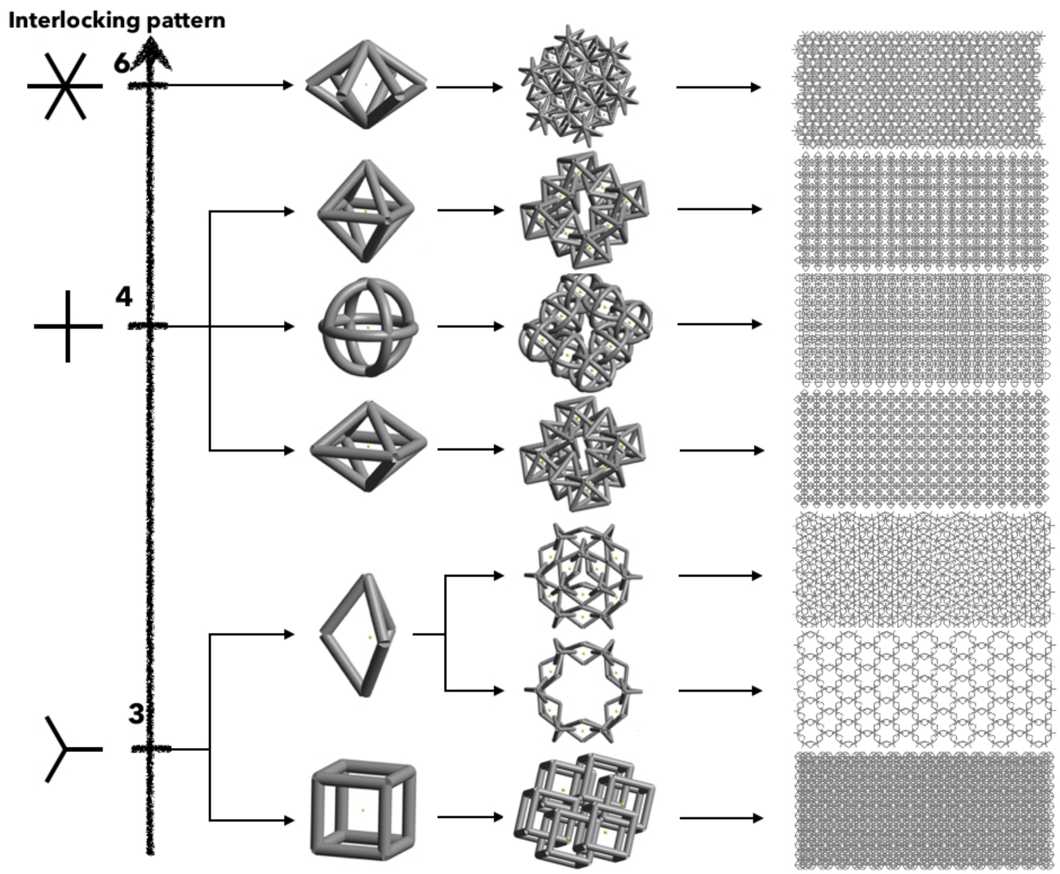

Figure 4.3: All investigated granular sheets following different interlocking pattern, from left to right the demonstrations of: designed particle shape, formed unit cell and formed single-layer sheet.

For each of the designed shape, we use the same thickness for the constituent bars as those from octahedral, and we choose its size such that the constructed vertically stacked two layers of sheets can be fit into the constructed membrane. Lastly, for triangulation mesh of each designed particle, we make sure the probability distribution of all edge lengths matches the one for octahedral - in this way we make sure the mechanical responses of all designed sheets are consistent with that of the octahedral sheets. For each simulation, after relaxation is done but before the three-point bending test, we record the dimension of each jammed sheets and the mean contact number of constituent particle. Similarly, from the three-point bending simulation we compute the elastic bending stiffness at small-strain limit. The elastic flexural modulus then can be computed following the formula below according to the fundamental beam theory:

$$E_\mathrm{f} = \frac{KL^3}{4bh^3}, \tag{4.1}$$

where E_f is the elastic flexural modulus, K is the elastic bending stiffness computed from three-point bending test, and L, b, and h are the length, width and height of the isotropically jammed sheets right after completing compression relaxation, but right before performing three-point bending. We observe that when plotting the elastic modulus E_f against mean particle contact number $\langle Z \rangle$, all data collapse onto a single master curve characterized by a power-law scaling with an exponent around 3 (Figure 4.4a). Note that when fitting, data computed at zero confining pressure is excluded. This is because the corresponding mean particle contact number is smaller than two, and as such, the bending stiffness (therefore the flexural modulus as well) computed is highly affected by the elongation of the enveloping membrane. Indeed, the fitted power-law predicts the values of elastic flexural modulus under zero confining pressure deviating from numerically computed ones (see inset of Figure 4.4a). In addition, we observe that the class of particle shape with a square-like interlocking pattern outperforms other classes of particle shapes investigated, due to larger average numbers induced upon confining isotropically. For instance, at confining pressure 90 kPa, 40kPa, and 2 kPa, octahedral sheets have larger particle contact number over cubical frame sheets, as shown in Figure 4.4b where the color of each particle is scaled by its contact number. We should point out that the value of the scaling exponent may change if we change the constituent material in fabricating our granular sheets. As such, using stiffer constituent materials may give an even wider range of flexural modulus tunability. Studies on how the scaling exponent will depend on the stiffness of constituent material merit further investigations.

Interestingly, such power-law scaling has been previously identified from computational studies on assemblies of frictionless spheres under periodic boundary conditions, where the corresponding bulk modulus and shear modulus have a power-law dependence on the average contact number, with the scaling exponent close to one near jamming [85]. As we mainly aim at evaluating the bending performance, it would be interesting in the future to see whether the bulk and shear modulus of the designed granular sheets also have similar power-law scaling, and if so, how would the scaling exponent compare to that of assemblies of frictionless spheres. In all, by linking a micro-scale geometrical quantity (mean contact number) to a macro-scale mechanical quantity (flexural modulus), the discovered universal power-law scal-

(a)

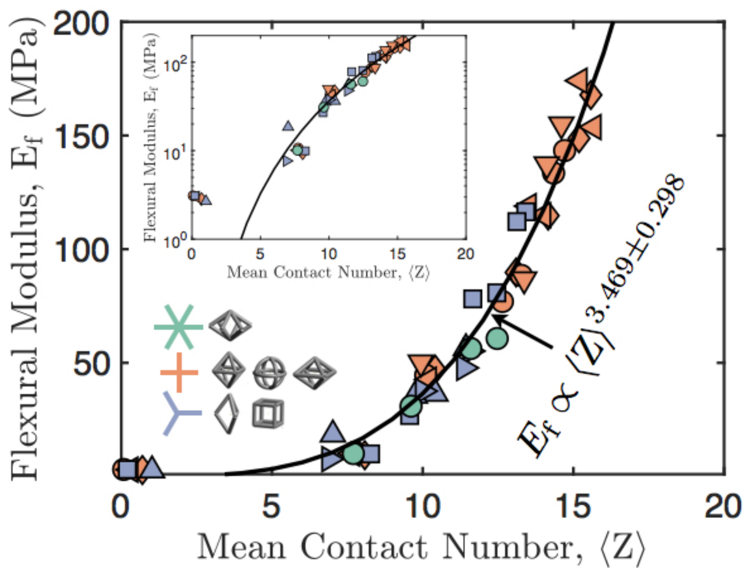

(b)

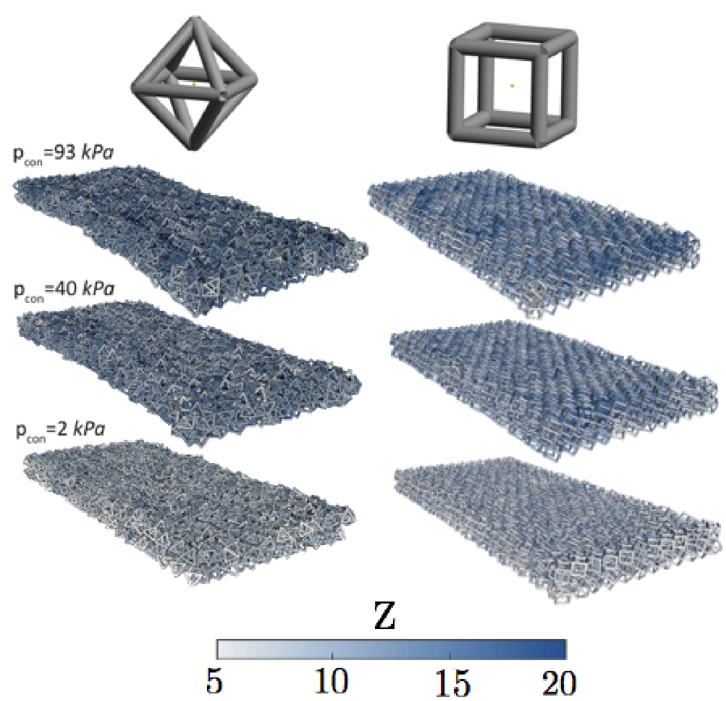

Figure 4.4: The power-law scaling between flexural modulus and average contact number. (a) Relation between elastic flexural modulus E_f and mean particle contact number $\langle Z\rangle$ for all investigated granular sheets, all data except those collected from zero confining pressure collapse onto a single master curve characterized by a power-law scaling (black solid line) with a universal scaling exponent whose value is around 3. Inset: same plot but in semi-log scale, it can be observed more clearly that data collected from zero confining pressure deviate from the power-law scaling. (b) Demonstrations of jammed granular sheets right before three-point bending for octahedral particles (left column) and cubical frame particles (right column) under three different confining pressures: 93 kPa (first row), 40 kPa (second row) and 2 kPa (third row), the color of each particle is scaled by the corresponding contact number it has.

ing has practical implications in rational design of such granular sheets for desired performance for choosing the right constituent particle shape.

Besides flat shapes, we further demonstrate the ability to form these textiles into structures with different shapes for desired applications. In the unjammed state, the enveloped textiles are flexible and can be formed in the desired shape. Negative internal pressure will then be applied to jam the textiles into the pre-formed geometry creating a load-bearing structure. Examples show that the textiles are forming a table shape (Figure 4.5a) and an arched shape (Figure 4.5b). The ability to morph into different shapes is especially important for wearable applications, where the textiles need to conform to human bodies with complex geometries.

Finally, we demonstrate the textiles' ability to protect threats from dynamic impacts. A drop-weight impact test is performed by dropping a steel bead on the textiles at varying negative internal pressures. The impact process is recorded by a high-speed camera. The test results show that the penetration depth can be significantly reduced with increased negative internal pressure: from 26mm at 0 kPa to 4mm at 66.7 kPa. These results demonstrate that the textiles can adjust their elastic stiffness and damping properties to adapt to impact threats and protect the wearer's body.

In summary, we present a novel architected textile material with interlocking granular particles. The mechanical properties of the textile can be controlled through granular jamming transition, which makes it a promising candidate for smart wearable materials. We further explored the mechanics of jamming in these interlocked particles and obtained a scaling relationship between the mechanical moduli and average contact number per particle. This scaling is valid for particles with different geometries, which provides guidelines for designing particle geometry for improved textile stiffness at the jammed state. The textiles can also be formed into complex shapes to conform to human bodies and prevent threats from impacting objects. The concept of granular jamming explored in the architected textiles is a scale-invariant physical phenomena. Recent advances in additive manufacturing make it possible to scaling down the textile thickness comparable to other wearable materials. With the integration of smart control on the boundary confinement stresses, the textiles can obtain programmed stiffnesses at different locations, which can be applied in haptic perception devices for virtual reality applications.

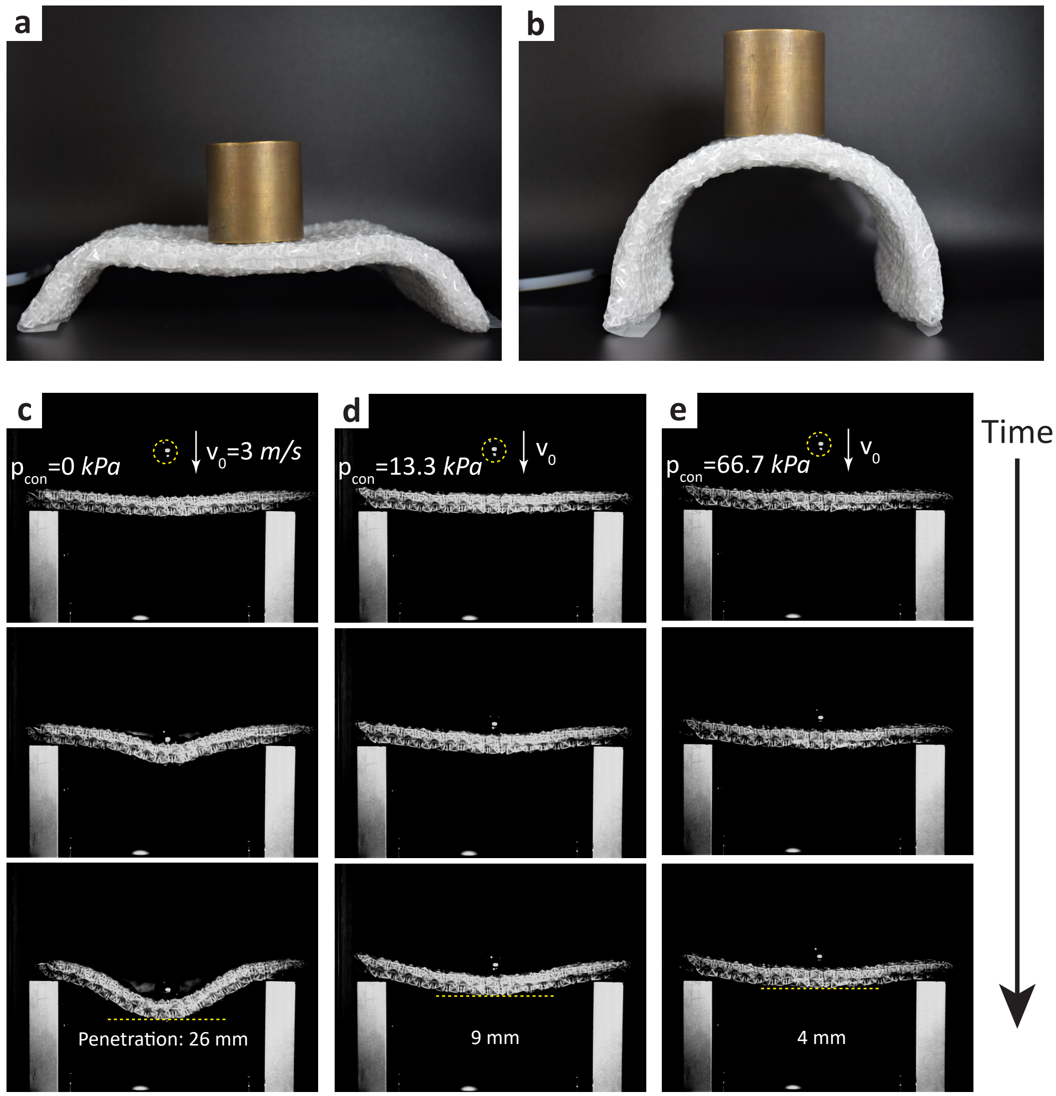

Figure 4.5: Examples of reconfigured structures with load-bear abilities. (a) and (b) Demonstrations of the ability of the jammed granular sheets to morph into different load-bearing structures: in (a) table-like shape and in (b) arch-like shape. (c) Without confining pressure, snapshots of the dynamical deformation of the granular sheets when impacted by a steel bead released from above with an initial velocity of 3 m/s, image at the third row shows a maximum penetration depth of 26 mm. (b) Same snapshots but with the granular sheets under a confining pressure of 13.3 kPa. (e) Same snapshots but with the granular sheets under a confining pressure of 66.7 kPa.

Chapter 5

CONCLUSION AND FUTURE OUTLOOK

Better controlling and utilizing granular matter pivots on developing a micro-structural understanding of the two basic macro-behaviors of granular matter: flowing heterogeneously and morphing adaptively. In this thesis, we have bridged the length-scale divide in this regard. We have linked the underpinning micro-structures with the overlaying macro-behaviors in terms of heterogeneous flows and shape-morphing assemblies. In order to access the micro-scale details, we mainly perform computational studies resorting to the (Level-set) Discrete Element Method. Meanwhile, experimental work is also carried out in tandem, guiding and validating our computational studies on capturing phenomena observed at the macro-scale.

In Chapter 2, we first test and validate the robustness of (LS-)DEM in capturing granular microstructures by comparing its simulation results with experimental measurments. We consider granular microstructures in terms of the polar diagram of the contact force magnitude, the polar diagram of the friction mobilization, and the angular distribution of the contact orientation. When quasi-statically shearing, we find that for both assemblies of circular-shaped particles and assemblies of arbitrarily-shaped particles, (LS-)DEM can faithfully capture the evolution of both macro-scale responses (e.g. dilation and effective stress) and microstructures as mentioned above.

In Chapter 3, we investigate spatial phase transitions in heterogeneous granular flows. We focus on the model granular matter - collections of (quasi-)spherical particles - developing heterogeneous flows in rotating drum systems, from a top-down perspective. Based on our calibrated (LS-)DEM model using experimental measurements of glass beads flowing in a rotating drum, we produce various microstructures of the generated flow fields by systematically varying boundary conditions and loading rates, and we study their correlations with spatial phase transitions. We identify a micro-scale parameter quantifying the structural anisotropy, that can for the first time pinpoint the spatial phase transitions starting from gas-like layers near the free surface, next transitioning into underlying liquid-like layers, and finally transitioning into solid-like layers deep in the bulk. We have also identified a universal correlation between this micro-scale parameter and effective bulk friction, an integral macro-scale quantity in constitutive modeling.

In Chapter 4, we investigate modulus adaptations in shape-morphing granular assemblies, from a bottom -up perspective. We design the shape of constituent particle and arrange such particles in space to construct interlocking granular sheets via 3D printing. After they are enclosed in flexible membranes and subjected to different levels of isotropic pressure, such granular sheets exhibit exceptional shape-morphing capabilities that are enabled by their bending moduli's adaptations. Then based on our calibrated (LS-)DEM model using experimental measurements, we probe different microstructures of the constructed granular sheets by varying the shape of the constituent particle and also varying the level of imposed isotropic pressure. We next study their correlations with bending moduli adaptations. We discover a universal power-law scaling between the bending modulus (a macro-scale quantity) and the coordination number (a micro-scale quantity), with the power exponent being independent of the constituent particle shape, the initial configuration and the imposed pressure level. We also show that such interlocking granular sheets outperform discrete granular assemblies by inducing larger coordination numbers.

In all, our work has bridged the length-scale divide in linking micro-structures of granular matter with their two basic macro-scale behaviors: flowing heterogeneously and morphing adaptively. Built upon such understandings, our work also raises several important questions that remain to be answered regarding understanding the physics and mechanics of granular matter.

For instance, in Chapter 4 we present the underpinning micro-structural interpretations of the overlaying spatial phase transitions in heterogeneous flows at the macro-scale. Two important questions lie ahead. First, what are the "resources" leading to the formation of the corresponding microstructures in different phase regimes? Investigations along this line may adopt a Lagrangian perspective by tracking the trajectories of particles in different phase regimes and analyzing their correlations with the contact force network. Such investigations may help us establish connections to the kinematical fields, which will subsequently lead to establishing robust rheology models describing granular matter. Second, what will happen if more ingredients are considered regarding granular matter, such as particle shape, size polydispersity and elasticity. Understanding the contributions of these ingredients will help us refine the rheology models so that they can be applied to address much more real world challenges, e.g. designing more efficient industrial equipments to handle natural granular matter. In Chapter 5, we effectively propose a design protocol for designing shape-morphing granular sheets, and we show that better performance is promoted by constituent particle shape that induces a larger coordination number. However, our work is limited to cases where (1) constituent particles are of the same shape, same size and same elasticity and (2) quasi-static applications. Similarly, there are many more exciting opportunities lying ahead regarding customizing particle details in the aforementioned three aspects and the corresponding dynamical applications such as impact cushioning.

Lastly, our work focuses on phenomena of granular matter near equilibrium: dynamic equilibrium for heterogenous flows and quasi-static equilibrium for shape-morphing granular sheets. Such near equilibrium conditions allow us to establish statistically representative mappings between macro-scale behaviors and the underpinning microstructures. However, many macro-scale behaviors of granular matter of interest can also be far from equilibrium. Examples are flow arrest in hopper discharge, the onset of landslides and the dynamical response of shape-morphing granular assemblies. It thus becomes challenging to establish a statistically representative mapping between the macro and the micro, due to the enormously large microstructure phase space in need of exploring. In addition, accompanying the enormously large phase space is the increasing difficulty in identifying the relevant ingredients of microstructure in different scenarios. Thus, how to extend our work to phenomena far from equilibrium also opens many future research venues. With the rapid advances in computation capability, techniques such as machine learning and data driven algorithm may be particularly useful in this regard in the future.

BIBLIOGRAPHY

[1] *Vic-2D, Reference Manual*. URL http://www.correlatedsolutions.com/supportcontent/Vic-2D-v6-Manual.pdf.

[2] Jun Ai, Jian-Fei Chen, J Michael Rotter, and Jin Y Ooi. Assessment of rolling resistance models in discrete element simulations. *Powder Technology*, 206 (3):269–282, 2011.

[3] J.E. Andrade and C.F. Avila. Granular element method (gem): linking inter-particle forces with macroscopic loading. *Granular Matter*, 14:51–61, 2012.

[4] Riccardo Artoni and Patrick Richard. Effective wall friction in wall-bounded 3d dense granular flows. *Physical review letters*, 115(15):158001, 2015.

[5] Athanasios G Athanassiadis, Marc Z Miskin, Paul Kaplan, Nicholas Rodenberg, Seung Hwan Lee, Jason Merritt, Eric Brown, John Amend, Hod Lipson, and Heinrich M Jaeger. Particle shape effects on the stress response of granular packings. *Soft Matter*, 10(1):48–59, 2014.

[6] Emilien Azéma and Farhang Radjaï. Stress-strain behavior and geometrical properties of packings of elongated particles. *Physical Review E*, 81(5): 051304, 2010.

[7] Emilien Azéma and Farhang Radjaï. Force chains and contact network topology in sheared packings of elongated particles. *Physical review E*, 85(3): 031303, 2012.

[8] Emilien Azéma and Farhang Radjai. Internal structure of inertial granular flows. *Physical review letters*, 112(7):078001, 2014.

[9] Emilien Azéma, Farhang Radjai, Robert Peyroux, and Gilles Saussine. Force transmission in a packing of pentagonal particles. *Physical Review E*, 76(1): 011301, 2007.

[10] Emilien Azéma, Farhang Radjai, and Gilles Saussine. Quasistatic rheology, force transmission and fabric properties of a packing of irregular polyhedral particles. *Mechanics of Materials*, 41(6):729–741, 2009.

[11] Emilien Azéma, Yannick Descantes, Nicolas Roquet, Jean-Noël Roux, and François Chevoir. Discrete simulation of dense flows of polyhedral grains down a rough inclined plane. *Physical Review E*, 86(3):031303, 2012.

[12] Emilien Azéma, Nicolas Estrada, and Farhang Radjai. Nonlinear effects of particle shape angularity in sheared granular media. *Physical Review E*, 86 (4):041301, 2012.

[13] Emilien Azéma, Farhang Radjai, and Frédéric Dubois. Packings of irregular polyhedral particles: Strength, structure, and effects of angularity. *Physical Review E*, 87(6):062203, 2013.

[14] Emilien Azéma, Itthichai Preechawuttipong, and Farhang Radjai. Binary mixtures of disks and elongated particles: Texture and mechanical properties. *Physical Review E*, 94(4):042901, 2016.

[15] Oleh Baran, Deniz Ertaş, Thomas C Halsey, Gary S Grest, and Jeremy B Lechman. Velocity correlations in dense gravity-driven granular chute flow. *Physical Review E*, 74(5):051302, 2006.

[16] D Bonamy, F Daviaud, and L Laurent. Experimental study of granular surface flows via a fast camera: a continuous description. *Physics of fluids*, 14(5): 1666–1673, 2002.

[17] D Bonamy, F Daviaud, L Laurent, M Bonetti, and JP Bouchaud. Multiscale clustering in granular surface flows. *Physical review letters*, 89(3):034301, 2002.

[18] Tamás Börzsönyi, Robert E Ecke, and Jim N McElwaine. Patterns in flowing sand: understanding the physics of granular flow. *Physical review letters*, 103(17):178302, 2009.

[19] Tamás Börzsönyi, Balázs Szabó, Gábor Törös, Sandra Wegner, János Török, Ellák Somfai, Tomasz Bien, and Ralf Stannarius. Orientational order and alignment of elongated particles induced by shear. *Physical review letters*, 108(22):228302, 2012.

[20] Mehdi Bouzid, Martin Trulsson, Philippe Claudin, Eric Clément, and Bruno Andreotti. Nonlocal rheology of granular flows across yield conditions. *Physical review letters*, 111(23):238301, 2013.

[21] Mehdi Bouzid, Adrien Izzet, Martin Trulsson, Eric Clément, Philippe Claudin, and Bruno Andreotti. Non-local rheology in dense granular flows. *The European Physical Journal E*, 38(11):125, 2015.

[22] Nicolas Brodu, Patrick Richard, and Renaud Delannay. Shallow granular flows down flat frictional channels: Steady flows and longitudinal vortices. *Physical Review E*, 87(2):022202, 2013.

[23] Nicolas Brodu, Joshua A Dijksman, and Robert P Behringer. Spanning the scales of granular materials through microscopic force imaging. *Nature communications*, 6:6361, 2015.

[24] Eric Brown, Nicholas Rodenberg, John Amend, Annan Mozeika, Erik Steltz, Mitchell R Zakin, Hod Lipson, and Heinrich M Jaeger. Universal robotic gripper based on the jamming of granular material. *Proceedings of the National Academy of Sciences*, 107(44):18809–18814, 2010.

[25] Jean-François Camenen, Yannick Descantes, and Patrick Richard. Effect of confinement on dense packings of rigid frictionless spheres and polyhedra. *Physical Review E*, 86(6):061317, 2012.

[26] David Cantor, Emilien Azéma, Philippe Sornay, and Farhang Radjai. Rheology and structure of polydisperse three-dimensional packings of spheres. *Physical Review E*, 98(5):052910, 2018.

[27] Gye-Chun Cho, Jake Dodds, and J Carlos Santamarina. Particle shape effects on packing density, stiffness, and strength: natural and crushed sands. *Journal of geotechnical and geoenvironmental engineering*, 132(5):591–602, 2006.

[28] Jaehyuk Choi, Arshad Kudrolli, Rodolfo R Rosales, and Martin Z Bazant. Diffusion and mixing in gravity-driven dense granular flows. *Physical review letters*, 92(17):174301, 2004.

[29] J Christoffersen, MM Mehrabadi, and Sia Nemat-Nasser. A micromechanical description of granular material behavior. *Journal of applied mechanics*, 48 (2):339–344, 1981.

[30] Abram H Clark, Jacob D Thompson, Mark D Shattuck, Nicholas T Ouellette, and Corey S O'Hern. Critical scaling near the yielding transition in granular media. *Physical Review E*, 97(6):062901, 2018.

[31] Ray W Clough and Joseph Penzien. Dynamics of structures. berkeley: Computers & structures, 1995.

[32] P-P Cortet, D Bonamy, F Daviaud, Olivier Dauchot, Bérengere Dubrulle, and M Renouf. Relevance of visco-plastic theory in a multi-directional inhomogeneous granular flow. *EPL (Europhysics Letters)*, 88(1):14001, 2009.

[33] Peter A Cundall and Otto DL Strack. A discrete numerical model for granular assemblies. *geotechnique*, 29(1):47–65, 1979.

[34] Frédéric Da Cruz, Sacha Emam, Michaël Prochnow, Jean-Noël Roux, and François Chevoir. Rheophysics of dense granular materials: Discrete simulation of plane shear flows. *Physical Review E*, 72(2):021309, 2005.

[35] Adeline Favier de Coulomb, Mehdi Bouzid, Philippe Claudin, Eric Clément, and Bruno Andreotti. Rheology of granular flows across the transition from soft to rigid particles. *Physical Review Fluids*, 2(10):102301, 2017.

[36] S Courrech Du Pont, P Gondret, Bernard Perrin, and M Rabaud. Wall effects on granular heap stability. *EPL (Europhysics Letters)*, 61(4):492, 2003.

[37] Denis Dumont, Maurine Houze, Paul Rambach, Thomas Salez, Sylvain Patinet, and Pascal Damman. Emergent strain stiffening in interlocked granular chains. *Physical review letters*, 120(8):088001, 2018.

[38] Nicolas Estrada, Emilien Azéma, Farhang Radjai, and Alfredo Taboada. Identification of rolling resistance as a shape parameter in sheared granular media. *Physical Review E*, 84(1):011306, 2011.

[39] Yi Fan, Paul B Umbanhowar, Julio M Ottino, and Richard M Lueptow. Shear-rate-independent diffusion in granular flows. *Physical review letters*, 115(8): 088001, 2015.

[40] Somayeh Farhadi and Robert P Behringer. Dynamics of sheared ellipses and circular disks: effects of particle shape. *Physical review letters*, 112(14): 148301, 2014.

[41] Jean-Francois Ferellec and Glenn R McDowell. A method to model realistic particle shape and inertia in dem. *Granular Matter*, 12(5):459–467, 2010.

[42] DuPont Fluoroproducts. Teflon® ptfe fluoropolymer resin: Properties handbook. Technical report, DuPontTM Technical Report H-37051-3, 1996.

[43] Yoël Forterre and Olivier Pouliquen. Flows of dense granular media. *Annu. Rev. Fluid Mech.*, 40:1–24, 2008.

[44] Piotr Frankowski and Martin Morgeneyer. Calibration and validation of dem rolling and sliding friction coefficients in angle of repose and shear measurements. In *AIP Conference Proceedings*, volume 1542, pages 851–854. AIP, 2013.

[45] Johan Gaume, Guillaume Chambon, and Mohamed Naaim. Quasistatic to inertial transition in granular materials and the role of fluctuations. *Physical Review E*, 84(5):051304, 2011.

[46] Isaac Goldhirsch. Rapid granular flows. *Annual review of fluid mechanics*, 35(1):267–293, 2003.

[47] R.C. Gonzalez, R.E. Woods, and S.L. Eddins. *Digital Image Processing using Matlab*. Pearson Prentice Hall, New Jersey, 2004.

[48] Nick Gravish, Scott V Franklin, David L Hu, and Daniel I Goldman. Entangled granular media. *Physical review letters*, 108(20):208001, 2012.

[49] John Mark Nicholas Timm Gray. Particle segregation in dense granular flows. *Annual Review of Fluid Mechanics*, 50:407–433, 2018.

[50] RC Hidalgo, B Szabó, K Gillemot, T Börzsönyi, and T Weinhart. Rheological response of nonspherical granular flows down an incline. *Physical Review Fluids*, 3(7):074301, 2018.

[51] Melany L Hunt and Nathalie M Vriend. Booming sand dunes. *Annual Review of Earth and Planetary Sciences*, 38:281–301, 2010.

[52] RC Hurley, SA Hall, JE Andrade, and J Wright. Quantifying interparticle forces and heterogeneity in 3d granular materials. *Physical review letters*, 117(9):098005, 2016.

[53] RC Hurley, KW Lim, G Ravichandran, and JE Andrade. Dynamic interparticle force inference in granular materials: method and application. *Experimental Mechanics*, 56(2):217–229, 2016.

[54] Ryan Hurley, Eloïse Marteau, Guruswami Ravichandran, and José E. Andrade. Extracting inter-particle forces in opaque granular materials: Beyond photoelasticity. *Journal of the Mechanics and Physics of Solids*, 63:154 – 166, 2014.

[55] N Iikawa, MM Bandi, and H Katsuragi. Sensitivity of granular force chain orientation to disorder-induced metastable relaxation. *Physical review letters*, 116(12):128001, 2016.

[56] Heinrich M Jaeger, Sidney R Nagel, and Robert P Behringer. Granular solids, liquids, and gases. *Reviews of modern physics*, 68(4):1259, 1996.

[57] Heinrich M Jaeger, Sidney R Nagel, and Robert P Behringer. The physics of granular materials. *Physics today*, 49:32–39, 1996.

[58] Michel Jean. The non-smooth contact dynamics method. *Computer methods in applied mechanics and engineering*, 177(3-4):235–257, 1999.

[59] Pierre Jop, Yoël Forterre, and Olivier Pouliquen. Crucial role of sidewalls in granular surface flows: consequences for the rheology. *Journal of Fluid Mechanics*, 541:167–192, 2005.

[60] Pierre Jop, Yoël Forterre, and Olivier Pouliquen. A constitutive law for dense granular flows. *Nature*, 441:727–730, 2006.

[61] Ken Kamrin and Georg Koval. Nonlocal constitutive relation for steady granular flow. *Physical Review Letters*, 108(17):178301, 2012.

[62] Reid Kawamoto, Edward Andò, Gioacchino Viggiani, and José E Andrade. Level set discrete element method for three-dimensional computations with triaxial case study. *Journal of the Mechanics and Physics of Solids*, 91:1–13, 2016.

[63] Reid Kawamoto, Edward Andò, Gioacchino Viggiani, and José E Andrade. All you need is shape: Predicting shear banding in sand with ls-dem. *Journal of the Mechanics and Physics of Solids*, 111:375–392, 2018.

[64] Prashidha Kharel and Pierre Rognon. Vortices enhance diffusion in dense granular flows. *Physical review letters*, 119(17):178001, 2017.

[65] Christoph Kloss, Christoph Goniva, Alice Hager, Stefan Amberger, and Stefan Pirker. Models, algorithms and validation for opensource dem and cfd–dem. *Progress in Computational Fluid Dynamics, an International Journal*, 12(2-3):140–152, 2012.

[66] Teruhisa S Komatsu, Shio Inagaki, Naoko Nakagawa, and Satoru Nasuno. Creep motion in a granular pile exhibiting steady surface flow. *Physical review letters*, 86(9):1757, 2001.

[67] Georg Koval, Jean-Noël Roux, Alain Corfdir, and François Chevoir. Annular shear of cohesionless granular materials: From the inertial to quasistatic regime. *Physical Review E*, 79(2):021306, 2009.

[68] H Kruggel-Emden, E Simsek, S Rickelt, S Wirtz, and V Scherer. Review and extension of normal force models for the discrete element method. *Powder Technology*, 171(3):157–173, 2007.

[69] Liuchi Li, Eloïse Marteau, and José E Andrade. Capturing the inter-particle force distribution in granular material using ls-dem. *Granular Matter*, 21(3): 43, 2019.

[70] Keng-Wit Lim and José E Andrade. Granular element method for three-dimensional discrete element calculations. *International Journal for Numerical and Analytical Methods in Geomechanics*, 38(2):167–188, 2014.

[71] K.W. Lim, R. Kawamoto, E. Andò, G. Viggiani, and J.E. Andrade. Multiscale characterization and modeling of granular materials through a computational mechanics avatar: a case study with experiment. *Acta Geotechnica*, 11: 243–253, 2016.

[72] Stefan Luding. Introduction to discrete element methods: basic of contact force models and how to perform the micro-macro transition to continuum theory. *European Journal of Environmental and Civil Engineering*, 12(7-8): 785–826, 2008.

[73] Trushant S Majmudar and Robert P Behringer. Contact force measurements and stress-induced anisotropy in granular materials. *Nature*, 435(7045):1079, 2005.

[74] Sandip Mandal and DV Khakhar. Sidewall-friction-driven ordering transition in granular channel flows: Implications for granular rheology. *Physical Review E*, 96(5):050901(R), 2017.

[75] Theodore Marschall and S Teitel. Compression-driven jamming of athermal frictionless spherocylinders in two dimensions. *Physical Review E*, 97(1): 012905, 2018.

[76] E. Marteau and J.E. Andrade. A novel experimental device for investigating the multiscale behavior of granular materials under shear. *Granular Matter*, 19:77, 2017.

[77] E Marteau and J.E. Andrade. Do force chains exist? effect of grain shape on force transmission and mobilized strength of granular materials. *Journal of the Mechanics and Physics of Solids*, XXX(XXX):XXX, 2018.

[78] GDR MiDi. On dense granular flows. *European Physical Journal E–Soft Matter*, 14(4), 2004.

[79] Thomas Miller, P Rognon, B Metzger, and I Einav. Eddy viscosity in dense granular flows. *Physical review letters*, 111(5):058002, 2013.

[80] Pierre Mills, PG Rognon, and François Chevoir. Rheology and structure of granular materials near the jamming transition. *EPL (Europhysics Letters)*, 81(6):64005, 2008.

[81] Daniel M Mueth, Georges F Debregeas, Greg S Karczmar, Peter J Eng, Sidney R Nagel, and Heinrich M Jaeger. Signatures of granular microstructure in dense shear flows. *Nature*, 406(6794):385, 2000.

[82] Kieran A Murphy, Nikolaj Reiser, Darius Choksy, Clare E Singer, and Heinrich M Jaeger. Freestanding loadbearing structures with z-shaped particles. *Granular Matter*, 18(2):26, 2016.

[83] B Nadler, F Guillard, and I Einav. Kinematic model of transient shape-induced anisotropy in dense granular flow. *Physical Review Letters*, 120(19): 198003, 2018.

[84] Kiri Nichol, Alexey Zanin, Renaud Bastien, Elie Wandersman, and Martin van Hecke. Flow-induced agitations create a granular fluid. *Physical review letters*, 104(7):078302, 2010.

[85] Corey S O?hern, Leonardo E Silbert, Andrea J Liu, and Sidney R Nagel. Jamming at zero temperature and zero applied stress: The epitome of disorder. *Physical Review E*, 68(1):011306, 2003.

[86] Ashish V Orpe and Arshad Kudrolli. Velocity correlations in dense granular flows observed with internal imaging. *Physical review letters*, 98(23):238001, 2007.

[87] B. Pan, K. Qian, H. Xie, and A. Asundi. Robust full-field measurement considering rotation using digital image correlation. *Meas. Sci. Technol.*, 20: 062001, 2009.

[88] Arman Pazouki, Michał Kwarta, Kyle Williams, William Likos, Radu Serban, Paramsothy Jayakumar, and Dan Negrut. Compliant contact versus rigid contact: A comparison in the context of granular dynamics. *Physical Review E*, 96(4):042905, 2017.

[89] Andrew Phillip Grima and Peter Wilhelm Wypych. Discrete element simulations of granular pile formation: Method for calibrating discrete element models. *Engineering Computations*, 28(3):314–339, 2011.

[90] Nicholas A Pohlman, Julio M Ottino, and Richard M Lueptow. End-wall effects in granular tumblers: From quasi-two-dimensional flow to three-dimensional flow. *Physical review E*, 74(3):031305, 2006.

[91] Valentin L Popov. *Contact mechanics and friction*. Springer, 2010.

[92] Olivier Pouliquen. Scaling laws in granular flows down rough inclined planes. *Physics of fluids*, 11(3):542–548, 1999.

[93] Olivier Pouliquen. Velocity correlations in dense granular flows. *Physical review letters*, 93(24):248001, 2004.

[94] Olivier Pouliquen and Yoel Forterre. A non-local rheology for dense granular flows. *Philosophical Transactions of the Royal Society of London A: Mathematical, Physical and Engineering Sciences*, 367(1909):5091–5107, 2009.

[95] Farhang Radjai and Stéphane Roux. Turbulentlike fluctuations in quasistatic flow of granular media. *Physical Review Letters*, 89(6):064302, 2002.

[96] Farhang Radjai, Michel Jean, Jean-Jacques Moreau, and Stéphane Roux. Force distributions in dense two-dimensional granular systems. *Physical review letters*, 77(2):274, 1996.

[97] Farhang Radjai, Dietrich E Wolf, Michel Jean, and Jean-Jacques Moreau. Bimodal character of stress transmission in granular packings. *Physical review letters*, 80(1):61, 1998.

[98] CJ Reagle, JM Delimont, WF Ng, SV Ekkad, and VP Rajendran. Measuring the coefficient of restitution of high speed microparticle impacts using a ptv and cfd hybrid technique. *Measurement science and technology*, 24(10):105303, 2013.

[99] KA Reddy, Y Forterre, and O Pouliquen. Evidence of mechanically activated processes in slow granular flows. *Physical Review Letters*, 106(10):108301, 2011.

[100] Mathieu Renouf, Daniel Bonamy, Frederic Dubois, and Pierre Alart. Numerical simulation of two-dimensional steady granular flows in rotating drum: On surface flow rheology. *Physics of fluids*, 17(10):103303, 2005.

[101] Patrick Richard, Mario Nicodemi, Renaud Delannay, Philippe Ribiere, and Daniel Bideau. Slow relaxation and compaction of granular systems. *Nature materials*, 4(2):121, 2005.

[102] Patrick Richard, Alexandre Valance, J-F Métayer, Paola Sanchez, Jérôme Crassous, M Louge, and Renaud Delannay. Rheology of confined granular flows: Scale invariance, glass transition, and friction weakening. *Physical review letters*, 101(24):248002, 2008.

[103] Leo Rothenburg and RJ Bathurst. Analytical study of induced anisotropy in idealized granular materials. *Geotechnique*, 39(4):601–614, 1989.

[104] J.C. Russ. *The Image Processing Handbook, 5th edition*. CRC Press, 2007.

[105] Chris H Rycroft, Gary S Grest, James W Landry, and Martin Z Bazant. Analysis of granular flow in a pebble-bed nuclear reactor. *Physical review E*, 74(2):021306, 2006.

[106] Kuniyasu Saitoh and Brian P Tighe. Nonlocal effects in inhomogeneous flows of soft athermal disks. *Physical review letters*, 122(18):188001, 2019.

[107] SB Savage. Analyses of slow high-concentration flows of granular materials. *Journal of Fluid Mechanics*, 377:1–26, 1998.

[108] Leonardo E Silbert, Deniz Ertaş, Gary S Grest, Thomas C Halsey, Dov Levine, and Steven J Plimpton. Granular flow down an inclined plane: Bagnold scaling and rheology. *Physical Review E*, 64(5):051302, 2001.

[109] P. Soille. *Morphological Image Analysis - Principles and Applications, 2nd edition*. Springer-Verlag, New York, 2003.

[110] Lydie Staron. Correlated motion in the bulk of dense granular flows. *Physical Review E*, 77(5):051304, 2008.

[111] Lydie Staron and Farhang Radjai. Friction versus texture at the approach of a granular avalanche. *Physical Review E*, 72(4):041308, 2005.

[112] Lydie Staron, Jean-Pierre Vilotte, and Farhang Radjai. Preavalanche instabilities in a granular pile. *Physical Review Letters*, 89(20):204302, 2002.

[113] M.A. Sutton, J.J. Orteu, and H. Schreier. *Image Correlation for Shape, Motion and Deformation Measurements: Basic Concepts,Theory and Applications*. Springer US, 2009.

[114] Nicolas Taberlet, Patrick Richard, Alexandre Valance, Wolfgang Losert, José Miguel Pasini, James T Jenkins, and Renaud Delannay. Superstable granular heap in a thin channel. *Physical review letters*, 91(26):264301, 2003.

[115] Nicolas Taberlet, Patrick Richard, and E John Hinch. S shape of a granular pile in a rotating drum. *Physical Review E*, 73(5):050301(R), 2006.

[116] William Thielicke and Eize Stamhuis. Pivlab–towards user-friendly, affordable and accurate digital particle image velocimetry in matlab. *Journal of Open Research Software*, 2(1), 2014.

[117] Kyle VanderWerf, Weiwei Jin, Mark D Shattuck, and Corey S O'Hern. Hypostatic jammed packings of frictionless nonspherical particles. *Physical Review E*, 97(1):012909, 2018.

[118] Ivan Vlahinić, Edward Andò, Gioacchino Viggiani, and José E Andrade. Towards a more accurate characterization of granular media: extracting quantitative descriptors from tomographic images. *Granular Matter*, 16(1):9–21, 2014.

[119] Charles Voivret, Farhang Radjai, J-Y Delenne, and Moulay Saïd El Youssoufi. Multiscale force networks in highly polydisperse granular media. *Physical review letters*, 102(17):178001, 2009.

[120] Z Zeravcic, N Xu, AJ Liu, SR Nagel, and Wim van Saarloos. Excitations of ellipsoid packings near jamming. *EPL (Europhysics Letters)*, 87(2):26001, 2009.

[121] Qiong Zhang and Ken Kamrin. Microscopic description of the granular fluidity field in nonlocal flow modeling. *Physical Review Letters*, 118(5): 058001, 2017.

[122] YC Zhou, BD Wright, RY Yang, Bao Hua Xu, and Ai-Bing Yu. Rolling friction in the dynamic simulation of sandpile formation. *Physica A: Statistical Mechanics and its Applications*, 269(2-4):536–553, 1999.

[123] Ling-Nan Zou, Xiang Cheng, Mark L Rivers, Heinrich M Jaeger, and Sidney R Nagel. The packing of granular polymer chains. *Science*, 326(5951): 408–410, 2009.

Appendix A

RESOLVE THE MESH-DEPENDENCY OF CURRENT LS-DEM IMPLEMENTATION

As mentioned in section two, in LS-DEM currently force and moment contributions from all penetrating nodes are considered, which in fact will cause LS-DEM to be mesh-dependent in displacement controlled loading condition - the mechanical response of a particle system will depend sensitively on the discretized fineness of each particle's surface, i.e. how many nodes each particle has. However, such mesh-dependent behavior vanishes for force controlled loading condition. To see this, using both LS-DEM and DEM with exactly the same model parameters we present several numerical tests of two identical frictional disk with radius $R = 15$ mm vertically stacked between two rigid walls with the top wall being moved downward via either displacement controlled (Δ) or force controlled condition (f), as shown in Figure A.1. In either case we output two quantities: the contact force magnitude $|F|$, and the inter-particle penetration d. For DEM $d = 2R - |\boldsymbol{r}_1 - \boldsymbol{r}_2|$ where $\boldsymbol{r}_1, \boldsymbol{r}_2$ are the centroid position of the two particle respectively; for LS-DEM $d = \sum_z d_z$ where we sum over the penetration d_z of all penetrating nodes. For LS-DEM simulation each disk surface is randomly spatially discretized with either 30, 50 or 70 nodes. As shown in Figure A.2, the mesh-dependence problem appears for displacement controlled loading condition while vanishes for force controlled case. This can be explained by the following: in displacement controlled case the top wall is displaced downward for a certain amount that will lead to larger contact force with denser disk surface discretization, which subsequently leads to increasing $|F|$ and d; while for the force controlled case, external force is already known and is used to compute displacement by enforcing equilibrium − no matter how dense the surface discretization is the total force from all penetrating nodes should always equilibrate the externally prescribed one. Therefore the results for $|F|$ and d all collapse onto those computed from DEM.

In order to solve this mesh-dependency problem and further show that LS-DEM converges to DEM with proper modification, two simple approaches are tested: regarding the contributions from all penetrating nodes, we either take average or

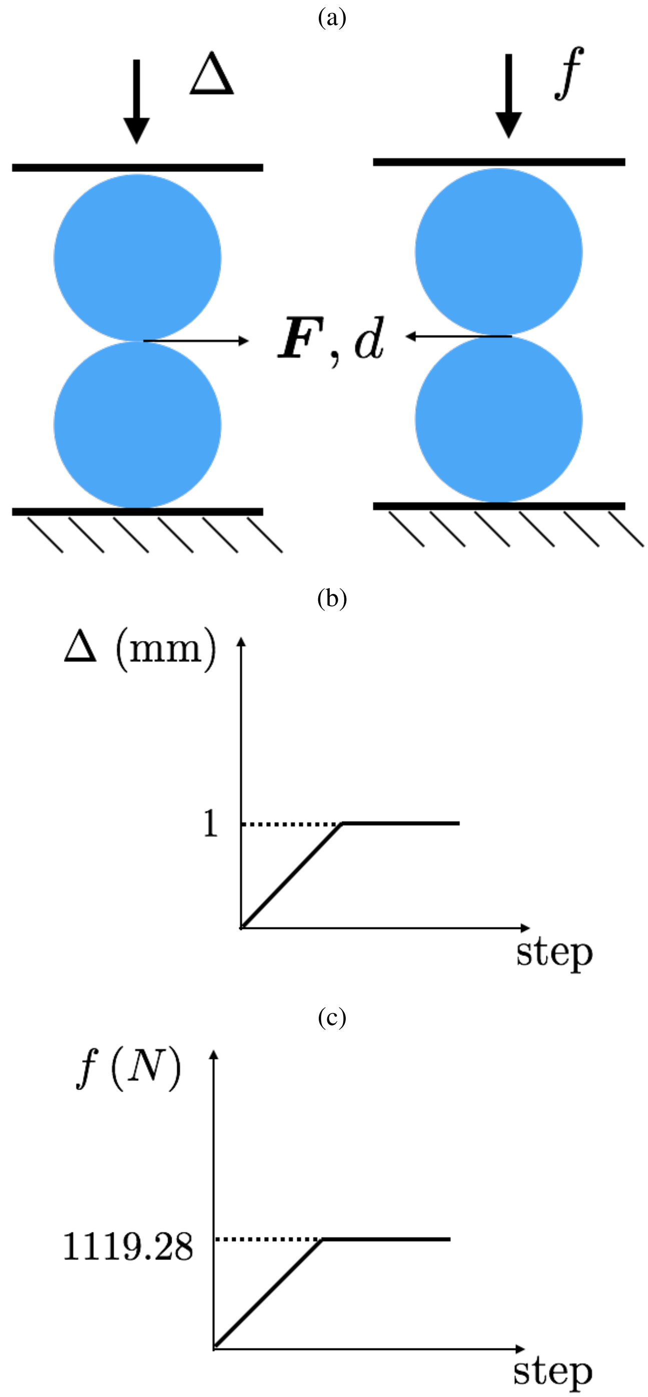

Figure A.1: Two spheres being stacked and then loaded vertically. (a) Displacement controlled and force controlled loading condition with prescribed Δ and f, respectively, and both with the output in terms of inter-particle force F and penetration d; (b)(c) Loading curve of input Δ and f.

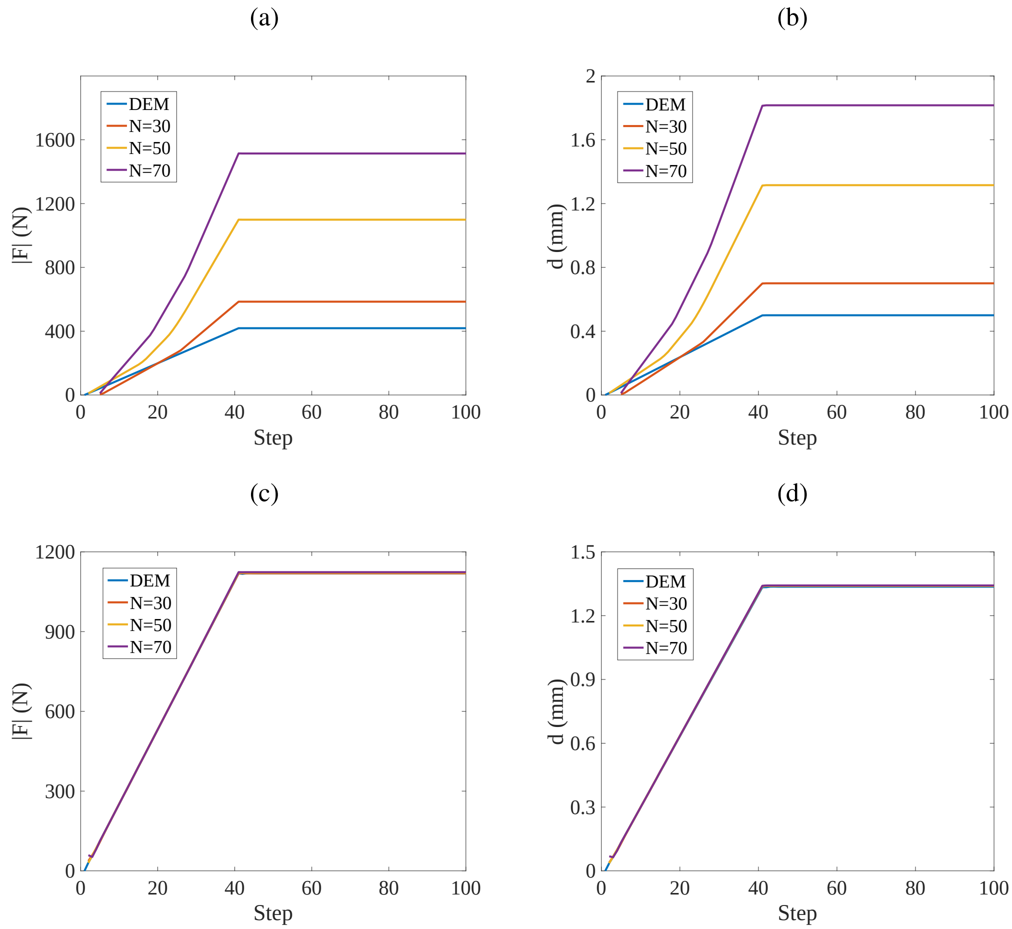

Figure A.2: Inter-particle force magnitude $|F|$ and penetration d response for displacement controlled case (a),(b), and for force controlled case (c),(d) from DEM simulation and LS-DEM simulations with 30, 50, or 70 nodes.

only consider the one with maximum penetration:

$$\boldsymbol{f}_n = \frac{1}{P}\sum_{z=1}^{P} \boldsymbol{f}_{n,z}, \quad \boldsymbol{f}_t = \frac{1}{P}\sum_{z=1}^{P} \boldsymbol{f}_{t,z} \tag{A.1}$$

or

$$\boldsymbol{f}_n = \boldsymbol{f}_{n,z_m} | d_{z_m} = \max_{1\le z\le P}\{d_z\}, \quad \boldsymbol{f}_t = \boldsymbol{f}_{t,z_m}^{j,i} | d_{z_m} = \max_{1\le z\le P}\{d_z\} \tag{A.2}$$

As shown in Figure A.3, for displacement controlled loading condition, both approaches resolve the mesh-dependency problem but only the modification of considering maximum penetration can further make LS-DEM converge to DEM: the computed $|F|$ and d from LS-DEM converge to those computed from DEM as the node number N discretizing a grain surface is increased from 30 to 70. We can

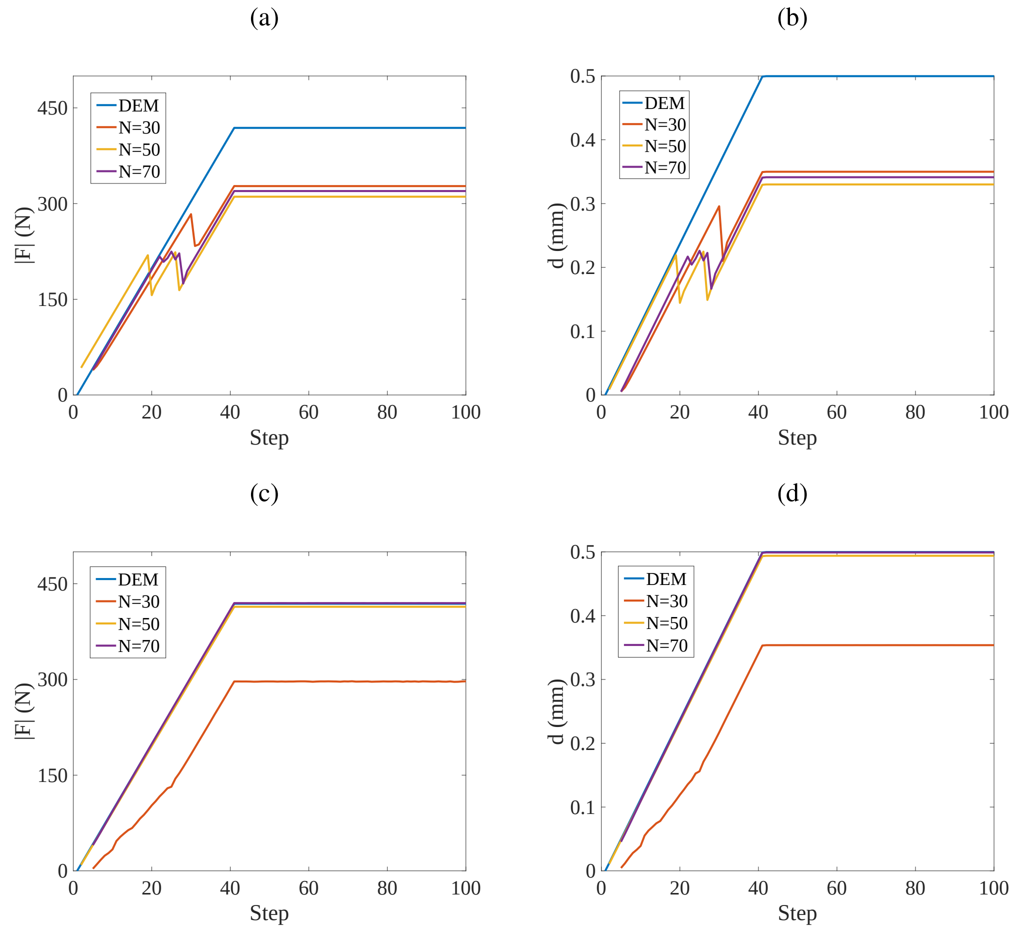

Figure A.3: Inter-particle force magnitude $|F|$ and penetration d response for the same displacement controlled case from DEM simulation and LS-DEM simulations with 30, 50 or 70 nodes; (a),(b): taking average for all penetrating nodes and (c),(d): considering only the node with maximum penetration.

expect that as the value of N goes larger and larger, LS-DEM will converge to DEM for simulating circular particles with exactly the same model parameters.

Appendix B

BOUNDARY CONDITION IMPLEMENTATION

Here we discuss our methodology in estimating the variation of $|\boldsymbol{F}_A|$ and $|\boldsymbol{F}_B|$ as θ increases. We note first that all quantities mentioned here are experimentally measured. Following the discussion in section three (Figure. 2.6), we assume the forces exerted by the particles and from F_N to the boundary "AD-DC-BC" all act at the center of each bar and the former can be estimated based on the stress state of the granular assembly $\boldsymbol{\sigma}_\theta$. In each configuration with a certain θ value, we have the following unknown vectors: $\boldsymbol{F}_A$, $\boldsymbol{F}_B$ and $\boldsymbol{F}_h$, see Figure 2.6. However, we only end up having three instead of six unknowns due to our experiment setup: $\boldsymbol{F}_A$ and $\boldsymbol{F}_B$ should always be perpendicular to AD and BC, and $\boldsymbol{F}_h$ should always be horizontal. We herein denote them as F_A, F_B and F_h as the corresponding signed magnitude: if positive the force is along the assumed direction, otherwise opposite. With force and torque equilibrium we have three equations and can therefore solve for F_A, F_B and F_h. At a certain configuration with a given θ, we assume that:

$$\boldsymbol{F}_A = F_A \begin{bmatrix} \cos\theta & \sin\theta \end{bmatrix}, \tag{B.1}$$

$$\boldsymbol{F}_B = F_B \begin{bmatrix} \cos\theta & \sin\theta \end{bmatrix}, \tag{B.2}$$

$$\boldsymbol{F}_h = F_h \begin{bmatrix} 1 & 0 \end{bmatrix}. \tag{B.3}$$

Forces exerted by the particles can be estimated by:

$$\boldsymbol{F}_{pq} = -\left(\boldsymbol{\sigma}_\theta \cdot \boldsymbol{n}_{pq}\right) S_{pq}, \tag{B.4}$$

where "pq" is one of " AD", "DC" and "BC" and S_{pq} is the corresponding arm area. By force and torque equilibrium we must have:

$$\sum_l \boldsymbol{F}_l = \boldsymbol{0} \tag{B.5}$$

$$\sum_l \boldsymbol{r}_{lM} \times \boldsymbol{F}_l = \boldsymbol{0} \tag{B.6}$$

Where $\boldsymbol{F}_l$ stands for all external force exerted to "AD-DC-CB" with $\boldsymbol{r}_{lM}$ being the position vector point from point M (center of bar "DC") to the location of $\boldsymbol{F}_l$. Combining the above equations and after some algebra we arrive at the following linear system:

$$\boldsymbol{A}\boldsymbol{u} = \boldsymbol{b} \tag{B.7}$$

Where

$$\boldsymbol{A} = \begin{bmatrix} \cos\theta & \cos\theta & 1 \\ \sin\theta & \sin\theta & 0 \\ A_{31} & A_{32} & 0 \end{bmatrix}, \quad \boldsymbol{u} = \begin{bmatrix} F_A \\ F_B \\ F_h \end{bmatrix} \text{ and } \boldsymbol{b} = \begin{bmatrix} \tau_\theta S_{DC} \\ \sigma_{y,\theta} S_{DC} + F_N \\ b_3 \end{bmatrix}, \tag{B.8}$$

with

$$A_{31} = \frac{1}{2}\cos\theta\left(-2h_\theta \sec^2\theta - \boldsymbol{r}_{A2} + \boldsymbol{r}_{B2} + \tan\theta(\boldsymbol{r}_{A1} - \boldsymbol{r}_{B1})\right), \tag{B.9}$$

$$A_{32} = \frac{1}{2}\cos\theta\left(-2h_\theta \sec^2\theta + \boldsymbol{r}_{A2} - \boldsymbol{r}_{B2} + \tan\theta(\boldsymbol{r}_{B1} - \boldsymbol{r}_{A1})\right), \tag{B.10}$$

$$b_3 = S_{DC}\left[(\boldsymbol{r}_{A1} - \boldsymbol{r}_{B1})\sin\theta\sigma_{y,\theta} + \tau_\theta(\cos\theta + \sin\theta) - (\boldsymbol{r}_{A2} - \boldsymbol{r}_{B2})\cos\theta\sigma_{x,\theta}\right] \tag{B.11}$$

where $\boldsymbol{r}_A$ and $\boldsymbol{r}_B$ are locations of the slider A and B which both remain unchanged through the experiment with the subscripts "1" and "2" denoting the x and y component, respectively. Solving the above linear system can give us the estimation of F_A and F_B.

Appendix C

DISCRETE ELEMENT MODEL CALIBRATION AND VALIDATION

In this section we discuss how we determine the model parameters used in our simulations. In general, the interaction between rigid particles can be modeled by either solving a linear-complementarity problem (implicit dynamics, the NSCD) [58] or by penalizing the inter-particle penetration (explicit dynamics, the classical DEM). Despite the different underlying principle, they give consistent results within the scope of rigid particle dynamics [88]. For the classical DEM, there are various inter-particle contact laws with different level of sophistication. Following the discussion in [108], we choose the linear Hookean contact law and pick $k_{\mathrm{n}} = 2{\times}10^5\bar{m}g/\bar{d}$ (large enough to ensure rigid particle limit for the gravity-driven surface flows considered in our study) with $k_{\mathrm{t}} = 2/7k_{\mathrm{n}}$, $\gamma_{\mathrm{t}} = 0$, and $\gamma_{\mathrm{n}} = -2\ln e\sqrt{\bar{m}k_{\mathrm{n}}/(\pi^2 + \ln^2 e)}$. We are left to determine the coefficient of restitution e, the inter-particle friction μ_{p}, the particle-wall friction and possibly the addition of rolling friction μ_{r}.

C.1 First stage calibration via column collapse tests

We use the column collapse test to perform preliminary model calibration by measuring the angle of repose θ_r.We first glue glass beads to the center area of an aluminum sheet (300×300mm) and the inner surface of two identical iron angle bars with height 50mm, length 25mm and width 16 mm (Fig.C.1(a)). A typical column collapse test can be divided into three steps: (i) filling with glass beads the hollow rectangular tube formed by the two iron angle bars placed over the aluminum sheet center, (ii) rapidly removing the bars, and (iii) taking picture of the formed pile to measure θ_r. We repeat the procedure for 50 times and θ_r is measured to have a mean of 13.87° and a standard deviation of 0.576°.

Via DEM simulations, we then perform numerical column collapse tests with the same configuration as in the experiments. We carry out two sets of simulations: (1) fixing $\mu_{\mathrm{p}} = 0.4$ (a common choice for glass beads) and varying e from 0.1 to 0.82, and (2) fixing $e = 0.82$ [98] and varying μ_{p} from 0.1 to 0.8. From (1) we find that e has negligible effect on θ_{r} (Fig.C.1(c)), and from (2) that θ_{r} first increases but later saturates with the increase of μ_{p} (Fig.C.1(b)). In summary the above results suggest the necessity to incorporate rolling friction μ_{r}, a parameter that imposes

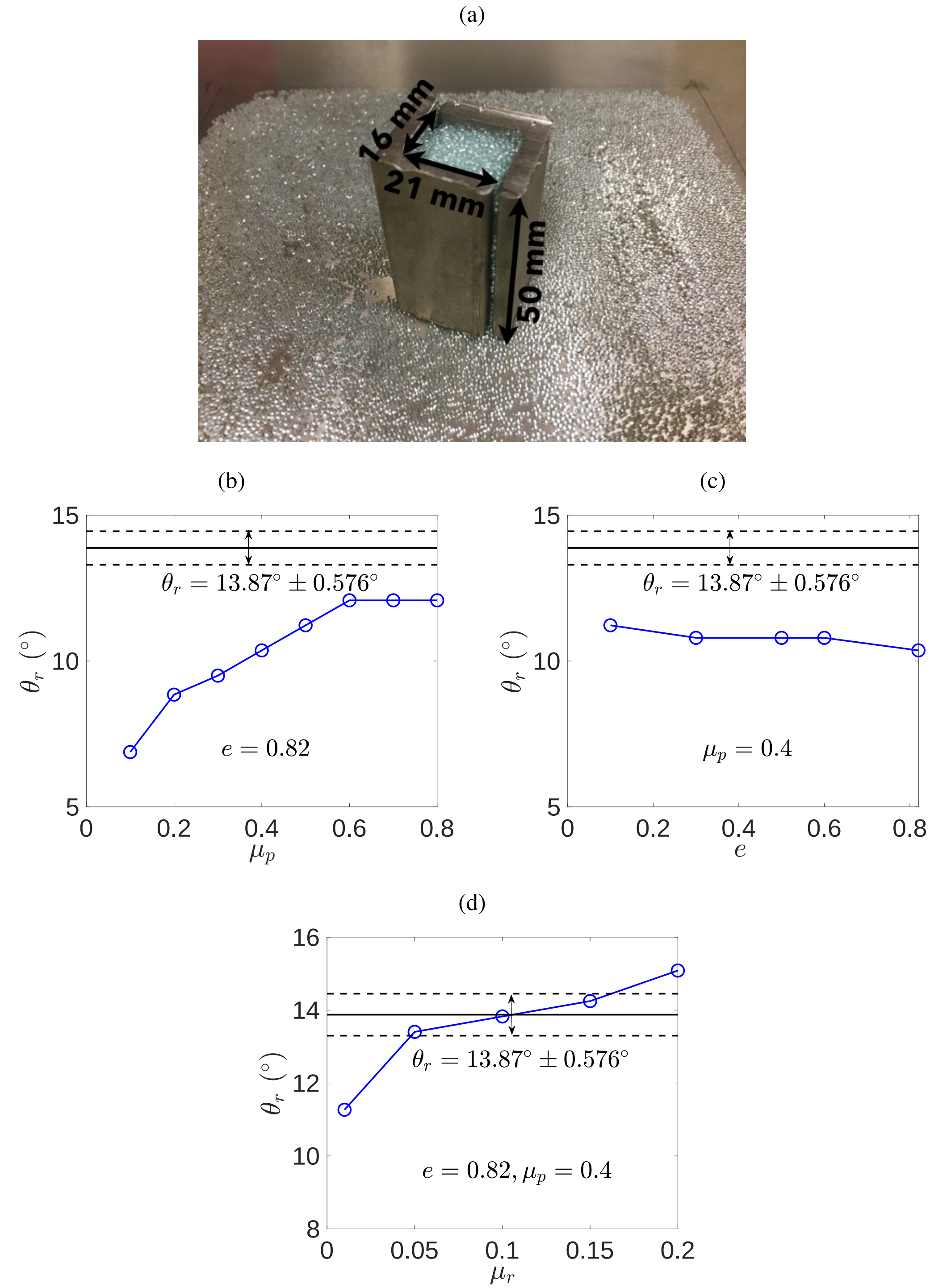

Figure C.1: The experimental setup of the column collapse test together with the simulation results. (a) Setup of the column collapse test, (b) variation of θ_r according to the change of μ_p with a fixed $e = 0.82$, (c) variation of θ_r according to the change of e with a fixed $\mu_p = 0.4$, and (d) variation of θ_r according to the change of μ_r with fixed $\mu_\mathrm{p} = 0.4$, $e = 0.82$.

rotation hinderance [122] to model the interaction between non-spherical particles. Accordingly, we fix $e = 0.82, \mu_{\mathrm{p}} = 0.4$ and vary μ_{r} from 0.01 to 0.2. Fig.C.1(d) shows the variation of θ_{r} against μ_{r}. The numerical results indicate μ_{r} to be around 0.07 which is slightly larger than 0.01 in [44] where smooth glass spheres were used and slightly smaller than 0.1 in [89] where plastic spheres were used.

C.2 Second stage calibration and validation via rotating drum experiments

In the rotating drum experiments (Fig.C.2(a)), after the surface flow becomes stationary under rotation speed $\omega = 2.59°/s, 5.73°/s$ and $11.23°/s$, we use a high speed camera positioned against the glass plate to take images (288 px × 288 px corresponding to a 0.1389 mm/px resolution) for a time period of 10 s with a frame rate of 1000 fps. Accordingly the images cover an area of about 4 cm ×4 cm at the drum center (Fig.C.2(b)). From the sequence of images, we measure the dynamical angle of repose θ_d and the down-stream velocity $v_{\mathrm{yw}}(z)$ near the glass plate. In terms of the former, we first binarize each image, then identify the pixels that represents the slope surface, and lastly use the identified pixels to perform a linear fit whose slope gives θ_{d} (Fig.C.2(d)); as to the latter, we first use the open-source Particle Image Velocimetry (PIV) code [116] to compute the 2D velocity field (v_1, v_2) by correlating boxes with dimension 8 px ×8 px (corresponding to roughly $\bar{d} \times \bar{d}$), we then compute the velocity field under the frame rotating with the drum located at the drum center to get $(v_{\mathrm{y}}, v_{\mathrm{z}})$, lastly we compute $v_{\mathrm{yw}}(z)$ by averaging v_{y} within bands $(L_{\mathrm{y}} = 20\bar{d}, L_{\mathrm{z}} = 2\bar{d})$ positioned in parallel to y (slope surface) over a set of points that are placed every $\bar{d}$ distance along z (perpendicular to the slope surface) with $y = 0$. Note that $|v_{\mathrm{z}}| \ll |v_{\mathrm{y}}|$ as the flow is nearly unidirectional. In the simulations, we generate images located at exactly the same location with exactly the same size (and resolution) as the ones taken from experiment (Fig.C.2(c)), from which we follow the same image analysis procedure to find θ_{d}. For v_{yw}, under the frame rotating with the drum at the drum center, we first pick particles located within $2\bar{d}$ away from the front-side flat wall, we then compute $v_{\mathrm{yw}}(z)$ by averaging the particle velocity following the same procedure used in the experiments. Note that the width $2\bar{d}$ is picked to best represent the glass beads that are captured by the high speed camera.

We use θ_d and $v_{yw}(z)$ measured with $\omega = 11.23°/s$ for model calibration and the rest two for model validation. Prior to calibration, according to the column collapse test results, we fix $\mu_{\mathrm{p}} = 0.4$, and $e = 0.82$ that best represents the property of glass beads, although the latter has negligible effect for simulating steady granular flow

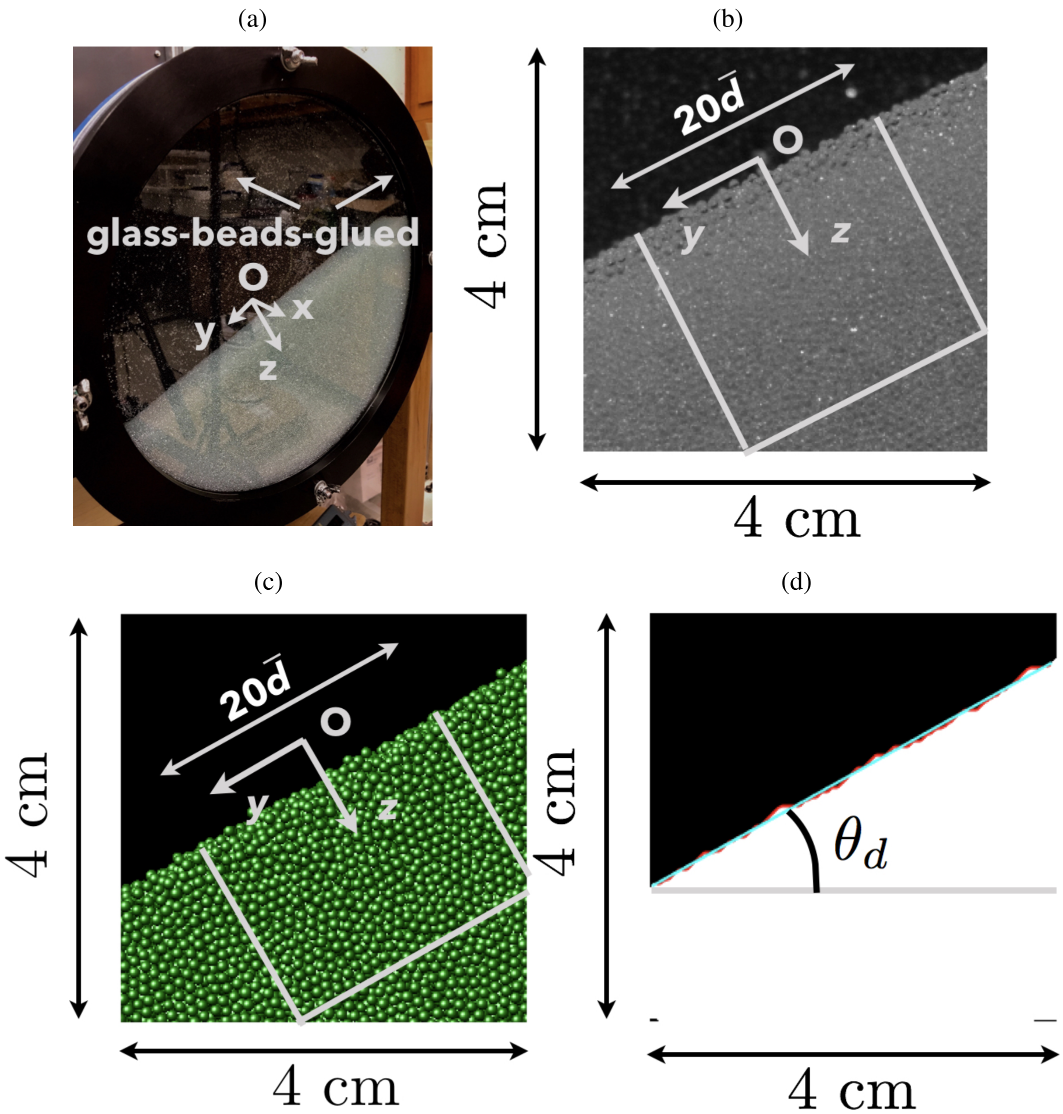

Figure C.2: The images taken from both experiments and simulations. (a) The half-filled rotating drum with rear-side wall and inner-cylinder wall being glued with glass beads, (b) an image taken by the high speed camera at the drum center, (c) an image generated by numerical simulation with exactly the same location and size (resolution) as (b), (d) the binarized image of (c) for θ_{d} estimation.

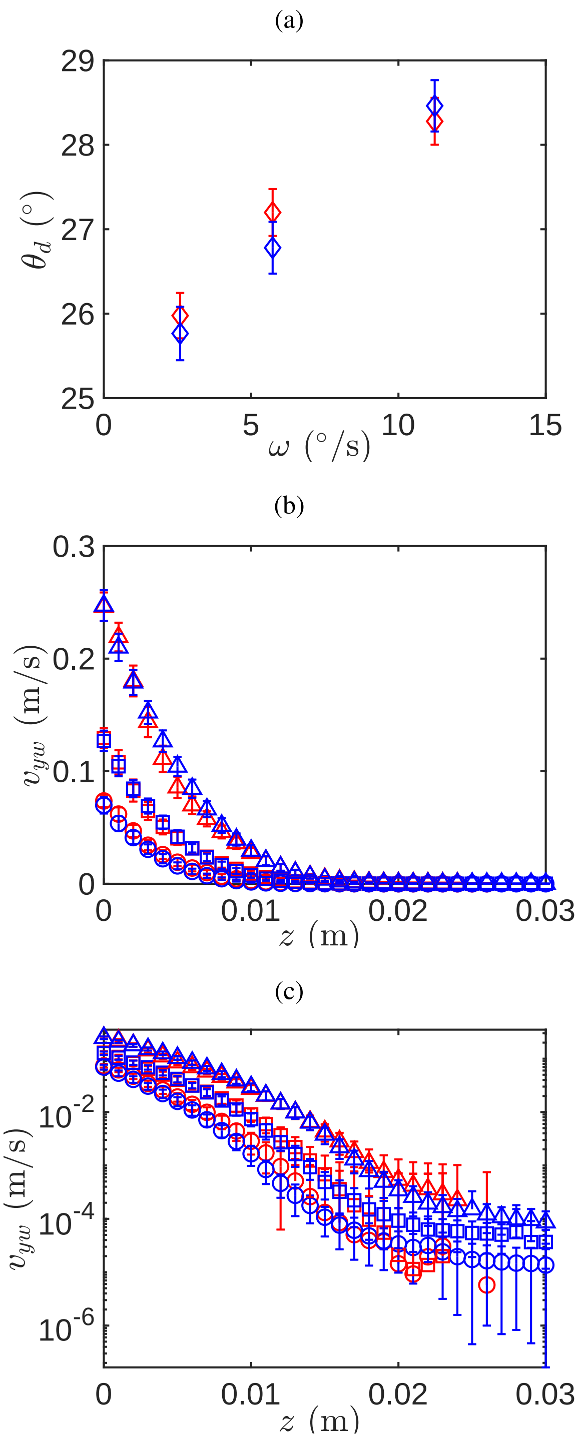

Figure C.3: Experimental and simulation results. (a) time-averaged θ_d data for three different rotating speed ω estimated from experiments (red) and simulations (blue), (b) the down-stream velocity profile $y_{\mathrm{yw}}(z)$ against the depth at the drum center calculated respectively for $\omega = 11.23°/s$ from experiment (red triangle) and simulation (blue triangle), for $\omega = 5.73°/s$ from experiment (red square) and simulation (blue square), and for $\omega = 2.59°/s$ from experiment (red circle) and simulation (blue circle), and (c) the corresponding semi-log plot of (b). The error bars represent the standard deviation associated with each time-averaged quantity.

[108]. Further, as the front-side plate is also made from glass, we fix the associated wall friction to be 0.4. The only left parameter to calibrate is the inter-particle rolling friction μ_r. Observing Fig.C.1(d), we vary μ_r to be $0, 0.03, 0.05$, and 0.07 and take the particle-wall rolling friction to be zero. As the front-side wall is flat, zero wall rolling friction is a reasonable choice. By solely using θ_d, we identify that $\mu_\mathrm{r} = 0.03$ gives the best estimation ($\mu_\mathrm{r} = 0$ underestimates θ_d while the other two lead to overestimation). What's more, when $\mu_\mathrm{r} = 0.03$, simulation and experiment show excellent agreement (Fig.C.3(a)) in terms of $v_\mathrm{yw}(z)$. The choice of $\mu_\mathrm{r} = 0.03$ is then validated (Figs.C.3(a), C.3(b) and C.3(c)) by comparing both θ_d and $v_\mathrm{yw}(z)$ obtained from simulations to those measured from experiments under $\omega = 2.59°/\mathrm{s}$ and $\omega = 5.73°/\mathrm{s}$.

C.3 Additional simulation results

"S-shape" surface profile

For a direct comparison, Fig.C.4 shows the surface shape profile for simulations performed under, respectively, periodic boundary condition, frictional side walls with $W/\bar{d} \simeq 21$ and wall friction 0.4, and that with $W/\bar{d} \simeq 10$ and wall friction 0.4. It can be observed that as the effective drum width is decreased from infinite (periodic boundaries) to $W/\bar{d} \simeq 21$ and to $W/\bar{d} \simeq 21$, the "S-shape" profile becomes more obvious under more significant side wall friction effects, especially when the rotation speed is large such as when $\omega = 67.38°/\mathrm{s}$ (Figs.C.4(j) and C.4(o)) in our case.

Effect of lateral boundary condition on the co-directionality between s and $\dot{\gamma}^d$

Fig.C.5 showcases the spatial variation of the misalignment angle α for all considered drum configurations under $\omega = 33.69°/\mathrm{s}$, where α is defined as the angle between the principle directions of s and those of $\dot{\gamma}^d$. It can be observed that the presence of frictional side wall has a great impact on the value of α, and the more frictional the side walls and the narrower the drum, the less co-directional are s and $\dot{\gamma}^d$. α is generally large (up to 60°) near the side walls (especially on the bumpy side), and beneath $z = z_\mathrm{th}$ in the creep flow region. The green solid line indicates locations with local deformation $|\dot{\gamma}^d|/2\Omega$ equalling one [32] where $\Omega = \omega/360°$; locations above this line have $|\dot{\gamma}^d|/2\Omega > 1$ while $|\dot{\gamma}^d|/2\Omega < 1$ for locations below this line. It thus may be understood that the large α in the creep flow region is due to the lack of shear. For locations above $z = z_\mathrm{th}$, shear deformation is sufficient, and the misalignment α can be attributed to side wall perturbation.

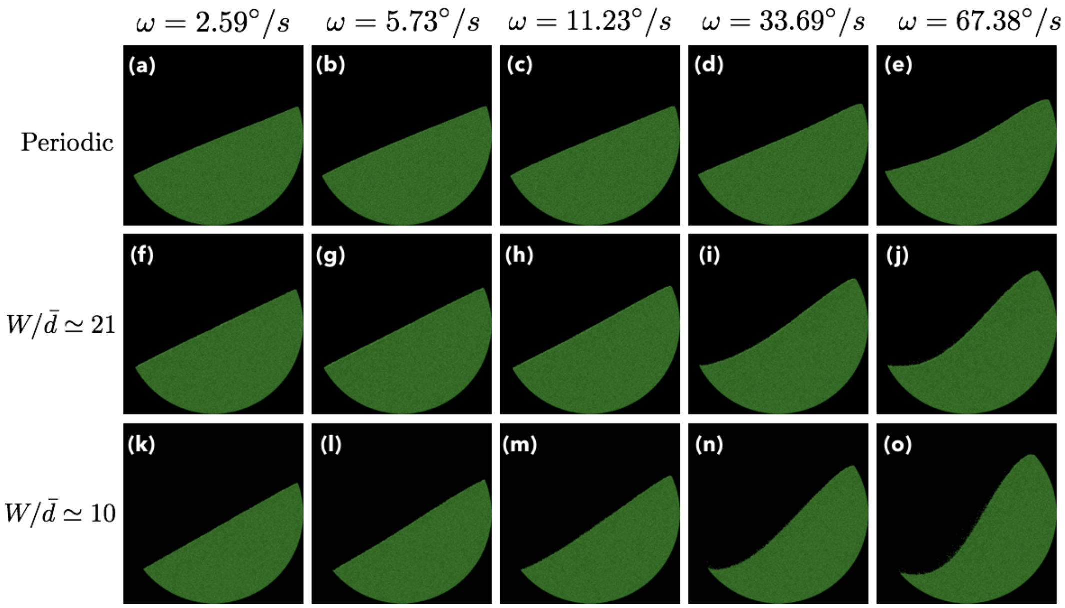

Figure C.4: Surface shape profiles. Images in first row from (a) to (e) are those under periodic lateral boundaries, in second row from (f) to (j) represents those under frictional side walls with $W/\bar{d} \simeq 21$, and in third row from (k) to (o) represents those under frictional side walls too but with $W/\bar{d} \simeq 10$. Wall friction is 0.4.

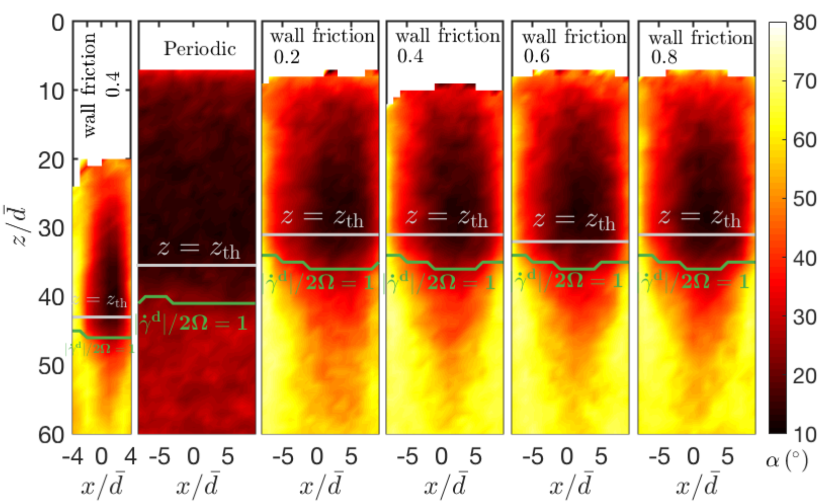

Figure C.5: Spatial variation of α under $\omega = 33.69°/\mathrm{s}$ for all drum configuration considered; from left to right: $W/\bar{d} \simeq 10$ with wall friction of 0.4, periodic boundary, $W/\bar{d} \simeq 21$ with wall friction of 0.2, 0.4, 0.6 and 0.8, respectively. The grey solid lines indicate $z = z_{\mathrm{th}}$ and the green ones represent locations with local deformation $|\dot{\gamma}^d|/2\Omega = 1$, where $\Omega = 360°/\omega$.

Tests of several non-local models

- **The velocity fluctuation model**. Based on 2D numerical simulation results on granular flow in annular shear cells, the model proposed in [45] shows that an improved relation between μ and I by adding the effect of velocity fluctuation is able to capture the failure of the one-to-one $\mu(I)$ relation in the creep flow region. The key prerequisite of this model is that the variation of $\mu - I$ and that of $\Delta - I$ are both not one-to-one and are mutually correlated, where $\Delta = |\delta v|\sqrt{\rho_s/P}$ is called the fluctuation number. However, Fig.C.6(a) shows that for all flows considered, there is a global collapse between Δ and I. It appears that this model does not apply to the 3D flows considered in our study.

- **The gradient expansion model**. In the gradient expansion model [20], the value of μ in the $\mu - I$ relation is modified by considering an additional contribution $\bar{d}^2\nabla^2 I/I$which is scaled by a phenomenological constant $\nu > 0$, assuming short range correlation between particle motions in different locations. Physically, the Laplacian term captures on average, how does the I value at a certain point compares to its surrounding area. For instance, if a point is surrounded by a more fluid-like area (higher I), the laplacian term is positive and leads to the decrease of μ at that point. Since $\nu > 0$, essentially as long as $\nabla^2 I \neq 0$, the model will report a modification on μ. Fig.C.6(c) shows the typical drum-width-averaged I and $|v|/\sqrt{g\bar{d}}$ against z with the case under $\omega = 33.69°/s, W/d \simeq 21$ and wall friction of 0.4. The variation of I against z roughly follows the same trend as that of $|v|/\sqrt{g\bar{d}}$: it linearly decays in the collisional region and exponentially decays in the dense region. Thus in the collisional region, $\nabla^2 I = 0$ and the model reports no modification on μ, which is consistent with our observation. However, in the dense region, μ will be modified according to the model since $\nabla^2 I \neq 0$ – this contradicts our computations that confirm the applicability of the $\mu - I$ relation in the dense region. Again, it appears that this model does not apply to the 3D surface flows considered in our study.

- **The fluidity model**. The fluidity model [61] implicitly modifies the value of μ in the $\mu - I$ relation by considering the nearby region contribution through the Laplacian of the fluidity parameter $g = \dot{\gamma}/\mu$ expressed as $\xi^2\nabla^2 g$, where ξ is defined as the cooperative length that diverges while approaching the jamming transition. Although the mathematical expression looks similar to that of the gradient expansion model, the assumed underlying physical mechanism is different. g is found to obey the following microscopic relation [121]: $\dot{\gamma}^d \bar{d}/\mu = \delta v F(\phi)$. Fig.C.6(b) shows how the normalized fluidity $\dot{\gamma}^d \bar{d}/(\mu \delta v)$, varies with volume fraction ϕ. It can be observed for all data computed from $W/\bar{d} \simeq 21$ with varying side wall friction, they collapse well onto a single curve who shape resembles the one identified in [121]. However, this curve is clearly drum-width-dependent, as when the effective drum width is respectively infinite (periodic boundary, colored in blue) and $10\bar{d}$ (colored in yellow), no collapse can be observed, even in the dense and collisional region where the $\mu(I)$ rheology in its invariant form holds. Memory effect (insufficient shear) observed for $I < I_{\text{th}}$ (see Fig.C.5) may explain the failure of the model in the creep flow region; while its break down in the fast flow regime ($I > I_{\text{th}}$ with sufficient shear deformation) reveals the non-trivial effects of side wall friction that have not been considered in the granular fluidity model [121] - indeed, even though investigated in 3D configuration, the considered flow fields have shear only in z direction as boundaries along both x and y direction are treated as periodic.

Additional results from micro-scale analysis

The micro-structure can be investigated by three kinds of quantities that range from lower-order (L) to higher-order (H) within each kind: (i) geometry-associated ones range from volume fraction ϕ (L), coordination number Z (L) to the angular distribution of contact orientation (H) [13, 103]; (ii) inter-particle-force-associated ones range from normal (and tangential) force p.d.f. distribution (L) [13, 103] to their angular distributions (H) [13, 103]; and (iii) kinematics-associated ones where the lower order quantity can be the velocity fluctuation δv [45, 121]. Inspired by [95, 103], we may regard $a_\chi^v = (\lambda_3 - \lambda_1)/(\lambda_3 + \lambda_1)$ as the higher order quantity where $\lambda_3(\lambda_1)$ is the maximum (minimum) eigenvalue of the tensor $\chi = \langle |\delta v| n_i^v n_j^v \rangle / \langle |\delta v| \rangle$. Here "$\langle \cdot \rangle$" denotes the average over all particles and n^v is the direction of velocity fluctuation associated with each particle. Accordingly a_χ^v has range from 0 to 1 and reflects how "cooperative" the particle motions are: a value close to 1 in the quasi-static flow region implies the formation of "granular eddy" [64, 79].

In principle, we are trying to find certain micro-structural quantities whose variations against I, (R1) exhibit a clear transition as passing through $z = z_{\text{th}}$, and more importantly, (R2) show consistence with that of μ against I for rheological considerations: when $I > z_{\text{th}}$ they are free of drum configuration effect and rotation

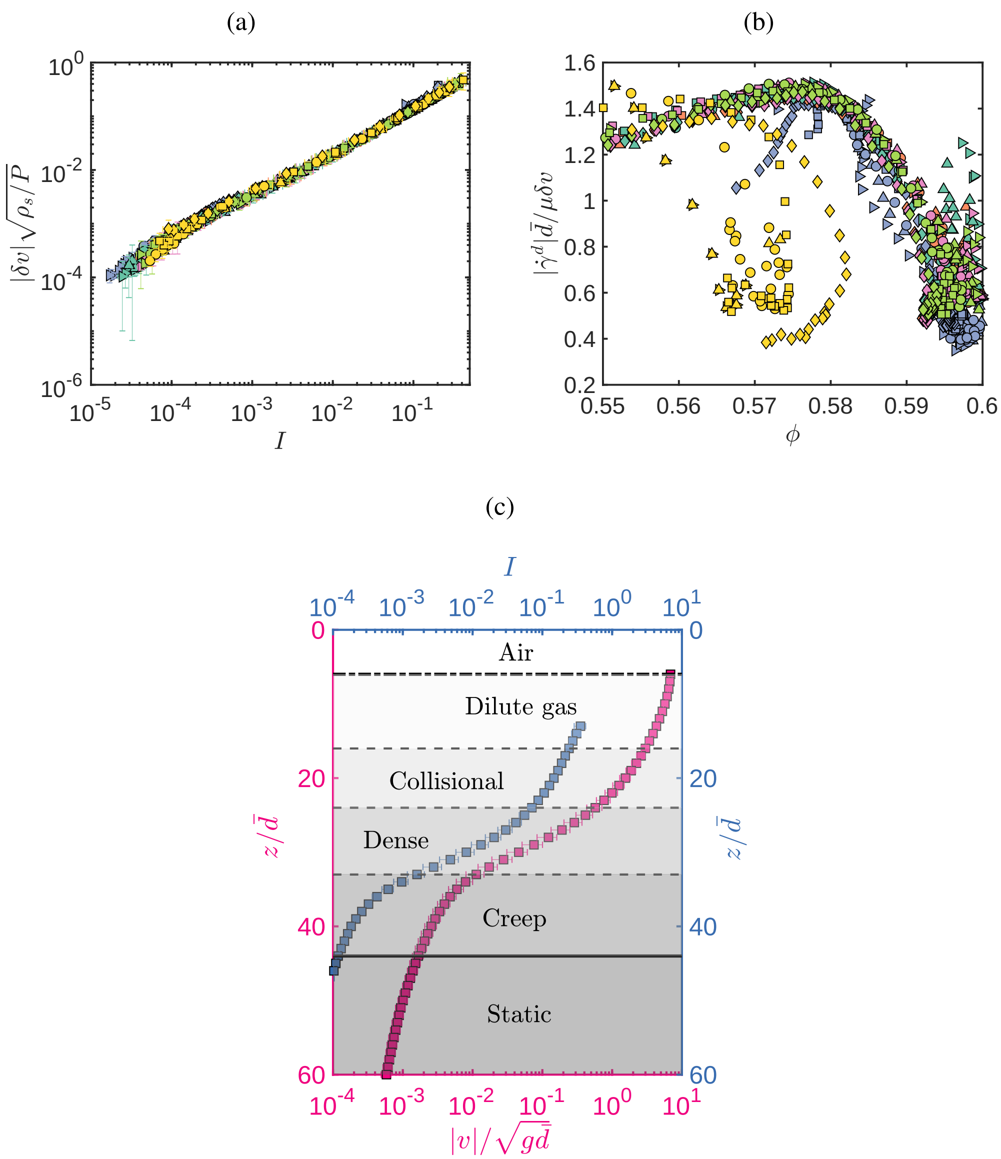

Figure C.6: Computed results for the three tested non-local models. (a) $\Delta - I$ data for all cases considered collapse onto a single master curve. Data are shown as the drum-with-average values with error bars representing the associated variation. (b) Relation between the normalized fluidity $|\dot{\gamma}^d|\bar{d}/\mu\delta v$ and volume fraction ϕ. (c) Variation of drum-width-averaged $|v|/\sqrt{g\bar{d}}$ and I against z with the case under $\omega = 33.69°/s, W/d \simeq 21$ and wall friction of 0.4. Data are shown as the drum-with-average values for clarity.

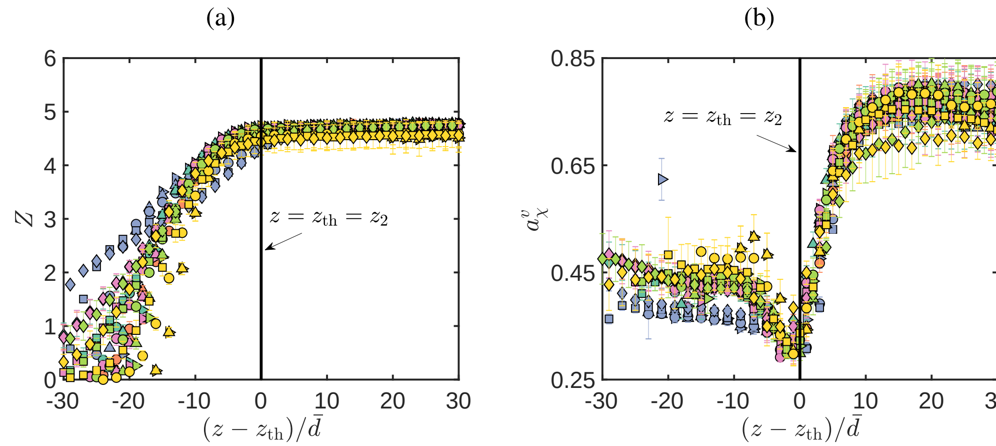

Figure C.7: Spatial variation of the coordination number Z and a^v_χ against the depth z. The symbol shape represents different rotation speed, while the symbol color represents different drum configurations in terms of drum width W and side wall friction. Error bars represent the variation of each shown quantity across the drum width.

speed effect while they become lateral boundary dependent and rotation speed dependent as soon as $I \le I_{\mathrm{th}}$. Many of the aforementioned quantities, as we discover, only satisfy R1, such as Z and a^v_χ. Fig.C.7(a) shows the variation of Z against the depth z. Z varies case by cases when $z \le z_{\mathrm{th}}$ and remains almost constant when $z > z_0$. However, on the contrary, the stress ratio μ shows a global collapse when $z \le z_{\mathrm{th}}$ but varies case by case when $z > z_{\mathrm{th}}$. a^v_χ shows a slightly different spatial variation (Fig.C.7(b)): it remains constant when $z \le z_{\mathrm{th}}$ in a similar way to that of $\delta\theta$. However, a^v_χ seems to be boundary condition dependent instead. When $z > z_{\mathrm{th}}$, it rapidly increases independently with respect to the boundary condition and rotation speed, which is inconsistent with the variation of μ either. Following the momentum transferring argument, we have also investigated the portion of formed granular clusters based on either the velocity fluctuation following [17, 64] or the local volume fraction fluctuation (achievable via the computed Voronoi diagram) following [17, 80]. The variation of such portion along the depth show similar trend as that of a^v_χ that does not satisfy (R2).

Determination of z_{th} based on the drum-width-averaged velocity profile

Fig.C.8 shows the velocity magnitude profile against depth at the drum center $|v|(z)$ and its variation across the drum width, for the same set of simulations considered here. When the lateral boundaries are periodic, $|v|(z)$ shows negligible differences

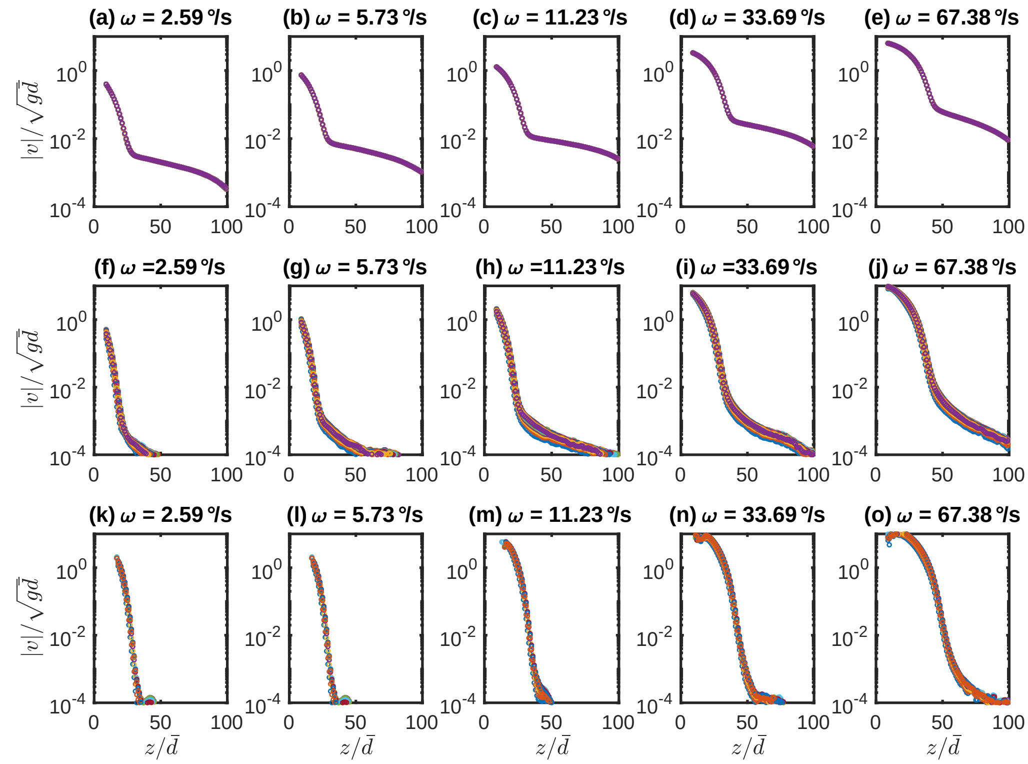

Figure C.8: $|v|(z)$ profile variation across the drum width for different rotation speeds with each color representing a certain location x between $-8\bar{d}$ and $9\bar{d}$ ($W/\bar{d} \simeq 21$) and between $-3\bar{d}$ and $4\bar{d}$ ($W/\bar{d} \simeq 10$). First row from (a) to (e): data extracted from simulations with periodic lateral boundaries; second row from (f) to (j): data extracted from simulations with frictional side walls ($W/\bar{d} \simeq 21$); third row from (k) to (o): data extracted from simulations with frictional side walls ($W/\bar{d} \simeq 10$); wall friction is 0.4.

across the drum width. For the cases with frictional side walls ($W/\bar{d} \simeq 21$ and 10), $|v|(z)$ varies majorly as vertical translation without shape alteration. Therefore, without sacrificing much the accuracy, we determine z_{th} based on the drum-width-averaged $|v|(z)$ profile.